UNIVERSITY OF COPENHAGEN
FACULTY OF SCIENCE

Master's thesis

Structural properties of kagome-layered crystals

Phenomenological and first-principles study

Luca Buiarelli

Advisors: Morten Holm Christensen and Brian Møller Andersen

Submitted: May 22, 2023

This thesis has been submitted to The Faculty of Science, University of Copenhagen

Abstract

This thesis investigates the structural properties of materials with kagome-layered crystal structure, focusing on the new kagome metals AV_3Sb_5 and the shandites $M_3A_2Ch_2$. The former have only recently been synthesized and found to have a charge ordering phase that doubles its unit cell, called a charge density wave (CDW). The latter have been known for a long time and have also recently resurfaced because of some interesting transport properties, possibly connected to topological effects, but none of them is known to have a similar CDW phase. The thesis begins by providing an overview of the materials and their crystal structures, highlighting the unique electronic features of the kagome lattice. It then extends the existing phenomenological Landau theory for CDW-like structural transitions in AV_3Sb_5 to the shandite crystal structure, revealing that the symmetries of $M_3A_2Ch_2$ could potentially allow for a CDW phase. Density Functional Theory (DFT) is then introduced as a computational tool to study the materials of interest. The simulations on CsV_3Sb_5 confirm the presence of an unstable phonon mode, signifying a structural instability, but are not able to identify electronic instabilities. Regarding the shandites, we focus on $Pd_3Sn_2Se_2$, where we examine its similarities and differences compared to the kagome metals. Through simulations, we demonstrate that there are no indications of any structural or electronic instability in $Pd_3Sn_2Se_2$ and other shandite compounds. Throughout the study, further investigations are proposed, such as studying the role of apical ions, exploring different shandite compounds, searching for shandites exhibiting CDW phases, and delving deeper into the interplay between phonons and electronic effects in the CDW formation. In summary, this thesis contributes to our understanding of the structural properties of kagome-layered compounds and their interplay with the electronic properties, laying the groundwork for future research and applications in the shandite materials.

Acknowledgements

First and foremost, I want to thank my supervisors, Morten Holm Christensen and Brian Møller Andersen, for the consistent support they offered me over the last year. Their willingness to address my doubts and questions provided me with invaluable guidance during (many) moments of uncertainty. I'm really grateful for how they impacted me and I will bring the lessons they thought me in all of my future research endeavors. I also want to thank Turan Birol from University of Minnesota, who helped me navigate through the topic of DFT, for his kindness and guidance.

Second, not in importance, I would like to express my heartfelt gratitude to my wonderful office-mates, Eva Lopez Rojo and Sofie Castro Holbæk, for all the discussion that we had and the time spent together. They made me feel so welcome and appreciated that the idea of going to our office every day to work was everything but a boring one. I am thankful for their friendship and the positive impact they had on my journey.

More broadly, I would like to thank everybody in the CMT group for providing such a nice and friendly environment. I want to thank especially Mercè Roig I Server, Andreas Kreisel, Henrik Schou Røising and Clara Neerup Breiø for the fruitful discussions that I had with them.

Lastly, I extend my deep appreciation to my family, Paolo, Bianca, and Giulia, for their unwavering support both financially and emotionally throughout this journey. Their love and encouragement have been instrumental in my success. I also am thankful to all my friends in Italy, including Alessandro, Mirco, Riccardo, Lucrezia, Luigi and Tommaso for constantly reaching out over the phone during these two years in Copenhagen. Additionally, my stay in Copenhagen and this last year of thesis, would have not been sustainable without all of the people that I met and became friend with here in Copenhagen: Qiyu, Christine, Luka, Jorge, Filippo and many others. Thank you guys for bringing joy and laughter to my days off, I will carry the lessons, memories, and connections forever.

Contents

Chapter 1

Introduction

The kagome lattice (Figure 2.8) is a triangular Bravais lattice with three atoms per unit cell. In their crystal structure, some materials - both found in nature and artificially synthesized - contain sheets of atoms arranged in a kagome lattice. The name was first used in 1951 by physicist Itiro Syôzi [1], who was referencing a pattern used in Japanese basket-weaving, and has stuck since then. Syôzi was studying the Ising model on the kagome lattice, and in the following decades most of the interest around kagome was related to geometrically frustrated magnetism and the quest to find quantum spin liquids [2], magnetic systems with large ground state degeneracy that fail to order even at $T = 0$ K due to quantum oscillations. The Hubbard model on the kagome lattice has been studied extensively, with numerical analyses finding unconventional superconductivity, charge and spin orders as possible ground states [3–5]. In recent years, interest in kagome materials has been revamped because of some newly found materials with peculiar electronic properties, such as pressure-tunable superconductivity [6], giant anomalous Hall effect (AHE) [7] and the speculated presence of topological effects [8] and local loop currents [9].

The kagome metals AV_3Sb_5 (where A = K, Rb, Cs) have been the subject of extensive research as they were the first kagome crystals discovered to exhibit superconductivity at low temperatures. Despite the absence of magnetic ordering, these materials exhibit a very large AHE. In a manner reminiscent of Cuprates and Iron-based superconductors, the superconductivity in AV_3Sb_5 emerges from and competes with another electronically ordered phase known as a Charge Density Wave (CDW) [6]. While the theory of a CDW in one dimension is well established in terms of a purely electronic Peierls instability [10] stemming from the nesting of the Fermi surface, the microscopic mechanism in two dimensional layered compounds is still highly debated [11]. In a heuristic sense, the CDW is a phenomenon in which an electronic order and a periodic lattice modulation help stabilize each other through the electron-phonon coupling. Numerous theoretical models have been proposed to explain the microscopic electronic nature of the CDW in AV_3Sb_5, often involving charge-bond orders and loop currents, referred to as real and imaginary CDWs. At the moment, first-principles calculations have been able to predict the lattice instability in AV_3Sb_5, but it has not been easy to predict the electronic instability.

Recently, there has also been much interest about the ferromagnetic $Co_3Sn_2S_2$ [8], with Shandite structure and kagome layers of cobalt. Like the kagome metals, this material has been found to have a large AHE [12], which is speculated to stem from its Weyl semimetal nature. The shandites family $M_3A_2Ch_2$ includes many other possible materials with kagome layers, sometimes also referred to as half antiperovskite [13], but around them there is not as much literature as $Co_3Sn_2S_2$ [14, 15]. To the extent of our knowledge, none of these materials have been found to undergo a CDW-like structural transition analogous to AV_3Sb_5.

In this work, we embark on a comprehensive exploration of the kagome lattice and the intriguing possibility of interplay between structural properties and electronic degrees of

(a)

(b)

Figure 1.1: How times have changed: (a) kagome basket weaver in Japan, 1915. Credit: Wikimedia Commons; (b) screenshot taken from the 2D Semiconductors website, displaying a sample of the kagome ferromagnet $Co_3Sn_2S_2$ for sale.

freedom. In Chapter 2 we present the materials and their structure more in detail and we give some arguments for why the electronic structure of the kagome lattice might be interesting by studying a simple tight-binding model. Chapter 3 focuses on presenting the existing phenomenological Landau theory for CDW-like structural transitions in AV_3Sb_5 and extending it to shandites $M_3A_2Ch_2$ which have slightly different symmetries. The aim is to compare these systems and identify symmetry-related factors that may determine the potential for hosting a CDW phase. In Chapter 4 we give a quick introduction to DFT, which we then employ in Chapter 5, to study some of the specific materials we mentioned. By dissecting the materials' structures, we aim to shed light on the underlying mechanisms governing the CDW phase and pave the way for future research in this field.

Chapter 2

The kagome lattice

Kagome metals AV_3Sb_5

In 2019, a new family of materials AV_3Sb_5 containing kagome layers of vanadium was synthesized [16] and later found to be superconducting at $T \sim 1-3$ K [17–19]. Using crystallography language, we describe their crystal structure by labeling the atomic coordinates in the unit cell with their *Wyckoff positions*. Using this convention[1], the atomic coordinates and multiplicities are determined by only using a letter (some lower symmetry sites could also require one or more parameters). As shown in Figure 2.1a, these compounds crystallize in the $P6/mmm$ space group, where the V atoms are at the three Wyckoff positions g. The vanadium kagome lattice is sandwiched in between two layers of antimony Sb2 at the four positions h that form honeycomb lattices. Another antimony Sb1 is contained in the same plane as the V kagome and is at the position c, forms a simple triangular lattice. Moreover, these layers are intercalated by triangular lattices of the alkali atom A = K,Rb,Cs, sitting at the position a.

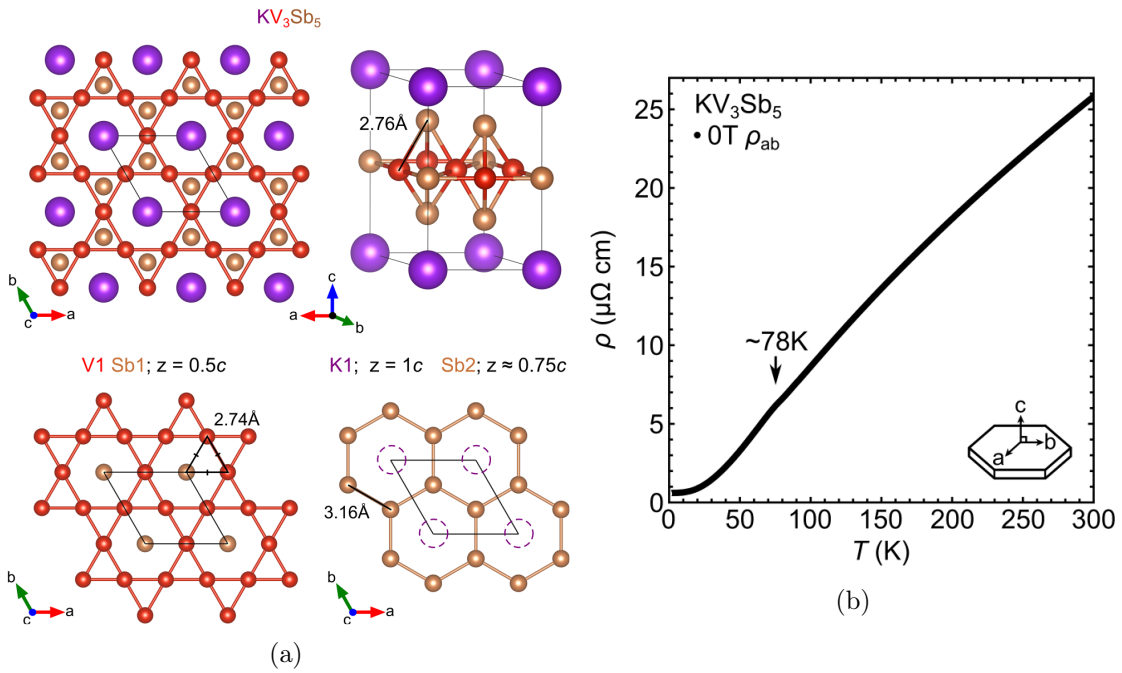

Figure 2.1: (a) Crystal structure of the AV_3Sb_5 family, with the alkali atom in purple, the vanadium ones in red and the antimony in gold. The distances measured in Å specifically refer to KV_3Sb_5. Figures adapted from Reference [16]

[1]For each space group, the table of all possible Wyckoff positions are determined by symmetry and can be found on the Bilbao Crystallographic Server [20].

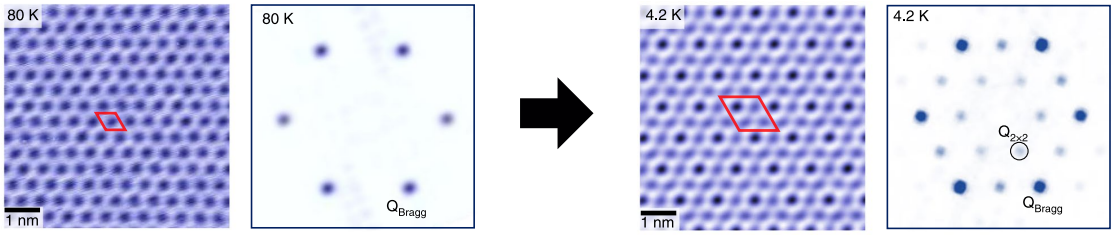

Figure 2.2: STM topography of an antimony Sb2 cleaved surface and respective Fourier transform, for two different temperatures. On the left, the high temperature phase, with a small unit cell represented with red lines and that corresponds in reciprocal space to a hexagonal BZ indicated by six Bragg peaks. On the right, the low temperature phase with a doubled (2x2) unit cell that in reciprocal space corresponds to a smaller BZ, signaled by six new Bragg peaks appearing. Figure adapted from Reference [21]

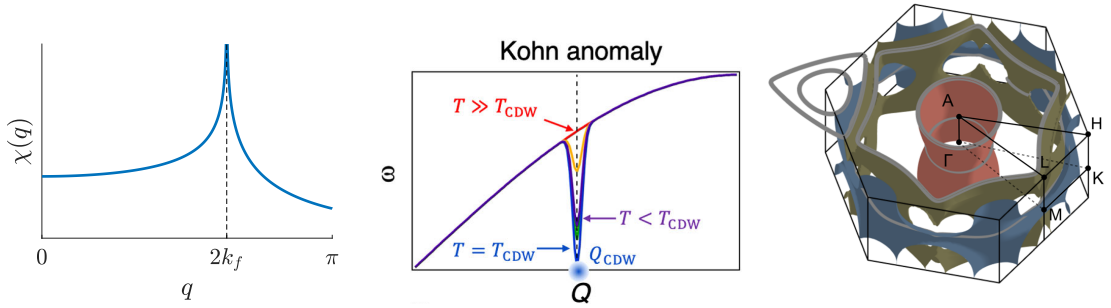

(a) (b) (c)

Figure 2.3: (a) Bare electronic susceptibility for a free electron gas on a 1D chain. The function diverges at the nesting vector. (b) In a Peierls unstable system, if the electrons are coupled to the lattice an acoustic phonon mode will become unstable at the nesting vector. Figure adapted from Ref. [24]. (c) Fermi surface calculated with DFT, which resembles the one obtained with ARPES. Figure adapted from Ref. [25].

Since their initial discovery, these materials have attracted considerable attention due to their intriguing properties. Other than superconductivity, one remarkable feature that has been observed and that we want to focus on, is an anomaly in various transport-related quantities at temperatures around $T \sim 80 - 100$ K. One such quantity is the in-plane resistivity, as depicted in Figure 2.1b. Detailed investigations using scanning tunneling microscopy (STM) topography maps [21] have revealed a connection between this anomaly and a structural transition occurring within the material. During this transition, the unit cell undergoes a doubling in both in-plane directions, as illustrated in Figure 2.2. Moreover, it also experiences a doubling or quadrupling in the out-of-plane direction [22]. This structural transformation gives rise to a distinct phase known as a Charge Density Wave (CDW), believed to originate from an electronic instability within the material. A theoretical model commonly used to explain this type of phenomenon in one-dimensional systems is the Peierls instability [23], which is driven by Fermi surface nesting: in a 1D chain, the bare electronic susceptibility for an electron gas diverges at the nesting vector $2k_F$. This purely electronic instability also renders the lattice unstable, causing a softening of an acoustic phonon mode at $q = 2k_F$ known as a Kohn anomaly. In the stable configuration, the unit cell doubles and a gap opens at the Fermi level in the electronic spectrum. In two-dimensional layered materials, however, the CDW picture could become more intricate.

In AV_3Sb_5, Fermi surface nesting may not be enough to cause an electronic instability. Angle resolved photoemission spectroscopy (ARPES) measurement have indeed detected

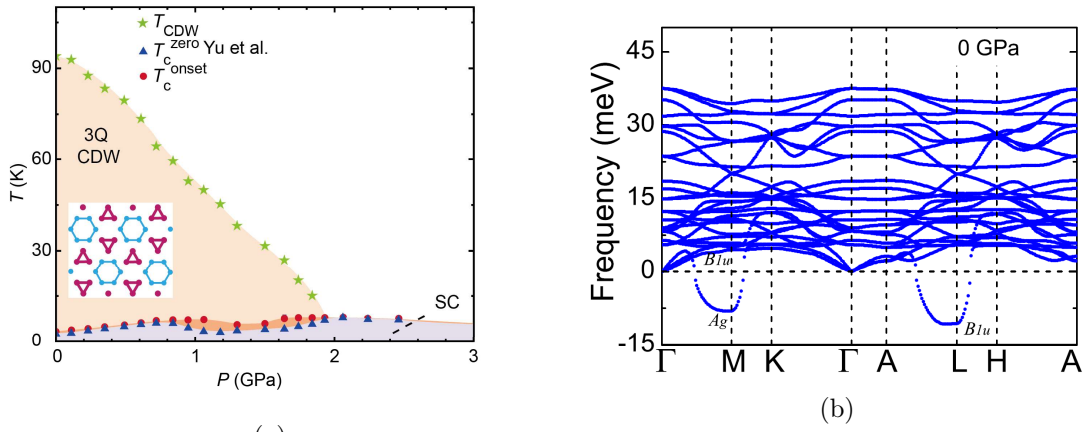

(a) (b)

Figure 2.4: (a) Experimental phase diagram for CsV_3Sb_5, figure adapted from Ref. [32]. (b) Phonon spectrum obtained from first principles, adapted from Ref. [33]. Imaginary frequencies are represented as negative for easy visualization. A heuristic explanation for why imaginary frequencies indicate an unstable structure can be found in the next chapter.

a Fermi surface formed by a Γ pocket and a quasi-two-dimensional hexagonal sheet with vertices on the $M - L$ lines, matching DFT calculations [25], so that the electronic instability could, in principle, be caused by the nesting of this Fermi surface by the **M** vector (see Figure 2.3c). In the low temperature CDW phase, ARPES is also able to measure multiple gaps opening [26]. Most experimental evidences diverge from the simple Peierls picture though, for example x-ray inelastic scattering measurements do not see any acoustic phonon anomaly [24], while coherent phonon spectroscopy predicts the condensation of three optical phonon modes [27]. Moreover, there has been evidence of unusually large AHE [7], time reversal symmetry breaking [28, 29] and 3-fold rotation symmetry breaking [30] in the CDW phase, which have been speculated to stem from local loop currents [9, 31].

The AHE is a phenomenon where a material exhibits a transverse voltage perpendicular to an applied electric current and an external magnetic field, even in the absence of any magnetic field gradient. Unlike the ordinary Hall effect, which arises from the Lorentz force acting on moving charges in the presence of a magnetic field, the AHE is usually associated with the presence of spin-orbit coupling and magnetic ordering in the material. Its presence in AV_3Sb_5 is compelling, since these materials don't appear to be magnetically ordered, and further point to an unconventional (non-Peierls) mechanism driving the CDW.

AV_3Sb_5 offers an intriguing platform for investigating the interplay between electron-phonon and electron-electron interactions. Its pressure-temperature phase diagram, depicted in Figure 2.4a, exhibits a dual-dome structure for superconductivity [6, 34] and the charge order of CDW gets monotonically suppressed under increasing pressure. Several studies have attempted to reproduce the superconductivity phase diagram using DFT [33, 35, 36]. While conventional electron-phonon driven superconductors can be analyzed using methods like Eliashberg theory [37, 38] or the more straightforward McMillan formula [39] to estimate the critical temperature from first-principles, whether these approaches are sufficient or not remains a topic of debate. Regarding the CDW, previous DFT simulations have successfully predicted the lattice instability (shown by the imaginary frequencies in Figure 2.4b) and its pressure dependence [33, 40] and point to strong electron-phonon coupling.

To gain a deeper understanding of the superconductivity exhibited in these materials, it is crucial to clarify the symmetry of the CDW phase from which the superconducting phase originates. In Chapter 3 we will explain why the imaginary phonon eigenvalues indicate a

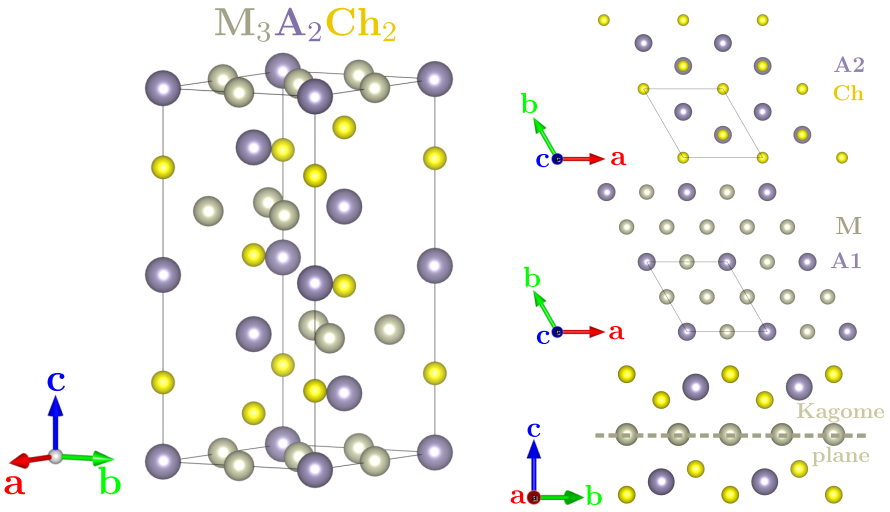

Figure 2.5: Conventional unit cell of the Shandite structure, containing three kagome layers. The kagome atoms are colored in grey.

lattice instability and we will present a phenomenological symmetry-based theory that has been recently proposed [41]. This theory can describe the in-plane and out-of-plane unit cell doubling (i.e., the structural transition) but remains agnostic about the microscopic nature of the order parameter. To get a better insight into what is the role of electronic degrees of freedom and their interplay with the lattice, we will produce and show the results of some of our own DFT calculations in Chapter 5. Moreover, we will compare these materials to the shandites, which we introduce in the next section.

Shandites $M_3A_2Ch_2$

Shandite is the name given to the compound with chemical formula $Ni_3Pb_2S_2$, discovered in the late 1940s [42]. Several compounds with the same crystal structure $M_3A_2Ch_2$, shown in Figure 2.5, have been synthesized in the past decades, and are now typically called shandites or half antiperovskites [43–47]. In this formula, M generally refers to a transition metal, A to a post-transition metal and Ch is a chalcogenide.

In these crystals, which have space group $R\bar{3}m$ (No. 166), the kagome layers are formed by the three M atoms sitting at the Wyckoff position e. The kagome lattice is coordinated by a triangular lattice of A1 atoms at the a position, and is intercalated by an additional A2 atom at the b position and two apical Ch atoms at the c position.

We will examine more in detail the arrangement of kagome layers in this crystal structure in Chapter 3, for the moment we just notice that the three major differences between $M_3A_2Ch_2$ and AV_3Sb_5 are: (1) the inter-layer distances in shandites are typically much smaller (around half as much as in the V-based kagome metals); (2) the layers are not repeating in a direction perpendicular to the layer itself, but are slightly shifted, such that it takes 3 layers to get a conventional unit cell with c axis perpendicular to the ab plane (see left panel of Figure 2.5); (3) the system does not posses six-fold rotational symmetry, both because of the shifted vertical stacking and because of the configuration of the apical ions above and below each kagome triangle. While in AV_3Sb_5 the Sb2 antimony act as the apical ions and lie on the same plane, forming two honeycomb lattices, in $M_3A_2Ch_2$ the apical ions do not lie on the same plane and are alternating M2 atoms and Ch atoms (see bottom right panel of Figure 2.5).

The mineral $Rh_3Pb_2S_2$ was discovered in 1983. Subsequently, the series $Rh_3A_2S_2$, where A represents In, Sn, Tl, and Pb, has been also studied and found to possess a

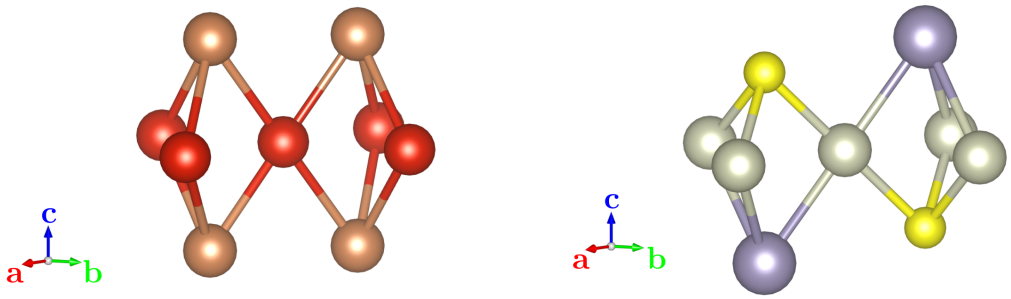

(a) (b)

Figure 2.6: Comparison of the arrangement of apical ions over the kagome triangles in: (a) the kagome metals AV_3Sb_5 where the apical ions are the antimony Sb2 atoms; (b) the shandites $M_3A_2Ch_2$ where the apical ions are alternating M2 atoms and Ch atoms and have different distances from the kagome plane.

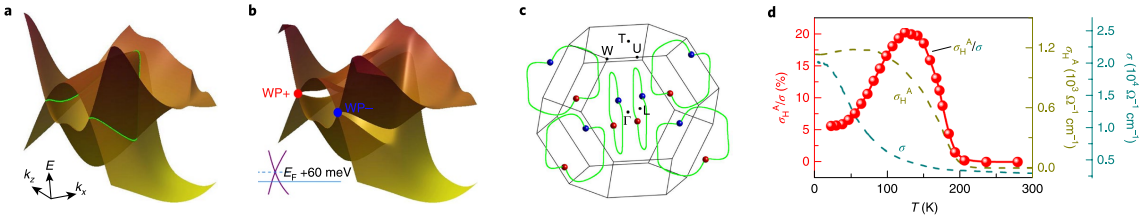

Figure 2.7: Weyl semimetal nature of $Co_3Sn_2S_2$ and AHE. Figure adapted from Ref. [49]. (a) Two bands are crossing over an entire line, called the nodal line. (b) The degeneracy gets lifted along the whole line other than in the two Weyl points. (c) Six couples of Weyl points are found around the BZ. (d) The anomalous Hall angle, defined as the ratio between the anomalous Hall conductance and the full conductance, as a function of temperature. The angle reaches approximately 20% around 120 K, a value that is considered *giant* since it is an order of magnitude larger than in usual ferromagnets.

shandite structure with kagome layers composed of rhodium atoms [46].

Recently, many works have focused on investigating the properties of ferromagnetic $Co_3Sn_2S_2$, which has been found to exhibit a giant AHE. This effect is believed to arise from the compound's speculated Weyl semimetal characteristics [48–51], shown in Figure 2.7. In a typical semimetallic system, the valence and conduction bands overlap and can become degenerate along an entire line referred to as the nodal line. However, in systems lacking inversion symmetry, the introduction of spin-orbit coupling can break this degeneracy along the entire line, except for two specific points known as Weyl points. These Weyl points are found to be monopoles of Berry phase curvature and their existence can even be predicted through first principles [52]. The emergence of Weyl fermions at these points leads to chiral excitations, which could potentially explain the unconventional behavior of electron flow observed under a magnetic field, as measured by the AHE.

Furthermore, certain shandite compounds with palladium kagome lattices have also been examined. For instance, $Rh_3Pb_2S_2$ has been discovered to exhibit superconductivity under high pressures [14] and has been theoretically investigated in relation to topological phonon excitations [15].

Shandites provide a versatile platform encompassing various materials. In the subsequent chapter, we will delve into the study of the layered kagome structure of shandites and extend the phenomenological theory of the CDW to these materials. Notably, no shandite compound exhibiting a CDW that doubles the unit cell has been discovered thus far, making it intriguing to examine the theoretical feasibility of such a phenomenon from a structural standpoint. Furthermore, in Chapter 5, we will employ DFT simulations to gain

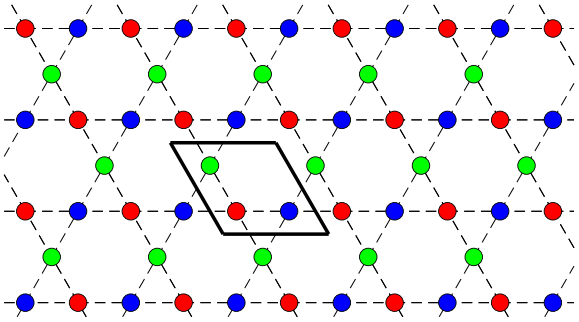

Figure 2.8: The kagome lattice with the three atom species in different colors. The unit cell is highlighted with black solid lines.

further insights into the electronic properties of these compounds and their relationship with the lattice.

Tight-binding model

Let's shift our attention away from specific material examples and take a more abstract approach to the kagome lattice. While our main emphasis is on the lattice structure itself, we will briefly introduce a simple tight-binding model to gain insight into the behavior of electrons within this lattice. In cartesian coordinates, we write the primitive translation vectors of a hexagonal Bravais lattice $\mathbf{R}$ as

$$\mathbf{t}_1 = a\begin{pmatrix}1\\0\end{pmatrix}, \qquad \mathbf{t}_2 = a\begin{pmatrix}-1/2\\\sqrt{3}/2\end{pmatrix}, \qquad \mathbf{R} = n_1\mathbf{t}_1 + n_2\mathbf{t}_2\,, \tag{2.1}$$

where n_1, n_2 are integers. For kagome, the positions of the three atomic sites inside the unit cell are

$$\mathbf{d}_A = \begin{pmatrix}0\\0\end{pmatrix}, \qquad \mathbf{d}_B = \frac{1}{2}\mathbf{t}_1, \qquad \mathbf{d}_C = \frac{1}{2}\mathbf{t}_2, \tag{2.2}$$

which are also said to form the three sub-lattices.

Using second quantization formalism, we can write down electronic field creation/annihilation operators $\hat{c}^\dagger_{\mathbf{R}\alpha}, \hat{c}_{\mathbf{R}\alpha}$ which create/annihilate an electron in the unit cell $\mathbf{R}$ at site α[2]. To write a tight-binding Hamiltonian, we assign a probability amplitude $-\mu$ for the electron to remain in the same site and a probability amplitude $-t$ that it could hop, both

- to its nearest neighboring sites, in the same unit cell $(\mathbf{R}, \alpha) \leftrightarrow (\mathbf{R}, \beta)$,
- to its nearest neighboring sites, in neighboring unit cells $(\mathbf{R}, \alpha) \leftrightarrow (\mathbf{R}', \beta) = (\mathbf{R} - 2\mathbf{d}_{\alpha\beta}, \beta)$,

where $\mathbf{d}_{\alpha\beta} = \mathbf{d}_\alpha - \mathbf{d}_\beta$. In terms of field operators we have

$$\hat{H} = -t\sum_{\mathbf{R}}\sum_{\alpha\neq\beta}\left(\hat{c}^\dagger_{\mathbf{R}\alpha}\hat{c}_{\mathbf{R}\beta} + \hat{c}^\dagger_{\mathbf{R}\alpha}\hat{c}_{\mathbf{R}-2\mathbf{d}_{\alpha\beta}\beta}\right) - \mu\sum_{\mathbf{R}\alpha}\hat{c}^\dagger_{\mathbf{R}\alpha}\hat{c}_{\mathbf{R}\alpha}\,. \tag{2.3}$$

If the lattice has periodic boundary conditions, the system is translationally invariant and the conjugate momentum $\mathbf{k}$ is a good quantum number. For any kind of 2D triangular system, the Brillouin Zone (BZ) is a hexagon, given by the Wigner-Seitz cell in the

[2]For the moment we omit the spin index, which is redundant in this simple case since the tight-binding Hamiltonian is diagonal in spin.

reciprocal lattice spanned by

$$\begin{aligned} \mathbf{G} &= m_1\mathbf{g}_1 + m_2\mathbf{g}_2\,, \qquad & m_1, m_2 &\in \mathbb{Z}\,, \\ \mathbf{g}_1 &= \frac{2\pi}{a}\left(1,\, 1/\sqrt{3}\right), \qquad & \mathbf{g}_2 &= \frac{2\pi}{a}\left(0,\, 2/\sqrt{3}\right)\,. \end{aligned} \tag{2.4}$$

Using group theory language, every point $\mathbf{k} \in$BZ labels one of the one-dimensional irreducible representations (irreps) of the translation group, which have character $e^{i\mathbf{k}\cdot\mathbf{R}}$. Projecting the operators $\hat{c}_{\mathbf{R}\alpha}$ in those irreps, is then equivalent to doing a Fourier transform

$$\hat{c}_{\mathbf{R}\alpha} = \frac{1}{\sqrt{N}} \sum_{\mathbf{k}} \hat{c}_{\mathbf{k}\alpha} e^{i\mathbf{k}\cdot\mathbf{R}} \tag{2.5}$$

so that the Hamiltonian becomes

$$\hat{H} = \sum_{k} \sum_{\alpha\beta} \hat{c}^{\dagger}_{\mathbf{k}\beta} \mathcal{H}_{\alpha\beta}(\mathbf{k}) \hat{c}_{\mathbf{k}\alpha}\,, \tag{2.6}$$

$$\mathcal{H}(\mathbf{k}) = \begin{bmatrix} -\mu & -t[1+e^{-2i\mathbf{k}\cdot(\mathbf{d}_{BA})}] & -t[1+e^{-2i\mathbf{k}\cdot(\mathbf{d}_{CA}]} \\ -t[1+e^{-2i\mathbf{k}\cdot(\mathbf{d}_{AB})}] & -\mu & -t[1+e^{-2i\mathbf{k}\cdot(\mathbf{d}_{CB})}] \\ -t[1+e^{-2i\mathbf{k}\cdot(\mathbf{d}_{AC})}] & -t[1+e^{-2i\mathbf{k}\cdot(\mathbf{d}_{BC})}] & -\mu \end{bmatrix}. \tag{2.7}$$

The Hamiltonian is now diagonal in $\mathbf{k}$ space, but not in sub-lattice space. Further diagonalization in sub-lattice space leads to finding a set of three energies for every $\mathbf{k}$ point, which can be plotted through a high symmetry path in the BZ to give the band structure for this tight-binding model, shown in Figure 2.9. The unitary matrix that takes us from sub-lattice space to band space can be written as

$$\mathrm{diag}(\varepsilon_{1\mathbf{k}}, \varepsilon_{2\mathbf{k}}, \varepsilon_{3\mathbf{k}}) = U(\mathbf{k})\mathcal{H}(\mathbf{k})U^{\dagger}(\mathbf{k})\,, \tag{2.8}$$

$$U(\mathbf{k}) = \begin{bmatrix} u_{1A}(\mathbf{k}) & u_{2A}(\mathbf{k}) & u_{3A}(\mathbf{k}) \\ u_{1B}(\mathbf{k}) & u_{2B}(\mathbf{k}) & u_{3B}(\mathbf{k}) \\ u_{1C}(\mathbf{k}) & u_{2C}(\mathbf{k}) & u_{3C}(\mathbf{k}) \end{bmatrix}, \tag{2.9}$$

so that the three columns of this matrix are the eigenstates of $\mathcal{H}(\mathbf{k})$ associated with the three eigenvalues $\varepsilon_{i\mathbf{k}}$. The matrix elements $u_{i\alpha}$ are also called sub-lattice weights. We can interpret them as telling how much of the electron's wavefunction is localized on one of the three sites, for a given band and $\mathbf{k}$ vector. In Figure 2.9 we represent the modulus squared of these weights on the band structure, by interpolation of RGB colors.

Although the overall system is 6-fold symmetric, depending on the $\mathbf{k}$-point, the Hamiltonian $\mathcal{H}(\mathbf{k})$ may not be commuting with every element of the point group D_6, but with just a (normal) subgroup of it. Formally, $\mathcal{H}(\mathbf{k})$ only commutes with the little group of $\mathbf{k}$. The little group of D_6 at $\mathbf{k}$ is the subset of symmetry operations of D_6 that leave $\mathbf{k}$ invariant, modulo a reciprocal lattice primitive translation. For example, the little group at $\mathbf{k} = (0,0)$, the $\mathbf{\Gamma}$ point, is D_6, but the little group at $\mathbf{k} = (\frac{1}{2}, 0)$, the $\mathbf{M}$ point, is D_2. The diagonalization of $\mathcal{H}(\mathbf{k})$ is equivalent to projecting onto the irreps of the little group at $\mathbf{k}$. One of the early developments of band theory, was the realization that the little group can give information about band crossing and degeneracies. For example, since the little group at $\mathbf{k} = (\frac{1}{3}, \frac{1}{3})$, the $\mathbf{K}$ point, is D_3 and it allows for a two-dimensional irrep, we can have a band crossing at $\mathbf{K}$, where the two degenerate eigenvectors transform like the two columns of the irrep. In contrast, at $\mathbf{M}$ the little group is D_2, which only allows for one-dimensional irreps, so all three bands in our tight-binding model should be non-degenerate by symmetry at $\mathbf{M}$.

In this simple model, which only accounts for the kinetics of the electrons but no Coulomb interactions, the band structure presents a completely flat band and two bands that cross in a Dirac cone at K, while also having two saddle points points at M. These

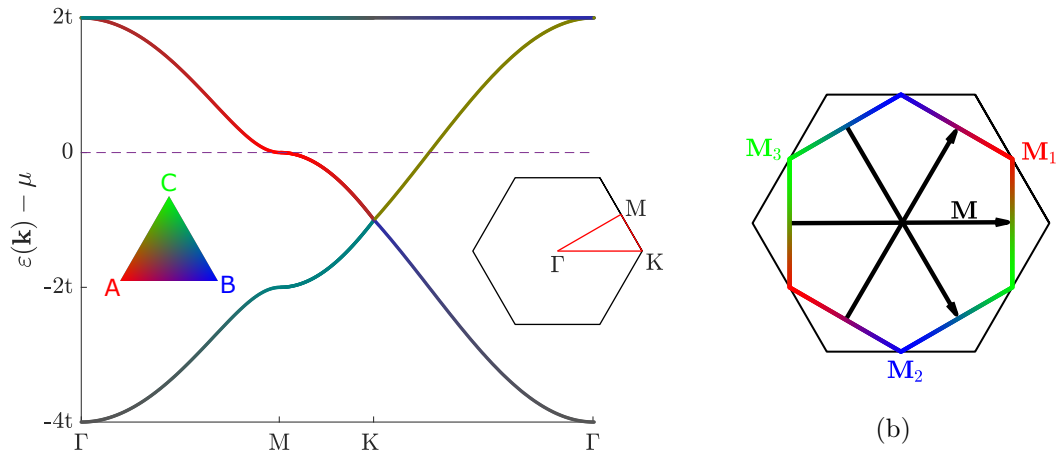

(a) (b)

Figure 2.9: (a) Band structure for a tight-binding model on the kagome lattice, having chosen a high symmetry path in the hexagonal Brillouin Zone, shown on the right inset. The left inset shows the correspondence between RGB colors and sub-lattice weight. (b) When the Fermi level lies on top of the saddle point, the Fermi surface is a regular hexagon. The colors indicate the sub-lattice weight and demonstrate the phenomenon of sub-lattice interference: at the **M** points there is only one sub-lattice specie. Moreover, the Fermi surface is perfectly nested by the **M** vectors.

saddle points are also referred to as van Hove singularities (vH), since the density of states at those energies should be singular with a logarithmic divergence. Of these vH points, the bottom one is called m-type (mixed) because it always has an equal mixture of two sub-lattice weights, while the top one is called p-type (pure), since it always come with only one of the three sub-lattice weights being different than zero. The hexagonal BZ has only three nonequivalent M points (said to form the *star* of **M**, the other three are obtained by reciprocal lattice translations), and at the specific M point plotted in Figure 2.9 the p-type vH is associated with the A sub-lattice, so it is red, while the bottom one is a mixture of B and C, so it is between green and blue. If we were to look at the other two nonequivalent M points, we would see the same thing happening, but with the colors inverted.

In Figure 2.10 we show how the (modulus squared of the) wavefunction would look like at the two kinds of vH points, in a simple scenario where s-orbital electrons are used as a basis for the tight-binding model. At the p-type vH point, the wavefunction is completely localized on just one of the three sites, while at the m-type vH point it is completely localized on two of the three sites.

This phenomenon is sometimes referred to as *sub-lattice interference* [53]. More involved theoretical investigations, such as extended Hubbard models [3–5] and Renormalization group analyses [31], have introduced interactions to the kagome tight-binding Hamiltonian to model the Coulomb interaction. It is widely believed that having the Fermi level close to the p-type vH point could promote electronic Fermi surface instabilities that can lead to a CDW ground state in these models, similar to the one observed in AV_3Sb_5. The instability could be strictly related to nesting: as shown in Figure 2.9b, at the vH filling, the Fermi surface is a regular hexagon that is perfectly nested by the **M** vectors and the divergence of the density of states could lead to enhanced scattering between electrons close to the saddle point. Notably, the CDW in the kagome metals seems to be modulated exactly by the **M** vectors.

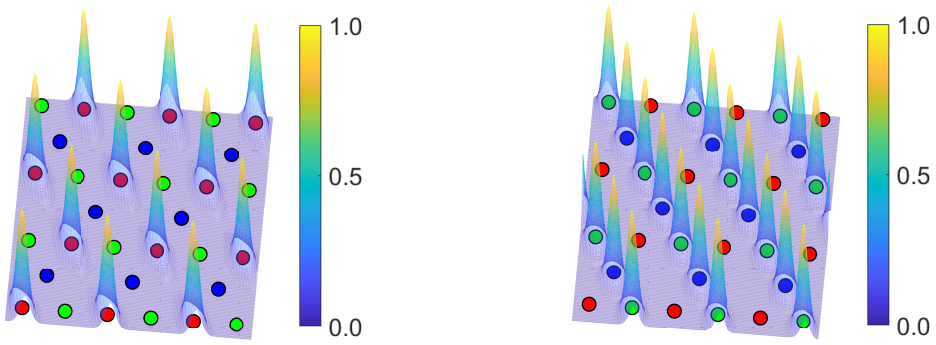

p-type m-type

Figure 2.10: Magnitude of the wavefunctions corresponding to the two kinds of saddle points/vH singularities: p-type, where the wavefunction is completely localized on just one of the three sites; m-type, where the wavefunction is completely localized on two of the three sites.

It is still heavily debated if in real systems like AV_3Sb_5 the CDW instability can be purely electronic or is actually stabilized by the electron-phonon coupling, in a way that reminds the Peierls mechanism. In the upcoming Chapter we will focus solely on the structural properties, but we will revisit these electronic properties and the Fermi surface nesting in Chapter 5.

Chapter 3

Landau theory for structural transitions

In Landau theory, a phase transition is a process in which a system loses some of its symmetries. Let us assume that, in the high symmetry (disordered) phase, there is a group G describing all of the symmetry operations that leave the system invariant. We call *order parameter* ψ a quantity whose thermodynamical average is zero in the disordered phase, and it is different than zero in the ordered phase. Landau's idea was that near the critical temperature for the phase transition, the order parameter would be small and the free energy functional could be Taylor expanded in powers of this small parameter. In general, one can predict by symmetry what terms are allowed in a Taylor expansion, for example the function $\cos(x)$ is even under the inversion $x \to -x$, so its Taylor expansion will only contain even powers. Using groups and representation theory, we can generalize this concept to discrete groups that contain more symmetry operations than just the inversion, and predict what terms will be allowed in the free energy expansion. An order parameter will transform under some representation Γ of the group G, so that in principle, we can know the functional form of the free energy and we can classify all of the low symmetry (ordered) phases that the system can enter, by listing all of the irreducible representations that the order parameter can transform under.

In the following, we are interested in how kagome lattice layers hosted in a material can undergo a structural transition, i.e., spontaneously break some of the space group symmetries. This is the phenomenon observed in the kagome metals AV_3Sb_5 CDW phase: some kind of electronic charge-bond order is accompanying a structural transition. In a normal structural transition, one can imagine the order parameter to be the average displacement $\psi = \langle \Delta\tau_\kappa \rangle$ of some of the atoms κ in the unit cell with respect to their equilibrium positions τ^0_κ. In the disordered phase the atoms have some fluctuations around their equilibrium positions (phonon modes), but they average to zero. In the ordered phase, some of these fluctuations get frozen in the crystal structure, lowering the symmetries of the system, and we say that particular order has *condensed*. Condensation of an order parameter causes the system to end up having a group of symmetries H, which is a (normal) subgroup of G. For a space group, the irrep is specified by picking a point in the BZ, choosing an element of its star (the set of points obtainable by point group operations and inequivalent by reciprocal lattice translations) and one of the irreps of the little group (introduced previously) at that point.

Once we have identified the specific symmetries of an order parameter ψ, we can write down a free energy $\mathcal{F}[\psi]$ expansion for small ψ. Since the free energy has to have all of the symmetries of the system, it must transform under the trivial irrep Γ^{triv}, so the problem turns into the question of finding all the combinations of ψ (or its components, in case of multi-dimensional irreps) which transform like Γ^{triv}. In the case of space groups, the terms that can enter the free energy need to be both invariant under every point group

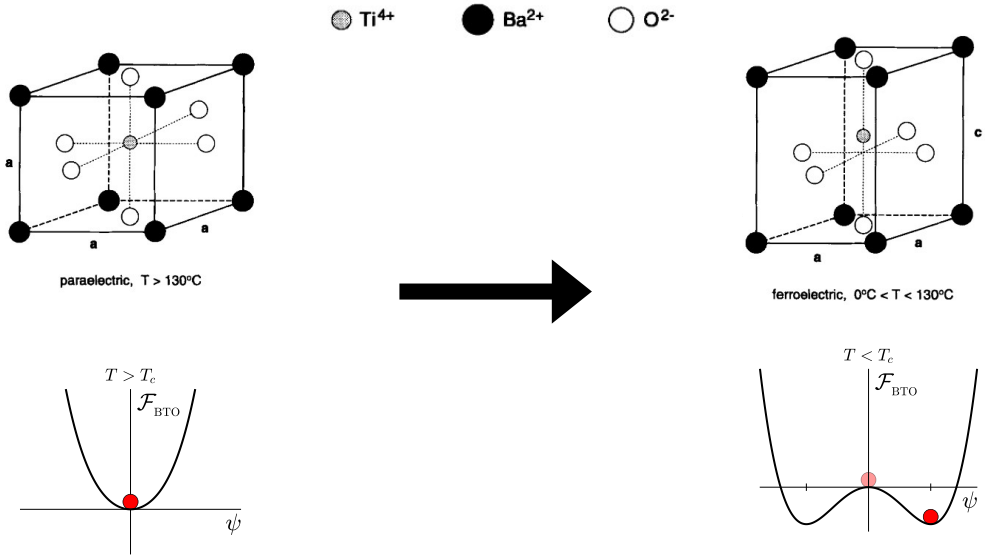

Figure 3.1: Ferroelectric phase transition in $BaTiO_3$. On the left: cubic phase, for $T > T_c$ the average titanium displacement is zero, with the stable system represented as a red ball sitting at the bottom of the curve. On the right: tetragonal phase, for $T < T_c$ the average titanium displacement is different than zero. The red ball represents the stable tetragonal system, while the shaded red ball represents the unstable cubic system and is sitting at the saddle point, where the curvature of the free energy is negative.

operation *and* invariant under all Bravais lattice translations (carry zero momentum).

Example - $BaTiO_3$ Before moving to kagome, let us examine the simpler case of perovskite barium titanate $BaTiO_3$, which undergoes (among others) a ferroelectric structural transition from a cubic to a tetragonal crystal system. In the cubic phase, the space group is $Pm\bar{3}m$ (No. 221) and the titanium atom sits at the center of the unit cell, Wyckoff position a, surrounded by oxygen atoms sitting at the 3 inequivalent sites d. As we will show in Chapter 4, it is possible to use DFT to calculate the dynamical matrix in the Born-Oppenheimer harmonic approximation. In the case of cubic $BaTiO_3$, we can find that at the $\mathbf{q}$ vector Γ, the center of the BZ, the dynamical matrix has a negative eigenvalue: a phonon frequency is imaginary.

Since the dynamical matrix is the hessian of the Born-Oppenheimer energy surface with respect to the atomic displacements, having a negative eigenvalue means that the system can decrease its energy by distorting in the "direction" described by the corresponding eigenvector, so it is unstable. The eigenvalues of the dynamical matrix are the phonon frequencies squared, so a negative eigenvalue corresponds to an imaginary phonon frequency[1]. Using the SMODES tool in the ISOTROPY software package [54], we can compare this eigenvector (i.e., the phonon mode obtained with DFT) to the irreducible representations of the point group of this system, O_h. We find that the phonon mode, which describes a displacement of the titanium atoms along z and the oxygen ones in the opposite direction, transforms like one of the columns of the Γ_4^- irrep.

We now have the ingredients to make a Landau theory. If we take the average displacement of the titanium atom to be the order parameter ψ, we know its symmetry properties, so we can determine the free energy expansion. Using the INVARIANTS tool [54], we find

[1]For more details on the dynamical matrix, which will be defined in equation 4.57, and the meaning of the Born-Oppenheimer approximation, see Chapter 4.

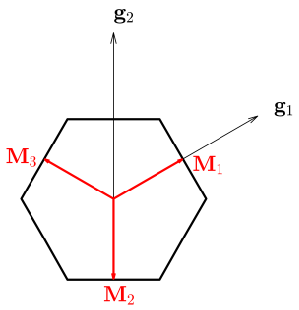

Figure 3.2: Hexagonal Brillouin Zone and star of the M vector.

the free energy up to fourth order to be

$$\mathcal{F}_{\mathrm{BTO}}[\psi] = \frac{a}{2}\psi^2 + \frac{b}{4}\psi^4$$

which is the most basic form of a Landau free energy. With the usual ansatz $a(T) \sim a(T - T_c)$, under the critical temperature the free energy has two non-zero minima, which describe the freezing in of the lattice phonon mode. Under the critical temperature, the system can decrease its energy by distorting and changing its structure, such that the average titanium displacement is different than zero. This new stable structure is a tetragonal system with space group $P4mm$ (No. 99).

As we will see, DFT is calculating ground state $T = 0$ K properties, so at that temperature the cubic phase of $BaTiO_3$ is sitting at the saddle point of the energy curve shown in the right of Figure 3.1. The takeaway point is: finding imaginary phonon frequencies, signals an unstable crystal structure.

2D - One kagome layer

For a single kagome layer, let us consider $G = D_{6h} \times \mathbf{T}$ as the group of symmetries for the system, where the point group D_{6h} includes 6-fold rotations, two mirrors and inversion and $\mathbf{T}$ is the group of all discrete translations allowed in a triangular Bravais lattice. From now on, we indicate with bold letters the points in the Brillouin Zone and italic letters the irreps of the little group at that point. As seen Chapter 2, experiments and previous DFT calculations indicate that the CDW in AV_3Sb_5 is modulated by the $\mathbf{M}$ vector, so we focus our analysis on this point. The little group at $\mathbf{M}$ is D_{2h}, which has eight one-dimensional irreps, four even and four odd under inversion (see the character table 3.2 at the end of the chapter). Furthermore, there are three vectors in the star of M, see Figure 3.2, with coordinates

$$\mathbf{M}_1 = \pm\frac{1}{2}\mathbf{g}_1\,, \qquad \mathbf{M}_2 = \pm\frac{1}{2}\mathbf{g}_2\,, \qquad \mathbf{M}_3 = \pm\frac{1}{2}(\mathbf{g}_1 - \mathbf{g}_2)\,, \tag{3.1}$$

which means that the eight space group irreps, labeled $M^{\pm}_{1,2,3,4}$ are all three dimensional: an order parameter transforming like one of these irreps has three components.

M_1^+ irrep Let us take a look at the Landau theory for an order parameter $\psi = (\psi_1, \psi_2, \psi_3)$ transforming like the M_1^+ irrep, the trivial irrep of the little group at the M point. In Figure 3.3 we show how a lattice distortion (or a frozen phonon mode) transforming like one of the three components of ψ looks like. Condensation of one of these three orders would cause a point group symmetry breaking $D_{6h} \to D_{2h}$ and breaking of the translational symmetry in one of the two primitive directions (2x1 doubling of the unit cell). We refer to that order as a stripe phase. Up to fourth order we obtain the free energy expansion

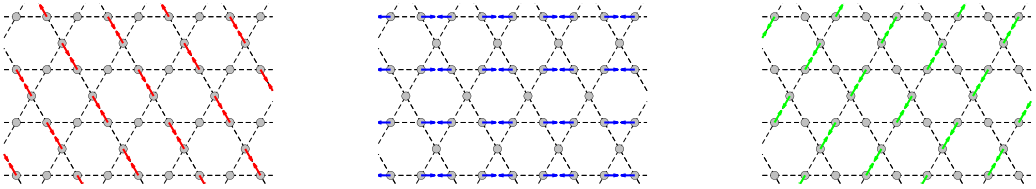

$\psi \propto (1,0,0)$ $\psi \propto (0,1,0)$ $\psi \propto (0,0,1)$

Figure 3.3: Lattice distortions corresponding to the three components of the M_1^+ irrep.

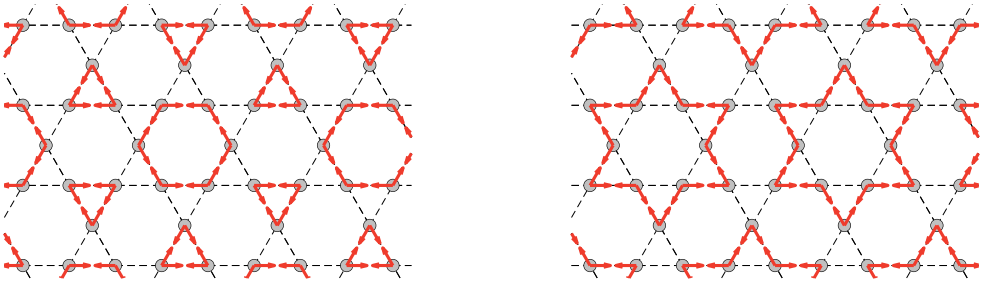

$\psi_{TriHex} \propto (1,1,1)$ $\psi_{SD} \propto (1,-1,1)$

Figure 3.4: Lattice distortions corresponding to the TriHex and SD patterns. They preserve all the point group symmetries of D_{6h} but break the original discrete translational symmetry of the lattice: now we need to double both the primitive translation vectors to preserve it.

$$\mathcal{F}_{M_1^+}[\psi] = \frac{\alpha}{2}\psi^2 + \frac{\gamma}{3}\psi_1\psi_2\psi_3 + \frac{u}{4}\psi^4 + \frac{\lambda}{4}(\psi_1^2\psi_2^2 + \psi_1^2\psi_3^2 + \psi_2^2\psi_3^2)\,, \tag{3.2}$$

where $\psi^2 = \psi_1^2 + \psi_2^2 + \psi_3^2$. The trilinear term is remarkable, part of the reason why it is allowed is that the sum of all three $\mathbf{M}$ vectors is zero, so this term carries zero momentum. Furthermore it is easy to check, with the help of Figure 3.3, that all operations of the point group would leave this term invariant. Because of this trilinear term, the condensation of all three components of the order parameter is always energetically favored, no matter the sign of γ, since we can always make up for it changing the sign of one of the three components. If one of the three was zero, the trilinear term would vanish and increase the free energy. In Figure 3.4 we show how an order with all three components different than zero (and same magnitude) looks like. There are two cases: all three have the same sign, so the distortions form a so called Tri-Hexagonal pattern (TriHex)[2]; one has opposite sign than the other two, the distortions form a so called Star-of-David (SD) pattern. The condensation of one of these two orders would not break the point group symmetry, but would break the translational symmetry and cause a doubling of the unit cell in both the primitive directions (2x2).

As shown in [41], we can actually minimize the free energy to prove that the TriHex or SD phases are always favored with respect to the stripe phase. In the stripe phase, the order parameter would be e.g., $\psi_{stripe} = (M,0,0)$, so that the free energy for this configuration would be

$$\mathcal{F}_{M_1^+}[\psi_{stripe}] = \frac{\alpha}{2}M^2 + \frac{u}{4}M^4\,, \tag{3.3}$$

and we impose $u > 0$ so it remains bounded. The minima of this free energy are $M_0 = \pm\sqrt{-\alpha/u}$, such that we find the free energy for the stripe phase to be

$$\mathcal{F}_{stripe} = -\frac{\alpha^2}{4u}(T - T_M)^2\,, \tag{3.4}$$

[2]Sometimes, in the literature, this configuration is also referred to as the Inverse Star-of-David (ISD).

having used the standard ansatz that the temperature dependence of the quadratic coefficient is $\alpha(T) \approx \alpha(T - T_M)$ and $\alpha > 0$. In the TriHex/SD phase, instead, we would have a free energy

$$\mathcal{F}_{M_1^+}[\psi_{\mathrm{TriHex/SD}}] = \frac{\alpha}{2}M^2 + \frac{\gamma}{3}M^3 + \frac{3u_*}{4}M^4 \,. \tag{3.5}$$

We must also require $u_* = 3u + \lambda > 0$ for the free energy to be bounded. At the minimum, the value of this free energy is

$$\mathcal{F}_{\mathrm{TriHex/SD}} = \frac{K^2}{2592u_*^3}[54\alpha(T - T_M)u_* - \gamma K] \tag{3.6}$$

with $K = \gamma + \sqrt{\gamma^2 - 36\alpha(T - T_M)u_*}$, which crosses zero at

$$T_{3M} = \frac{2\gamma^2}{81\alpha u_*} + T_M \,, \tag{3.7}$$

so this critical temperature is always greater than T_M, if $\gamma \neq 0$.

Every other irrep An order parameter transforming like one of the seven other irreps of the little group at the **M** point, M_1^- and $M_{2,3,4}^{\pm}$, would give the free energy expansion

$$\mathcal{F}_{\Gamma \neq M_1^+}[\psi] = \frac{\alpha}{2}\psi^2 + \frac{u}{4}\psi^4 + \frac{\lambda}{4}(\psi_1^2\psi_2^2 + \psi_1^2\psi_3^2 + \psi_2^2\psi_3^2) \,, \tag{3.8}$$

which *does not* contain a trilinear term. None of these order could condense and just double the unit cell, without also breaking some of the point group symmetries.

3D - $P6/mmm$ space group

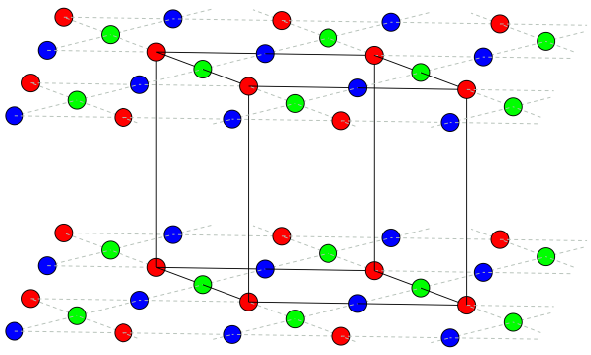

Figure 3.5: Two kagome layers in the $P6/mmm$ stacking. Black solid lines represent the unit cell defined by the primitive translations in 3.9.

The easiest way to stack kagome layers in three dimensions, is to just repeat the unit cell in the direction perpendicular to the kagome plane, such that we have a 3D unit cell given by the primitive translation vectors

$$\mathbf{t}_1 = a\begin{pmatrix}1\\0\\0\end{pmatrix} \,, \qquad \mathbf{t}_2 = a\begin{pmatrix}-1/2\\\sqrt{3}/2\\0\end{pmatrix} \,, \qquad \mathbf{t}_3 = c\begin{pmatrix}0\\0\\1\end{pmatrix} \,, \tag{3.9}$$

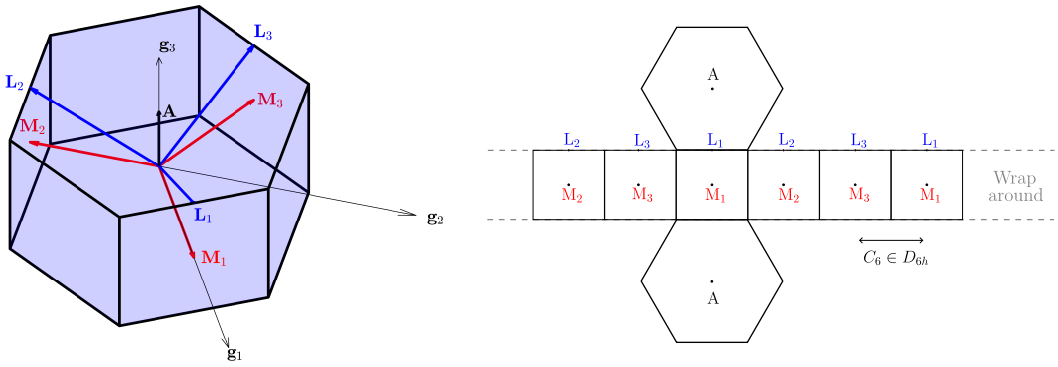

Figure 3.6: Brillouin zone for the $P6/mmm$ space group.

so that c is the inter-layer distance. This makes it so the system has the symmetries of the $P6/mmm$ space group (No. 191), with the three kagome sites being at the three inequivalent Wyckoff positions f. The name of the space group comes from the fact that the Bravais lattice is (hexagonal) Primitive and the system is 6-fold symmetric and invariant under two mirrors and inversion, so the point group is $.6/mmm$ or D_{6h} in the Schoenflies notation.

Given that the primitive translations are the same as in the 2D case, plus a third translation perpendicular to the firsts two, the Brillouin Zone is just a hexagonal prism, as shown in Figure 3.6. The primitive reciprocal lattice vectors are

$$\mathbf{g}_1 = \frac{2\pi}{a}\left(1, \frac{1}{\sqrt{3}}, 0\right), \qquad \mathbf{g}_2 = \frac{2\pi}{a}\left(0, \frac{2}{\sqrt{3}}, 0\right), \qquad \mathbf{g}_3 = \frac{2\pi}{c}\left(0, 0, 1\right). \tag{3.10}$$

Figure 3.6 also highlights the three vectors in the star of $\mathbf{M}$ in red and the three, so called, $\mathbf{L}$ vectors in blue. The $\mathbf{L}$ vectors can be obtained by just adding a $\frac{1}{2}\mathbf{g}_3$ component to the $\mathbf{M}$ vectors. Moreover, $\frac{1}{2}\mathbf{g}_3$ is known as the $\mathbf{A}$ vector, represented as a black arrow in Figure 3.6.

$$\begin{gathered} \mathbf{M}_1 = \frac{1}{2}\mathbf{g}_1\,, \qquad \mathbf{M}_2 = \frac{1}{2}\mathbf{g}_2\,, \qquad \mathbf{M}_3 = \frac{1}{2}(\mathbf{g}_1 - \mathbf{g}_2)\,, \\ \mathbf{L}_1 = \frac{1}{2}\mathbf{g}_1 + \frac{1}{2}\mathbf{g}_3\,, \qquad \mathbf{L}_2 = \frac{1}{2}\mathbf{g}_2 + \frac{1}{2}\mathbf{g}_3\,, \qquad \mathbf{L}_3 = \frac{1}{2}(\mathbf{g}_1 - \mathbf{g}_2) + \frac{1}{2}\mathbf{g}_3\,, \\ \mathbf{A} = \frac{1}{2}\mathbf{g}_3\,. \end{gathered} \tag{3.11}$$

M order parameter The symmetry analysis of the $\mathbf{M}$ point in this Brillouin Zone is the same as the 2D case in the previous section: there are three vectors in the star, the little group is D_{2h} and there are eight 1D irreps. Of these eight, only one (M_1^+) gives rise to a trilinear term in the free energy expansion, and the other seven do not. With a different notation, now we write the order parameter transforming like M_1^+ as $M = (M_1, M_2, M_3)$, whose components are represented as lattice distortions in Figure 3.7. Up to fourth order the free energy expansion in this order parameter is

$$\mathcal{F}_M = \frac{\alpha_M}{2}M^2 + \frac{\gamma_M}{3}M_1M_2M_3 + \frac{u_M}{4}M^4 + \frac{\lambda_M}{4}(M_1^2M_2^2 + M_1^2M_3^2 + M_2^2M_3^2)\,, \tag{3.12}$$

where $M^2 = M_1^2 + M_2^2 + M_3^2$ and $M^4 = (M^2)^2$. Similarly as in the 2D case, the stripe phase breaks rotational symmetry and reduces the space group to $Pmmm$ (No. 47), while also

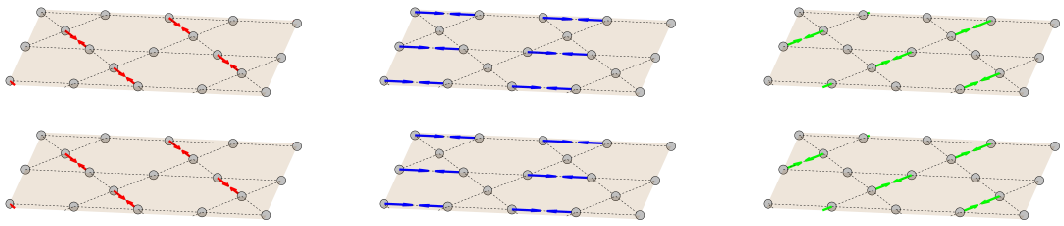

M_1 M_2 M_3

Figure 3.7: Lattice distortions corresponding to the three components of the M_1^+ irrep. Consecutive layers have exactly the same lattice distortions.

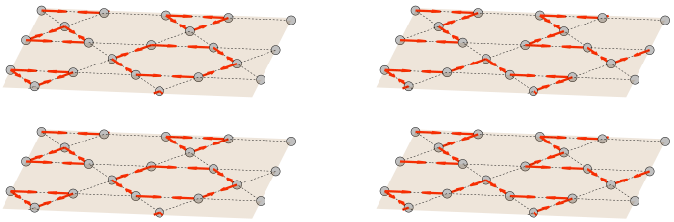

Tri-Hexagonal Star-of-David

Figure 3.8: Lattice distortions corresponding to the Tri-Hexagonal and Star-of-David configurations, where all three components of the M order parameter are condensing with the same magnitude. Consecutive layers have exactly the same lattice distortions, since **M** does not give any out-of-plane modulation.

doubling the unit cell in one direction (2x1x1). Because of the trilinear term though, the two possible ground states for this free energy are the Star-of-David or the Tri-Hexagonal configurations, repeating on every kagome layer, which double the unit cell in the two planar primitive directions (2x2x1) but preserve the space group $P6/mmm$.

L order parameter The symmetry analysis for the **L** point is a little easier: there are three vectors in its star, its little group is D_{2h}, but none of the irreps $L^{\pm}_{1,2,3,4}$ can give rise to a trilinear term allowed in the free energy. For an order parameter $L = (L_1, L_2, L_3)$ transforming like one of those eight irreps, the free energy up to fourth order looks the same, and it is

$$\mathcal{F}_L = \frac{\alpha_L}{2} L^2 + \frac{u_L}{4} L^4 + \frac{\lambda_L}{4} (L_1^2 L_2^2 + L_1^2 L_3^2 + L_2^2 L_3^2)\,. \tag{3.13}$$

There are two possible ground states for this free energy, which are determined by the sign λ_L: if $\lambda_L < 0$ it is energetically favorable for all three components (L_1, L_2, L_3) to condense and become different than zero; vice versa, if $\lambda_L > 0$ it is more favorable for just one component to condense and the other two to remain zero. We can prove this analitically by minimizing the free energy and finding the ground states $(L, 0, 0)$ and (L, L, L), where respectively the free energy takes values

$$\begin{aligned} \mathcal{F}_{1L} &= -\frac{\alpha_L^2 (T - T_L)^2}{4u_L}\,, \\ \mathcal{F}_{3L} &= -\frac{\alpha_L^2 (T - T_L)^2}{4u_L + \frac{4}{3}\lambda_L}\,, \end{aligned} \tag{3.14}$$

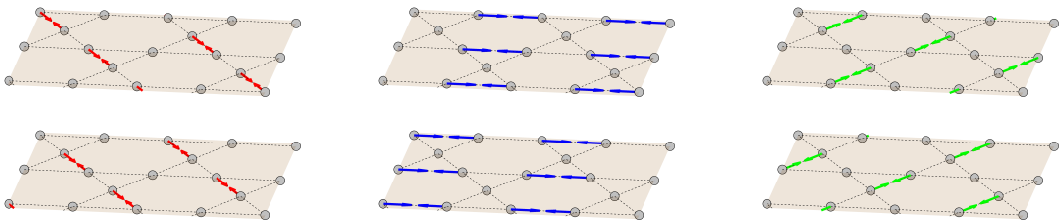

L_1 L_2 L_3

Figure 3.9: Lattice distortions corresponding to the three components of the L_2^- irrep. Differently from the components of M_1^+ in Figure 3.7, here consecutive layers have opposite lattice distortions.

where we assumed $\alpha_L \approx \alpha(T - T_L)$. A state with two condensed components e.g., $(L, L, 0)$, would always have a greater energy than these two. From these equations we can also see that for the free energy to be bounded we need $u_L > 0$ and $\lambda_L > -3u_L$.

The question of how do these two possible ground state configurations look like, in terms of lattice distortions, can only be answered once we select a particular irrep of the little group at **L**. For all of these irrep, it is true that since **L** has an out-of-plane component, the lattice distortions need to have some inter-layer modulation: in particular, consecutive layers must have opposite distortions, because the out-of-plane component of **L** is exactly $\frac{1}{2}$. Out of all the irreps allowed, L_2^- is particularly interesting since it causes the same kind of in-plane distortions as M_1^+, but has this inter-layer modulation imposed. We show the single-L phase in Figure 3.9 and the triple-L in Figure 3.10a. The single-L configuration breaks the space group to $Immm$ (No. 71) and doubles the unit cell in one direction, while the triple-L preserves the space group $P6/mmm$ while doubling the unit cell along every primitive direction 2x2x2. The latter is shown in Figure 3.10a, and it corresponds to an alternating Tri-Hexagonal and Star-of-David configuration.

ML coupling Let us study the case of a system allowing two order parameters M and L, the former transforming like M_1^+ and the latter transforming one of the **L** little group irreps. The combination of their components which are allowed by symmetry to enter the free energy, would be

$$\begin{aligned}\mathcal{F}_{ML} = & \frac{\gamma_{ML}}{3}(M_1L_2L_3 \pm L_1M_2L_3 + L_1L_2M_3) \\ & + \frac{\lambda_{ML}^{(1)}}{4}(M_1M_2L_1L_2 \pm M_1M_3L_1L_3 + M_2M_3L_2L_3) \\ & + \frac{\lambda_{ML}^{(2)}}{4}(M_1^2L_1^2 + M_2^2L_2^2 + M_3^2L_3^2) + \frac{\lambda_{ML}^{(3)}}{4}M^2L^2\,,\end{aligned} \tag{3.15}$$

where the two $\pm$ sign choices are $+$ for the cases in which L transforms as $L_{1,2}^{\pm}$ and $-$ for the $L_{3,4}^{\pm}$ cases. Because of what we mentioned at the end of the last paragraph, we will focus on the case of the L_2^- irrep. The total free energy for the coupled system would be $\mathcal{F} = \mathcal{F}_M + \mathcal{F}_L + \mathcal{F}_{ML}$, which contains many terms with competing effects and is complicated enough that doing an analytical minimization is not achievable. For an in-depth discussion on the numerical minimization of this free energy, we refer to [41], while here we limit ourselves to a discussion on some of the possible (not all) coupled ground states that are possible when the M order has already set in.

Assuming that the system finds itself deep in the (M, M, M) phase and that $T_L << T_{3M}$, we can write an effective Landau free energy for the (L_1, L_2, L_3) order parameter

Eigenvalue	Eigenvector
$\tilde{\alpha}_L + c$	(1,1,1)
$\tilde{\alpha}_L - c/2$	(-1,1,0)
	(-1,-1,2)

(a) Starting from 3M

Eigenvalue	Eigenvector
$\tilde{\alpha}_L + c/2$	(0,1,1)
$\tilde{\alpha}_L - c/2$	(0,-1,1)
$\tilde{\alpha}_L + b$	(1,0,0)

(b) Starting from 1M

Table 3.1: (a) Eigenvalues and eigenvectors of the matrix in equation 3.17. (b) Eigenvalues and eigenvectors of the matrix in equation 3.19.

around $T \sim T_L$

$$\begin{aligned}\tilde{\mathcal{F}}_L =& C + \frac{\tilde{\alpha}_L}{2}L^2 + \frac{c}{2}(L_1L_2 + L_2L_3 + L_1L_3) \\ &+ \frac{\tilde{u}_L}{4}L^4 + \frac{\tilde{\lambda}_L}{4}(L_1^2L_2^2 + L_1^2L_3^2 + L_2^2L_3^2)\,,\end{aligned} \tag{3.16}$$

where now we need to be careful about the renormalized (tilde) parameters: they are not just combinations of the ones found in eq. 3.15, since in this case we are far away from T_M. The quadratic part of this free energy can be written as the product

$$\frac{1}{2}\begin{pmatrix}L_1 & L_2 & L_3\end{pmatrix}\begin{pmatrix}\tilde{\alpha}_L & c/2 & c/2 \\ c/2 & \tilde{\alpha}_L & c/2 \\ c/2 & c/2 & \tilde{\alpha}_L\end{pmatrix}\begin{pmatrix}L_1 \\ L_2 \\ L_3\end{pmatrix}\,, \tag{3.17}$$

so that diagonalizing the matrix we get three eigenvectors, which parameterize the leading instabilities, and some eigenvalues, which indicate the their corresponding critical temperatures. We report these in table 3.1a, where we can see that the value of c determines what instability is favored: for example if $c < 0$ than all components of L will condense with the same magnitude and we get to a total ordered phase $(M, M, M) + (L, L, L)$, which in terms of lattice distortions corresponds to a *Superimposed Tri-Hexagonal + Star-of-David*, represented in Figure 3.10b. This configuration doubles the unit cell in every direction (2x2x2) but preserves the space group $P6/mmm$.

If instead we assume that the system found itself in a stripe phase e.g., $(M, 0, 0)$, and $T_L << T_M$, the effective free energy would be

$$\begin{aligned}\tilde{\mathcal{F}}_L =& C + \frac{\tilde{\alpha}_L}{2}L^2 + \frac{c}{2}L_2L_3 + \frac{b}{2}L_1^2 \\ &+ \frac{\tilde{u}_L}{4}L^4 + \frac{\tilde{\lambda}_L}{4}(L_1^2L_2^2 + L_1^2L_3^2 + L_2^2L_3^2)\,,\end{aligned} \tag{3.18}$$

so that using the same trick as before, we can rewrite the bilinear part of the free energy as

$$\frac{1}{2}\begin{pmatrix}L_1 & L_2 & L_3\end{pmatrix}\begin{pmatrix}\tilde{\alpha}_L + b & 0 & 0 \\ 0 & \tilde{\alpha}_L & c/2 \\ 0 & c/2 & \tilde{\alpha}_L\end{pmatrix}\begin{pmatrix}L_1 \\ L_2 \\ L_3\end{pmatrix}\,, \tag{3.19}$$

where the eigenvectors and eigenvalues of this matrix are reported in table 3.1b. In this case there are three leading instabilities, for example if $c < 0$ and $c < 2b$ we would obtain an instability towards a total ordered phase $(M, 0, 0) + (0, L, L)$, which is called the *Staggered Tri-Hexagonal*, represented in Figure 3.10c in terms of lattice distortions[3]. These configurations double the unit cell in every direction (2x2x2) and break the space group to $Fmmm$ (No. 69).

[3]If instead, we started from a $(-M, 0, 0)$ we could have also have obtained an instability towards $(-M, 0, 0) + (0, L, L)$, called *Staggered Star-of-David*.

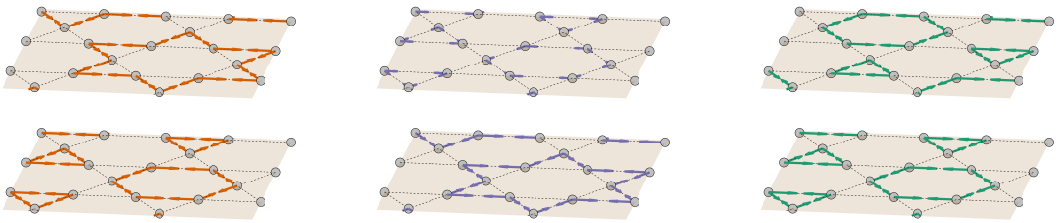

(a) (L, L, L) (b) $(M, M, M) + (L, L, L)$ (c) $(M, 0, 0) + (0, L, L)$

Figure 3.10: Lattice distortions corresponding to some of the other phases discussed in the last two paragraphs. (a) A configuration where only the L order has condensed and all its components have the same magnitude. It corresponds to alternating Tri-Hexagonal and Star-of-David configurations on each layer. (b) A configuration where both M and L have condensed with different relative magnitudes. There are again alternating Tri-Hexagonal and Star of David configurations on each layer, but with different distortion amplitudes. (c) A configuration where both M and L have condensed with equal relative magnitude. This configuration corresponds to a staggered Tri-Hexagonal configuration on each layer.

A order parameter and MLA coupling For what concerns the **A** point, there is only one vector in its star, which means that its little group is the same as the point group for the system D_{6h}, that allows for four 1D even irreps, four 1D odd irreps, two 2D even and two 2D odd irreps. An order parameter A transforming like one of these irreps gives the same free energy expansion

$$\mathcal{F}_A = \frac{\alpha_A}{2} A^2 + \frac{u_A}{4} A^4 \,, \tag{3.20}$$

where in the 1D cases A is just a scalar, while in the 2D case it has two components $A = (A_1, A_2)$ and $A^2 = A_1^2 + A_2^2$, $A^4 = (A^2)^2$.

It is possible to find trilinear combinations of order parameters M, L and A, respectively transforming like M_1^+, $L_j^\pm$ and $A_j^\pm$ with $j = 1, 2, 3, 4$ [4], that are invariant and are thus allowed to enter the free energy. In that case, the contributions to the free energy are

$$\begin{aligned}
\mathcal{F}_{MA} &= \frac{\lambda_{MA}}{4} M^2 A^2 \\
\mathcal{F}_{LA} &= \frac{\lambda^{(1)}_{LA}}{4} L^2 A^2 + \frac{\lambda^{(2)}_{LA}}{4} L_1 L_2 L_3 A \\
\mathcal{F}_{MLA} &= \frac{\gamma_{MLA}}{3} (M_1 L_1 + M_2 L_2 + M_3 L_3) A \\
&\quad + \frac{\lambda_{MLA}}{4} (M_1 M_2 L_3 + M_1 L_2 M_3 + L_1 M_2 M_3) A \,.
\end{aligned} \tag{3.21}$$

It is interesting to note that, in case we were to choose M_1^+, L_2^- and A_2^-, although the free energy would allow such coupling, the dynamical matrix would not contain any block that transforms like A_2^-, once brought to block diagonal form. This is because we are asking to find a set of displacements that changes sign when moving from one layer to another (modulated by the **A** vector), but that is also odd under inversion and under the horizontal mirror, and one can easily convince themselves this is impossible.

[4] For simplicity we will only look at the case where A transforms like one of the 1D irreps, although there could even be invariant MLA combinations in the case where A is two dimensional.

3D - $R\bar{3}m$ space group

Another interesting way to stack kagome layers in three dimensions, is to repeat the layers in the direction

$$\mathbf{d} = -\frac{1}{3}\mathbf{t}_1 + \frac{1}{3}\mathbf{t}_2 + \frac{1}{3}\mathbf{t}_3\,, \tag{3.22}$$

not perpendicular to the kagome plane, having used the vectors defined in 3.9. This is how the kagome layers are stacked in the Shandite structure. Using this vector, we can define $\{\mathbf{t}_1, \mathbf{t}_2, \mathbf{d}\}$ as a *primitive hexagonal* basis for the lattice, such that in cartesian coordinates we will find one layer at $z = 0$, the next at $z = c/3$, the next at $z = 2c/3$ and so on. We could still use $\{\mathbf{t}_1, \mathbf{t}_2, \mathbf{t}_3\}$ as a basis, but then the unit cell defined this way (often called *conventional*) would contain three kagome layers.

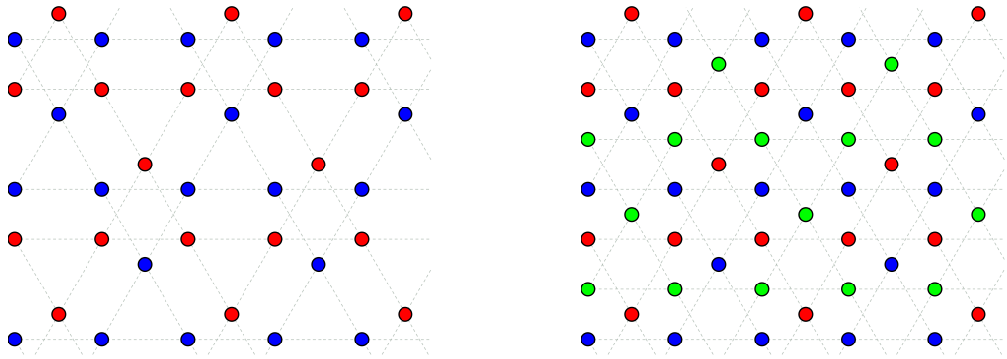

(a) Two consecutive layers.

(b) Three consecutive layers.

Figure 3.11: (a) Two consecutive layers of kagome lattices, stacked along the $\mathbf{d}$ direction: only some of the corner-sharing triangles are staggered with their counterpart on the next layer. (b) Three consecutive layers of kagome lattices, stacked along the $\mathbf{d}$ direction: all triangles are staggered with one from another layer. **Notice** that the colors now represent atoms belonging to different layers and not the sub-lattice specie.

This shifted stacking is not as random as it could look by just staring at the equation for $\mathbf{d}$. As shown in Figure 3.11a, where atoms belonging to different consecutive layers are colored in red and blue, the particular in-plane shift given by $-\frac{1}{3}\mathbf{t}_1 + \frac{1}{3}\mathbf{t}_2$ is such that some of the corner-sharing triangles between consecutive layers are *staggered*[5] with each other, when viewed from the top. If we add a third layer, colored in green in Figure 3.11b, we get that now all triangles are staggered with another one coming from a layer either above or below.

The space group for this configuration is $R\bar{3}m$ (No. 166), where the R signifies a trigonal crystal system that allows for a rhombohedral unit cell and $.\bar{3}m$ denotes the point group, D_{3d} in the Schoenflies notation. Let us address these two things separately.

- First, for a rhombohedral trigonal system, it is always possible to define both a hexagonal primitive cell (we did it above using $\{\mathbf{t}_1, \mathbf{t}_2, \mathbf{d}\}$) and a rhombohedral primitive cell, with primitive translation vectors $\{\mathbf{t}_{R1}, \mathbf{t}_{R2}, \mathbf{t}_{R3}\}$, such that $|\mathbf{t}_{R1}| = |\mathbf{t}_{R2}| = |\mathbf{t}_{R3}|$ and the angles between them are[6] $\alpha = \beta = \gamma < 90°$. In terms of the conventional

[5] We use the term staggered, since the superimposed triangles are reminding of the staggered ethane molecule, which has exactly the same point group D_{3d} as this system.

[6] Here we are assuming that $c > \sqrt{3/2}a$, i.e., the inter-layer distance is quite larger than the in-plane lattice parameter. It can be shown that this condition is equivalent to having $\alpha < 90°$, and in reciprocal

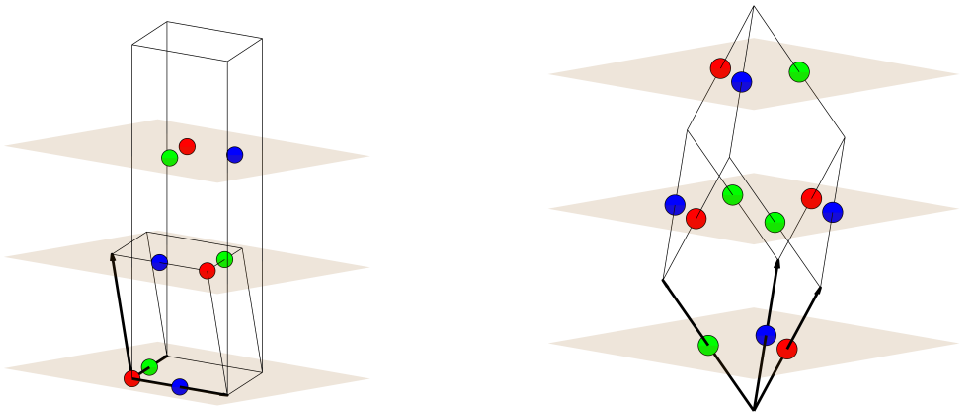

(a) (b)

Figure 3.12: The different unit cells for the $R\bar{3}m$ stacked kagome lattice, with the three repeating staggered layers. (a) The conventional (non-primitive) unit cell and the primitive hexagonal unit cell, with the $\{\mathbf{t}_1, \mathbf{t}_2, \mathbf{d}\}$ vectors indicated with solid black arrows. (b) The rhombohedral unit cell, with the primitive vectors $\{\mathbf{t}_{R1}, \mathbf{t}_{R2}, \mathbf{t}_{R3}\}$ highlighted as solid black arrows. **Notice** that in both these figures the colors represent again the sub-lattice specie and not the different layers.

lattice parameters used before, they can be written as

$$\mathbf{t}_{R1} = \frac{1}{3}\begin{pmatrix} 0 \\ \sqrt{3}a \\ c \end{pmatrix}, \qquad \mathbf{t}_{R2} = \frac{1}{6}\begin{pmatrix} 3a \\ -\sqrt{3}a \\ 2c \end{pmatrix}, \qquad \mathbf{t}_{R3} = \frac{1}{6}\begin{pmatrix} -3a \\ \sqrt{3}a \\ 2c \end{pmatrix}. \tag{3.23}$$

For computational purposes, it is better to use the rhombohedral unit cell, since it is smaller. In this unit cell, the three kagome sites are sitting at $\mathbf{t}_{R1}/2$, $\mathbf{t}_{R2}/2$ and $\mathbf{t}_{R3}/2$ and the angle determines the inter-layer distance, such that in the limit where $\alpha \to 0$ the layers are infinitely far away from each other.

- Second, the point group D_{3d} does not have a 6-fold rotational symmetry element, but it does have a so called S_6 symmetry element, which is a 6-fold rotation followed by a mirror perpendicular to the rotation axis. For example, in Figure 3.11a, a 60° rotation with respect to the center of one of the triangles would exchange red and blue, which corresponds to the mirror operation.

In Figure 3.13 we show the Brillouin Zone for this space group, where the reciprocal primitive vectors $\{\mathbf{g}_1, \mathbf{g}_2, \mathbf{g}_3\}$ are defined starting from $\{\mathbf{t}_{R1}, \mathbf{t}_{R2}, \mathbf{t}_{R3}\}$ with the usual construction,

$$\mathbf{g}_1 = \frac{2\pi}{V}\mathbf{t}_{R2} \times \mathbf{t}_{R3}\,, \qquad \mathbf{g}_2 = \frac{2\pi}{V}\mathbf{t}_{R3} \times \mathbf{t}_{R1}\,, \qquad \mathbf{g}_3 = \frac{2\pi}{V}\mathbf{t}_{R1} \times \mathbf{t}_{R2}\,, \tag{3.24}$$

where the volume of the unit cell is $V = \mathbf{t}_{R1} \cdot (\mathbf{t}_{R2} \times \mathbf{t}_{R3})$. The shape of this BZ is not really intuitive to grasp at first glance, so we also provide a 2D view of the external surface of the BZ in Figure 3.14, which makes it easier to visualize what the high-symmetry k-points are and the similarities between this BZ and the $P6/mmm$ one. First of all, we can see that the surface is made of two regular hexagons, top and bottom, similarly to the $P6/mmm$ BZ, but the surface that is wrapping around the sides, in this case, is made of couples

space it gives rise to the BZ in Figure 3.13, sometimes called RHL1. If the opposite was true, $c < \sqrt{3/2}a$, we would find $\alpha > 90°$ and a different BZ called RHL2. For more details we refer to the BZ database on the Bilbao Crystallographic Server [20] or Setyawan and Curtarolo [55].

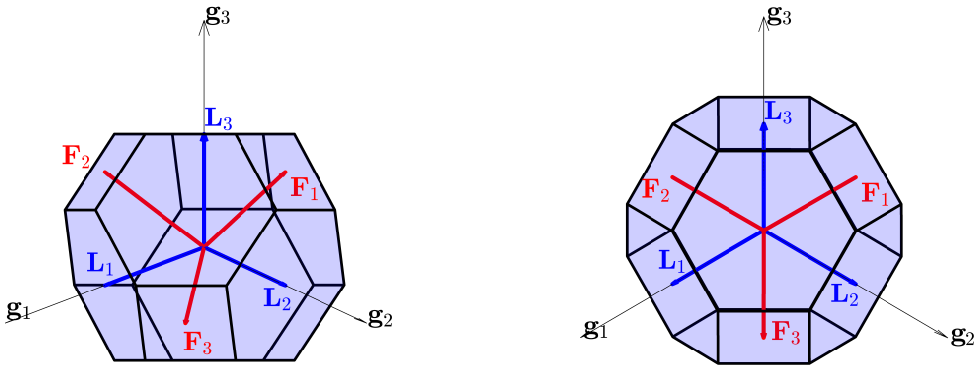

Figure 3.13: Two views of the three-dimensional $R\bar{3}m$ BZ, with the three **M** vectors represented as red arrows and the three **L** vectors as blue arrows.

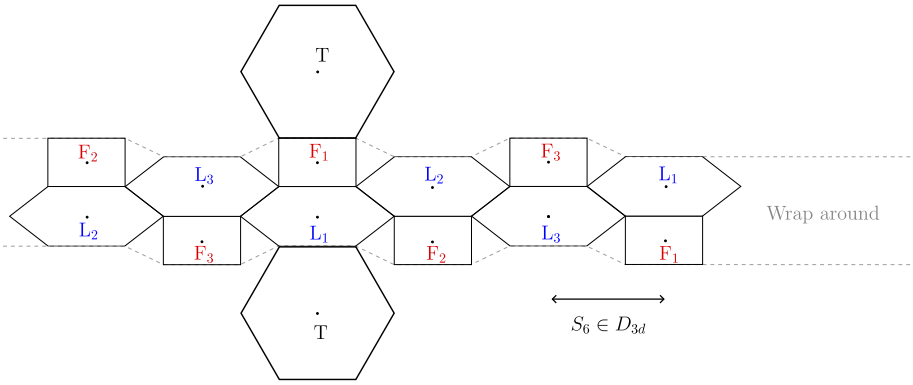

Figure 3.14: The external surface of the $R\bar{3}m$ BZ, with the relevant high-symmetry k-points reported with different colors. notice how the alternating structure of rectangles and hexagons reflects the S_6 symmetry element of the point group.

of alternating rectangles and hexagons. The fact that they are alternating reflects the S_6 symmetry element. At the center of the regular hexagons is the **T** point, which is akin to the **A** point in $P6/mmm$, at the center of the rectangles are the **F** points, the analogues of the **M** points and at the center of the non-regular hexagons are the **L** points. In terms of the reciprocal primitive vectors, these high-symmetry points are

$$\begin{gathered}\mathbf{F}_1 = \frac{1}{2}\mathbf{g}_2 + \frac{1}{2}\mathbf{g}_3\,, \qquad \mathbf{F}_2 = \frac{1}{2}\mathbf{g}_1 + \frac{1}{2}\mathbf{g}_3\,, \qquad \mathbf{F}_3 = \frac{1}{2}\mathbf{g}_1 + \frac{1}{2}\mathbf{g}_2\,, \\ \mathbf{L}_1 = \frac{1}{2}\mathbf{g}_1\,, \qquad \mathbf{L}_2 = \frac{1}{2}\mathbf{g}_2\,, \qquad \mathbf{L}_3 = \frac{1}{2}\mathbf{g}_3\,, \\ \mathbf{A} = \frac{1}{2}\mathbf{g}_1 + \frac{1}{2}\mathbf{g}_2 + \frac{1}{2}\mathbf{g}_3\,.\end{gathered} \tag{3.25}$$

F order parameter As described above, the **F** point has three vectors in its star. Moreover, the little group at **F** is C_{2h}, which has two 1D even irreps and two 1D odd irreps (see the character table 3.3 at the end of the chapter). Of these four, only the trivial one F_1^+, allows for an invariant trilinear combination, i.e., given an order parameter $F = (F_1, F_2, F_3)$ that transforms like F_1^+, the free energy expansion up to fourth order is

$$\mathcal{F}_F = \frac{\alpha_F}{2}F^2 + \frac{\gamma_F}{3}F_1F_2F_3 + \frac{u_F}{4}F^4 + \frac{\lambda_F}{4}(F_1^2F_2^2 + F_2^2F_3^2 + F_1^2F_3^2)\,. \tag{3.26}$$

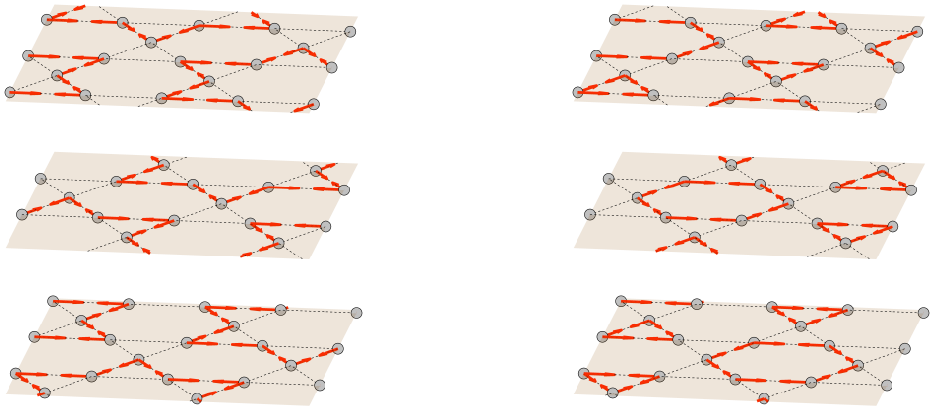

(a) (F, F, F) (b) $(F, F, -F)$

Figure 3.15: Lattice distortions corresponding to (a) Star-of-David configuration, (b) Tri-Hexagonal configuration. Both are shown on three consecutive kagome layers arranged as in the $R\bar{3}m$ shandite structure. Even though the layers are shifted, the same configuration is repeating on each layer.

This free energy looks exactly the same as the one for M_1^+ in the last section, equation 3.12, which means that also in this case the condensation of all three components is always favored. Moreover, it turns out that the lattice distortions that transform like F_1^+ also look the same as in Figure 3.7, so that the whole phenomenology described in the last Chapter still holds in the $R\bar{3}m$ case, even though the layers are slightly shifted. A stripe phase with just one component condensing, would double the unit cell in one direction and break the space group to $P2/m$ (No. 10). Because of the trilinear term, the two favored phases would be the Tri-Hexagonal and the Star-of-David configurations, repeating in every layer, which would double the unit cell in every direction but preserve the space group $R\bar{3}m$. These are shown in Figure 3.15. This result is kind of surprising since, as we mentioned in the introduction, no lattice-unstable $R\bar{3}m$ (shandite) kagome material has been found yet.

L order parameter and FL coupling The **L** point has three vectors in its star too, and their little group is C_{2h}. For an order parameter transforming like any irrep of the little group, the free energy expansion up to fourth order is

$$\mathcal{F}_L = \frac{\alpha_L}{2} L^2 + \frac{u_L}{4} L^4 + \frac{\lambda_L}{4} (L_1^2 L_2^2 + L_1^2 L_3^2 + L_2^2 L_3^2)\,. \tag{3.27}$$

In the last section, for the $P6/mmm$ space group we found that it was the L_2^- irrep that gave rise to the same kind of distortions as M_1^+, but with a π modulation on successive layers. The situation here is identical: in terms of lattice distortions, the L_2^- irrep gives rise to the same kind of in-plane configuration as F_1^+, but the sign is changing on every layer. For this reason the three components of L_2^- are as well described by Figure 3.9. In Figure 3.16a we show the lattice distortions caused by condensation of all components of the L order parameter in the shandite kagome-layered structure, which is the favored configuration for $\lambda_L < 0$.

Likewise, if the system has both order parameters F_1^+ and L_2^-, their coupling in the

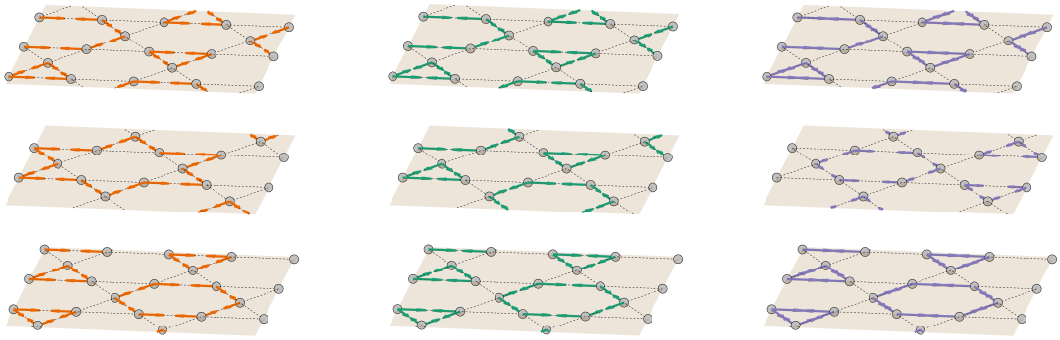

(a) (L, L, L) (b) $(F, 0, 0) + (0, L, L)$ (c) $(F, F, F) + (F, L, L)$

Figure 3.16: Lattice distortions corresponding to some configurations discussed in this section, shown on three consecutive kagome layers arranged as in the $R\bar{3}m$ shandite structure. (a) A configuration where only the L order has condensed and all its components have the same magnitude. It corresponds to alternating Tri-Hexagonal and Star-of-David configurations on each layer. (b) A configuration where both F and L have condensed with different relative magnitudes. There are again alternating Tri-Hexagonal and Star of David configurations on each layer, but with different distortion amplitudes. (c) A configuration where both F and L have condensed with equal relative magnitude. This configuration corresponds to a staggered Tri-Hexagonal configuration on each layer.

free energy would be

$$\begin{aligned}\mathcal{F}_{FL} = &\frac{\gamma_{FL}}{3}(F_1L_2L_3 + L_1F_2L_3 + L_1L_2F_3)\\ &+ \frac{\lambda^{(1)}_{FL}}{4}(F_1F_2L_1L_2 + F_1F_3L_1L_3 + F_2F_3L_2L_3)\\ &+ \frac{\lambda^{(2)}_{FL}}{4}(F_1^2L_1^2 + F_2^2L_2^2 + F_3^2L_3^2) + \frac{\lambda^{(3)}_{FL}}{4}F^2L^2\,,\end{aligned} \tag{3.28}$$

which looks identical to the $P6/mmm$ case and contains the trilinear terms. Following the discussion of the previous section, we could have many kinds of different coupled orders like $(F, F, F) + (L, L, L)$, shown in Figure 3.16c which would double the unit cell in every direction but keep the $R\bar{3}m$ space group, or $(F, 0, 0) + (0, L, L)$, shown in Figure 3.16b which would both double the unit cell and break the space group to $C2/m$ (No. 12).

T order parameter and FLT coupling Again, the discussion for a **T** order parameter is the same as for the **A** order in $P6/mmm$. There is only one vector in the star and the little group is D_{3d}, the same as the point group. If we pick F_1^+ and L_2^-, then the only **T** irrep that can couple to them is T_2^-,

$$\begin{aligned}\mathcal{F}_T &= \frac{\alpha_T}{2}T^2 + \frac{u_T}{4}T^4\,,\\ \mathcal{F}_{MT} &= \frac{\lambda_{MT}}{4}M^2T^2\,,\\ \mathcal{F}_{LT} &= \frac{\lambda^{(1)}_{LT}}{4}L^2T^2 + \frac{\lambda^{(2)}_{LT}}{4}L_1L_2L_3T\,,\\ \mathcal{F}_{MLT} &= \frac{\gamma_{MLT}}{3}(M_1L_1 + M_2L_2 + M_3L_3)T\,,\\ &\quad + \frac{\lambda_{MLT}}{4}(M_1M_2L_3 + M_1L_2M_3 + L_1M_2M_3)T\,.\end{aligned} \tag{3.29}$$

Even in this case, symmetry does not allow for any distortion of the atoms forming the kagome layer, i.e., the dynamical matrix does not contain any T_2^- block once diagonalized.

Conclusions Despite our efforts to identify notable distinctions in the symmetry properties of the permissible distortions between the **M** point in $P6/mmm$ and the **F** point in $R\bar{3}m$, our investigation found no significant differences. This is a interesting property of the two space groups and raises questions on the role these symmetries in the CDW formation in AV_3Sb_5, especially in light of the fact that (to the extent of our knowledge) there is no $R\bar{3}m$ kagome crystal that has a **F** driven lattice instability, similar to the **M** modulated lattice instability in $P6/mmm$ kagome metals. To gain more insight on the problem, we turn to first-principles calculations, for which we introduce the theory in the next chapter.

Character tables

The character table of a discrete group describes how the irreps behave under different group operations divided in so-called conjugacy classes. The trivial irrep A_{1g} is always the first row, and from the characters we can see that something that transform like A_{1g} is invariant under every operation of the point group. For D_{2h}, something that transforms like B_{1g} changes sign under the mirrors, and so on. We present the character tables for D_{2h}, which we found to be the little group for the **M** and **L** points in the $P6/mmm$ space group, and C_{2h}, which we found to be the little group for the **F** and **L** points in the $R\bar{3}m$ space group. Naming conventions for the irreps follow the ones adopted by the Bilbao Crystallographic Server [20]. For more details about group theory and its applications to condensed matter physics we refer to Arovas' lecture notes [56].

Irrep labels			Conjugacy classes and characters							
L little group	M little group	D_{2h}	E	C_2	C_2'	C_2''	i	σ_h	σ_v	σ_d
L_1^+	M_1^+	A_{1g}	1	1	1	1	1	1	1	1
L_2^+	M_2^+	B_{1g}	1	1	-1	-1	1	1	-1	-1
L_3^+	M_3^+	B_{2g}	1	-1	1	-1	1	-1	1	-1
L_4^+	M_4^+	B_{3g}	1	-1	-1	1	1	-1	-1	1
L_1^-	M_1^-	A_{1u}	1	1	1	1	-1	-1	-1	-1
L_2^-	M_2^-	B_{1u}	1	1	-1	-1	-1	-1	1	1
L_3^-	M_3^-	B_{2u}	1	-1	1	-1	-1	1	-1	1
L_4^-	M_4^-	B_{3u}	1	-1	-1	1	-1	1	1	-1

Table 3.2: Character table for the point group D_{2h}, which we found to be the little group for the **M** and **L** points in the $P6/mmm$ space group. The first four conjugacy classes represent the identity, two-fold rotation and the two possible mirrors, respectively. The next four are the same as the first four but followed by the inversion operation.

Irrep labels			Conjugacy classes and characters			
L little group	F little group	C_{2h}	E	C_2	i	σ_h
L_1^+	F_1^+	A_g	1	1	1	1
L_2^+	F_2^+	B_g	1	-1	1	-1
L_1^-	F_1^-	A_u	1	1	-1	-1
L_2^-	F_2^-	B_u	1	-1	-1	1

Table 3.3: Character table for the point group C_{2h}, which we found to be the little group for the **F** and **L** points in the $R\bar{3}m$ space group. The conjugacy classes represent the identity, the two-fold rotation, the inversion and the horizontal mirror, respectively.

Chapter 4

Kohn-Sham DFT

In this Chapter, our focus will be on providing a foundational understanding of DFT, shedding light on its underlying approximations and limitations. Consequently, while many important topics related to techniques utilized in the next Chapter will be omitted, we acknowledge here their significance. For instance, we will not delve into the theory of pseudopotentials, which allows to only consider valence electrons while disregarding core electrons, nor will we explore the theory of Projector Augmented Waves, which separates the electron wavefunctions into two components: a smooth region farther from the core, necessitating fewer details for accurate description, and a region in proximity to the core, requiring more detailed information for capturing its behavior. To learn more about these two subjects and their relation with each other, we refer the reader to the review in reference [57].

Many-body Schrödinger equation

One of the principles of Quantum Mechanics is that any system can be completely described by a wavefunction Ψ depending on a certain set of variables, which we call quantum numbers, and form the basis of the Hilbert space. Since physics is a game of assumptions and approximations, and our goal is to study crystals, we will start with the assumption that in real space Ψ is only a function of the coordinates $\mathbf{r}_1, \mathbf{r}_2, ..., \mathbf{r}_N$ of N electrons and $\mathbf{R}_1, \mathbf{R}_2, ..., \mathbf{R}_M$ of M nuclei that make up the aforementioned matter. We call such function, a *many-body wavefunction*

$$\Psi = \Psi(\mathbf{r}_1, \mathbf{r}_2, ..., \mathbf{r}_N; \mathbf{R}_1, \mathbf{R}_2, ..., \mathbf{R}_M)\,. \tag{4.1}$$

Given our assumption, we can then consider the Coulomb interaction between electrons and nuclei as the only force in play in our system, such that we can write a *many-body Schrödinger equation*

$$\left[-\sum_i \frac{\nabla_i^2}{2} - \sum_I \frac{\nabla_I^2}{2M_I} + \frac{1}{2}\sum_{i\neq j} \frac{1}{|\mathbf{r}_i - \mathbf{r}_j|} + \frac{1}{2}\sum_{I\neq J} \frac{Z_I Z_J}{|\mathbf{R}_I - \mathbf{R}_J|} - \sum_{i,I} \frac{Z_I}{|\mathbf{r}_i - \mathbf{R}_I|} \right] \Psi = E_{\text{tot}}\Psi\,, \tag{4.2}$$

which includes, in order, the kinetic term for the electrons, the kinetic term for the nuclei, the Coulomb repulsion between electrons, the Coulomb repulsion between nuclei and the attraction between electrons and nuclei. We set $\hbar = 1$ and measure all energies in Hartree, defined as $\mathrm{H}a = \frac{e^2}{4\pi\epsilon_0 a_0^2} \simeq 27$ eV, all lengths in Bohr radii $a_0 \simeq 0.53$ Å and all masses in units of m_e, the mass of the electron.

This equation is too general and also too hard to solve even for simple systems, so we will now go down a cascade of approximations that will turn this single equation into a system of equations which describe more effectively solid state systems and can also be solved numerically on today's computers in reasonable time scales.

Clamped nuclei approximation

In a solid state system, we think of the nuclei as being fixed (clamped) in a crystal structure and not moving (at least not as fast as the electrons). This sounds too restrictive, but is actually just the first step of a process known as the *Born-Oppenheimer approximation*: we will focus for now only on the electrons, and only later we will worry about the fact that the nuclei can move too.

There are three consequences of considering the nuclei as not moving:

1. $\mathbf{R}_1, ..., \mathbf{R}_M$ are just fixed parameters inside Ψ and are not variables anymore;
2. the kinetic energy of the nuclei is zero ($M_I = \infty$);
3. the energy term corresponding to the nuclei Coulomb repulsion is just a constant.

Given (3), we can take this constant term on the RHS of eq. 4.2 and redefine the energy eigenvalue as

$$E = E_{tot} - \frac{1}{2} \sum_{I \neq J} \frac{Z_I Z_J}{|\mathbf{R}_I - \mathbf{R}_J|} \,. \tag{4.3}$$

Moreover, we can rewrite the energy term corresponding to the attraction between electrons and the nuclei as

$$-\sum_{i,I} \frac{Z_I}{|\mathbf{r}_i - \mathbf{R}_I|} = \sum_i V_n(\mathbf{r}_i) \,, \tag{4.4}$$

so we can now write a *many-electron Schrödinger equation*

$$\left[-\sum_i \frac{\nabla_i^2}{2} + \sum_i V_n(\mathbf{r}_i) + \frac{1}{2} \sum_{i \neq j} \frac{1}{|\mathbf{r}_i - \mathbf{r}_j|} \right] \Psi = E\Psi \,. \tag{4.5}$$

If it was just for the first two terms on the LHS, this would be just a sum of single-particle Hamiltonians $\hat{H}_0$. What makes it a many-body Hamiltonian is the third term, the electron-electron repulsion

$$\hat{H}(\mathbf{r}_1, ..., \mathbf{r}_N) = \sum_i \hat{H}_0(\mathbf{r}_i) + \frac{1}{2} \sum_{i \neq j} \frac{1}{|\mathbf{r}_i - \mathbf{r}_j|} \,. \tag{4.6}$$

Before going on, let us remark that the electron density can be written with the many-body wavefunction as

$$n(\mathbf{r}) = N \int d\mathbf{r}_2 \, ... \, d\mathbf{r}_N \Psi^*(\mathbf{r}, \mathbf{r}_2, ..., \mathbf{r}_N) \, \Psi(\mathbf{r}, \mathbf{r}_2, ..., \mathbf{r}_N) \tag{4.7}$$

Independent electrons approximation

Now we need a new approximation to solve eq. 4.5. If there was no electron-electron interaction, we would just have a gas of free electrons. In that case, we know that the solution would be (because of Pauli's exclusion principle) the anti-symmetrized product of the individual single-electron wavefunctions $\phi_i(\mathbf{r})$, which we can write as a *Slater determinant*

$$\Psi(\mathbf{r}_1, ..., \mathbf{r}_N) = \frac{1}{\sqrt{N!}} \begin{vmatrix} \phi_1(\mathbf{r}_1) & \cdots & \phi_1(\mathbf{r}_N) \\ \vdots & \ddots & \vdots \\ \phi_N(\mathbf{r}_1) & \cdots & \phi_N(\mathbf{r}_N) \end{vmatrix} \,, \tag{4.8}$$

where each $\phi_i(\mathbf{r})$ is an eigenvector of the single-electron Hamiltonian $\hat{H}_0$, with eigenvalue ε_i. That means we would have to solve N differential equations of the kind

$$\hat{H}_0(\mathbf{r})\phi_i(\mathbf{r}) = \left[-\frac{\nabla^2}{2} + V_n(\mathbf{r}) \right] \phi_i(\mathbf{r}) = \varepsilon_i \phi_i(\mathbf{r}) \tag{4.9}$$

Notice that the density of electrons in this case would just be

$$n(\mathbf{r}) = \sum_i |\phi_i(\mathbf{r})|^2 \,. \tag{4.10}$$

Again, this approximation seems too drastic, so we will see how to make it better now.

Mean-field approximation

We would like to keep the single-electron description, but at the same time also introduce the Coulomb repulsion between them. Since we have the density of electrons $n(\mathbf{r})$ (i.e., a density of charge), we can exploit Poisson equation to introduce a classical electrostatic field generated by this density

$$\nabla^2 V_H(\mathbf{r}) = -4\pi\, n(\mathbf{r}) \qquad \rightarrow \qquad V_H(\mathbf{r}) = \int d\mathbf{r}' \frac{n(\mathbf{r}')}{|\mathbf{r}-\mathbf{r}'|} \,, \tag{4.11}$$

where we call V_H the Hartree potential for historical reasons. The idea is that, instead of describing the interaction of one electron with the others one by one, we can describe the interaction of one with the distribution (the *mean-field*) of all the others. Now we can insert this new potential V_H inside eq. 4.9, so that in total we would have to solve a system of N+1 differential equations

$$\left[-\frac{\nabla^2}{2} + V_n(\mathbf{r}) + V_H(\mathbf{r}) \right] \phi_i(\mathbf{r}) = \varepsilon_i\, \phi_i(\mathbf{r}) \,, \tag{4.12}$$

$$\nabla^2 V_H(\mathbf{r}) = -4\pi \sum_i |\phi_i(\mathbf{r})|^2 \,. \tag{4.13}$$

This system of equations is said to be *self-consistent*, which means that a set of solutions $\{\phi_i\}$ of eq. 4.12 must also be a solution of eq. 4.13. This also means that one can start with a guess of a solution and then solve iteratively towards a better solution.

Hartree-Fock approximation

The potential V_H that we added is a completely classical effect, but for our purposes we would like to account also for quantum effects. We said that if the electrons were to not interact at all, then the many-body wavefunction Ψ would look like eq. 4.8. Let us now imagine that they interact, but very lightly so we can use a *variational principle* as follows. We call E the expectation value of the Hamiltonian on the state Ψ,

$$E = \langle \Psi | \hat{H} | \Psi \rangle = \int d\mathbf{r}_1 ... d\mathbf{r}_N \Psi^* \hat{H}\, \Psi \,, \tag{4.14}$$

then we minimize this functional with respect to the single-electron functions $\phi_i(\mathbf{r})$ and impose their orthonormality

$$\frac{\delta E}{\delta \phi_i^*} = 0 \,, \tag{4.15}$$

$$\int d\mathbf{r}\, \phi_i^*(\mathbf{r}) \phi_j(\mathbf{r}) = \delta_{ij} \,. \tag{4.16}$$

This calculation is actually easier to do in second quantization so one does not have to deal with Slater determinants, but in the end it leads to the so called Hartree-Fock equations

$$\left[-\frac{\nabla^2}{2} + V_n(\mathbf{r}) + V_H(\mathbf{r}) \right] \phi_i(\mathbf{r}) + \int d\mathbf{r}'\, V_X(\mathbf{r}, \mathbf{r}')\, \phi_i(\mathbf{r}') = \varepsilon_i\, \phi_i(\mathbf{r}) \,, \tag{4.17}$$

$$\nabla^2 V_H(\mathbf{r}) = -4\pi \sum_i |\phi_i(\mathbf{r})|^2 \,, \tag{4.18}$$

which is a new set of self-consistent equations that now includes quantum effects (Pauli's exclusion principle), under the *non-local* potential $V_X(\mathbf{r}, \mathbf{r}')$, known as Fock exchange potential

$$V_X(\mathbf{r}, \mathbf{r}') = -\sum_j \frac{\phi_j^*(\mathbf{r}')\phi_j(\mathbf{r})}{|\mathbf{r} - \mathbf{r}'|} \,. \tag{4.19}$$

Kohn-Sham equations

The non-locality of $V_X(\mathbf{r}, \mathbf{r}')$ actually makes it harder to solve the set of equations 4.17, 4.18, so it is better to replace it with a simplified *local* version $V_x(\mathbf{r})$. We are also going to add a new effective potential $V_c(\mathbf{r})$ which accounts for the correlation between electrons, so in total we get

$$\left[-\frac{\nabla^2}{2} + V_n(\mathbf{r}) + V_H(\mathbf{r}) + V_x(\mathbf{r}) + V_c(\mathbf{r}) \right] \phi_i(\mathbf{r}) = \varepsilon_i \, \phi_i(\mathbf{r}) \,. \tag{4.20}$$

All these effective potentials V_H, V_x, V_c, are an approximation of the third term in eq. 4.2 and they stem from the fact that we decided to work with single-electron wavefunctions ϕ_i as if they were free and not interacting. We have not specified yet how the potentials V_x and V_c look like.

Hohenberg-Kohn theorem

We have seen in eq. 4.14 that the energy is in general a functional of the many-body wavefunction, $E = \mathcal{F}[\Psi(\mathbf{r}_1, ..., \mathbf{r}_N)]$, but if E is specifically the ground-state (GS) energy, then E is a functional of just the density $n(\mathbf{r})$,

$$E = F[n(\mathbf{r})] \,. \tag{4.21}$$

This is the statement of the Hohenberg-Kohn theorem, now we proceed to prove it.

As we said, the energy is a functional of the wavefunction Ψ. Moreover, the GS wavefunction is uniquely determined by the nuclear potential V_n. The one step we need to prove is that the GS density $n(\mathbf{r})$ uniquely determines the nuclear potential $V_n(\mathbf{r})$[1]:

$$n \overset{?}{\to} V_n \to \Psi \to E \,. \tag{4.22}$$

If that was not the case, then we could obtain the same GS density from two different nuclear potentials $V_n \neq V_n'$, so we will show that leads to a contradiction. Combining eq. 4.14 and eq. 4.5 we can write

$$\begin{aligned} E &= \langle \Psi | - \sum_i \frac{\nabla_i^2}{2} + \sum_i V_n(\mathbf{r}_i) + \frac{1}{2} \sum_{i \neq j} \frac{1}{|\mathbf{r}_i - \mathbf{r}_j|} | \Psi \rangle \\ &= \langle \Psi | \hat{T} + \sum_i V_n(\mathbf{r}_i) + \hat{W} | \Psi \rangle \\ &= \sum_i \int d\mathbf{r}_1 \, ... \, d\mathbf{r}_i \, ... \, d\mathbf{r}_N \Psi^*(\mathbf{r}_1, ..., \mathbf{r}_N) \, \Psi(\mathbf{r}_1, ..., \mathbf{r}_N) \, V_n(\mathbf{r}_i) + \langle \Psi | \hat{T} + \hat{W} | \Psi \rangle \,, \end{aligned} \tag{4.23}$$

[1] We defined it in eq. 4.4.

and now using the definition of the density in eq. 4.7

$$\begin{aligned} E &= \sum_{i=1}^{N} \frac{1}{N} \int d\mathbf{r}_i \, n(\mathbf{r}_i) \, V_n(\mathbf{r}_i) + \langle \Psi | \hat{T} + \hat{W} | \Psi \rangle \\ &= \int d\mathbf{r} \, n(\mathbf{r}) \, V_n(\mathbf{r}) + \langle \Psi | \hat{T} + \hat{W} | \Psi \rangle \, . \end{aligned} \tag{4.24}$$

Let us assume that Ψ is the GS wavefunction for the nuclear potential V_n with GS energy E and density $n(\mathbf{r})$. If we were to substitute V_n' for V_n we would get a new Hamiltonian $\hat{H}'$ for which Ψ is not the GS anymore

$$\langle \Psi | \hat{H}' | \Psi \rangle = \langle \Psi | \hat{T} + \sum_i V_n'(\mathbf{r}_i) + \hat{W} | \Psi \rangle > E' \, , \tag{4.25}$$

where E' is the GS energy of $\hat{H}'$. In the same way as we did before, we can rewrite this inequality as

$$\int d\mathbf{r} \, n(\mathbf{r}) \, V_n'(\mathbf{r}) + \langle \Psi | \hat{T} + \hat{W} | \Psi \rangle > E' \, , \tag{4.26}$$

so that combining with eq. 4.24 we find

$$E - E' > \int d\mathbf{r} \, n(\mathbf{r}) \left[V_n(\mathbf{r}) - V_n'(\mathbf{r}) \right] . \tag{4.27}$$

Since we did not make any assumption on the shapes of V_n and V_n', we could just redo this whole calculation exchanging the primed and unprimed variables, so that we could get

$$E' - E > \int d\mathbf{r} \, n(\mathbf{r}) \left[V_n'(\mathbf{r}) - V_n(\mathbf{r}) \right] . \tag{4.28}$$

The last two equations contradict each other, therefore two different nuclear potentials cannot lead to the same density and the theorem is proved.

Hohenberg-Kohn variational principle

Hohenberg-Kohn theorem says that the GS energy is a functional of the density, but it does not say how to find this functional. From 4.24 and using eq. 4.20 (multiply by ϕ_i^* on the left, integrate and sum over i) we find

$$\begin{aligned} E = F[n] &= \int d\mathbf{r} \, n(\mathbf{r}) \, V_n(\mathbf{r}) + \langle \Psi[n] | \hat{T} + \hat{W} | \Psi[n] \rangle \\ &= \underbrace{\int d\mathbf{r} \, n(\mathbf{r}) \, V_n(\mathbf{r}) - \sum_i \int d\mathbf{r} \, \phi_i^*(\mathbf{r}) \frac{\nabla^2}{2} \phi_i(\mathbf{r}) + \frac{1}{2} \int \int d\mathbf{r} \, d\mathbf{r}' \, \frac{n(\mathbf{r}) n(\mathbf{r}')}{|\mathbf{r} - \mathbf{r}'|}}_{Mean-field \; (Hartree) \; approximation} + E_{xc}[n] \, . \end{aligned} \tag{4.29}$$

The idea of Kohn and Sham was to split the functional into a sum of known contributions and the unknown one: the exchange and correlation energy. If we knew E_{xc} we could calculate the GS energy through the density $n(\mathbf{r})$. How do we determine the density?

Hohenberg-Kohn variational principle states that the GS density $n_0(\mathbf{r})$ is the one that minimizes the functional $F[n]$, that is

$$\left. \frac{\delta F}{\delta n(\mathbf{r})} \right|_{n=n_0} = 0 \, , \tag{4.30}$$

which makes sense, because minimizing F would mean obtaining the lowest energy. Using the chain rule, we can see that

$$\frac{\delta F}{\delta \phi_i^*} = \frac{\delta F}{\delta n} \frac{\delta n}{\delta \phi_i^*} = \frac{\delta F}{\delta n} \frac{\delta}{\delta \phi_i^*} \sum_j |\phi_j|^2 = \frac{\delta F}{\delta n} \sum_j \phi_j \delta_{ij} = \frac{\delta F}{\delta n} \phi_i \, , \tag{4.31}$$

so we might as well minimize F with respect to ϕ_i^*, since if eq. 4.30 holds, then it must also be that $\frac{\delta F}{\delta \phi_i^*} = 0$. Taking this functional derivative leads to a new set of self-consistent equations for the wavefunctions $\phi_i(\mathbf{r})$, known as the *Kohn-Sham equations*

$$\left[-\frac{\nabla^2}{2} + V_n(\mathbf{r}) + V_H(\mathbf{r}) + V_{xc}(\mathbf{r}) \right] \phi_i(\mathbf{r}) = \varepsilon_i \, \phi_i(\mathbf{r}) \,, \tag{4.32}$$

$$V_n(\mathbf{r}) = -\sum_I \frac{Z_I}{|\mathbf{R}_I - \mathbf{r}|} \,, \tag{4.33}$$

$$n(\mathbf{r}) = \sum_i |\phi_i(\mathbf{r})|^2 \,, \tag{4.34}$$

$$\nabla^2 V_H(\mathbf{r}) = -4\pi n(\mathbf{r}) \,, \tag{4.35}$$

$$V_{xc}(\mathbf{r}) = \left. \frac{\delta E_{xc}}{\delta n} \right|_{n(\mathbf{r})} \,, \tag{4.36}$$

with V_{xc} being called the exchange-correlation potential. There are several techniques to estimate the form of the functional E_{xc}, the two most common ones are the *local density approximation* (LDA) and the *generalized gradient approximation* (GGA).

Local density approximation

In order to understand the LDA, we first have to look at the free electron gas. We consider N electrons in a box of volume V, so we can solve all of the N single-electron Schrödinger equations in momentum space and find

$$\phi_{\mathbf{k}}(\mathbf{r}) = \frac{1}{\sqrt{V}} e^{i\mathbf{k}\cdot\mathbf{r}} \,, \qquad \varepsilon_{\mathbf{k}} = \frac{|\mathbf{k}|^2}{2} \,, \tag{4.37}$$

as the eigenstates and eigenvalues (in Hartree units) respectively. At zero temperature the states are all occupied up to the Fermi energy $\varepsilon_F = k_F^2/2$. The total number of electrons, is then related to the Fermi momentum k_F, since in momentum space the occupied states represent a sphere of radius k_F

$$\begin{aligned} N = \sum_i |\phi_i|^2 &\to \frac{V}{(2\pi)^3} 2 \int d^3\mathbf{k} \, \Theta(|\mathbf{k}| - k_F) \\ &= \frac{V}{(2\pi)^3} 2 \int_0^{2\pi} d\varphi \int_0^{\pi} d\theta \, \sin\theta \int_0^{k_F} dk \, k^2 = \frac{V k_F^3}{3\pi^2} \,, \end{aligned} \tag{4.38}$$

where the 2 comes from summing on the spins and Θ is the Heaviside step function. The fermi momentum is then related to the average electron density $\bar{n} = N/V$ by

$$k_F = (3\pi^2 \bar{n})^{1/3} \,. \tag{4.39}$$

Now we can turn on the electron-electron interactions and use the Hartree-Fock approximation. For the electron gas, the Fock exchange energy can be calculated exactly. By this we mean that if we look at the last term in the LHS of eq. 4.17, multiplying by $\phi_i^*(\mathbf{r})$, summing over i and integrating over $\mathbf{r}$ would lend us an energy (a scalar number) which we call E_X, and is given by

$$\begin{aligned} E_X &= -\sum_{i,j} \int_V d\mathbf{r} \int_V d\mathbf{r}' \, \frac{\phi_i^*(\mathbf{r}) \phi_i(\mathbf{r}') \phi_j^*(\mathbf{r}') \phi_j(\mathbf{r})}{|\mathbf{r} - \mathbf{r}'|} \\ &\to -\frac{1}{(2\pi)^6} \int d^3\mathbf{k} \, \Theta(|\mathbf{k}| - k_F) \int d^3\mathbf{k}' \, \Theta(|\mathbf{k}'| - k_F) \int_V d\mathbf{r} \int_V d\mathbf{r}' \, \frac{e^{-i(\mathbf{k}-\mathbf{k}')\cdot(\mathbf{r}-\mathbf{r}')}}{|\mathbf{r} - \mathbf{r}'|} \,. \end{aligned} \tag{4.40}$$

Now we can do a change of variables

$$\mathbf{u} = k_F(\mathbf{r} - \mathbf{r}')\,, \quad \mathbf{q} = \frac{\mathbf{k}}{k_F}\,, \quad \mathbf{q}' = \frac{\mathbf{k}'}{k_F}\,, \tag{4.41}$$

so the integral becomes

$$\begin{aligned} E_X &= -\frac{Vk_F^4}{(2\pi)^6} \overbrace{\int_{|\mathbf{q}|\leq 1} d^3\mathbf{q} \int_{|\mathbf{q}'|\leq 1} d^3\mathbf{q}' \, \frac{e^{-i(\mathbf{q}-\mathbf{q}')\cdot\mathbf{u}}}{|\mathbf{u}|}}^{16\pi^3} \\ &= -\frac{Vk_F^4}{4\pi^3} = -\frac{3V}{4}\left(\frac{3}{\pi}\right)^{1/3} \bar{n}^{4/3}\,. \end{aligned} \tag{4.42}$$

This is a function of the average electron density $\bar{n}$: that is why we call this model the *homogeneous electron gas* (HEG). Unfortunately, even for the electron gas, there is no analytical expression for the correlation energy E_C, but it has been possible to calculate it with numerical techniques like Monte Carlo and subsequently to parameterize it. This means that the form of the functional $E_{xc}^{HEG}[\bar{n}]$ is almost exactly known for the homogeneous electron gas.

In interacting systems, the density may not be similar at all to the one of the homogeneous electron gas. Nevertheless, if it is slowly varying, we can imagine that in every infinitesimal volume element $d^3\mathbf{r}$ we actually have the known HEG one evaluated at the local density $n(\mathbf{r})$

$$dE_{xc} = \frac{E_{xc}^{\mathrm{HEG}}[n(\mathbf{r})]}{V} d^3\mathbf{r}\,, \tag{4.43}$$

so that integrating over the volume lends us

$$E_{xc}^{LDA}[n(\mathbf{r})] = \int dE_{xc} = \int_V d^3\mathbf{r} \, \frac{E_{xc}^{\mathrm{HEG}}[n(\mathbf{r})]}{V}\,. \tag{4.44}$$

One can include some inhomogeneity by considering a functional of both the density and the density gradient, in what is known as the GGA approximation

$$E_{xc}^{GGA}[n(\mathbf{r})] = \int_V d^3\mathbf{r} \, \frac{E_{xc}^{\mathrm{HEG}}[n(\mathbf{r})] + H[n(\mathbf{r}), \nabla n(\mathbf{r})]}{V}\,. \tag{4.45}$$

The challenge lies in defining the specific form of the functional H within the GGA approximation. Different approaches have been used to determine H, such as incorporating empirical or fitted terms to match experimental or numerical results. The Perdew-Burke-Ernzerhof (PBE) functional [58] is the most widely used GGA approximation and it is the one that we will use in the next Chapter for our simulations. The PBE functional is constructed using only fundamental constants as parameters and is designed to match the local density approximation (LDA) in the limit of slowly varying density.

Details of an actual calculation

How do we start solving the set of self-consistent equations 4.32-4.36? If we have the nuclear coordinates we can calculate the nuclear potential 4.33 immediately (this is usually available from crystallographic data). To calculate the Hartree and exchange-correlation potentials 4.35-4.36 we need to start with a guess of what the electron density $n(\mathbf{r})$ looks like. This guess is usually made by adding up the densities of hydrogen-like orbitals arranged in the atomic positions of the material under study. With this first guess we obtain also an initial form of the potentials V_H and V_{xc}, so we can proceed to numerically solve eq. 4.32. The set of solutions ϕ_i that we get out of it, is used to calculate the

new density 4.34, from which we can get new potentials and so on, iteratively. We keep repeating this process until the difference between a measured quantity (e.g., the density itself or the energy or the potential) in two subsequent steps is small enough (smaller than a tolerance that we have to set), so we say that we have reached *self-consistency*.

Calculating band structures

In applying DFT to a solid, we can make use of the discrete translational invariance of its crystal structure. Said otherwise, we can use Bloch's theorem on the single particle wavefunctions to state they should have the form

$$\phi_{i\mathbf{k}}(\mathbf{r}) = e^{i\mathbf{k}\cdot\mathbf{r}} u_{i\mathbf{k}}(\mathbf{r})\,, \tag{4.46}$$

$$u_{i\mathbf{k}}(\mathbf{r}+\mathbf{T}) = u_{i\mathbf{k}}(\mathbf{r})\,, \qquad \mathbf{T} = n_1\mathbf{a}_1 + n_2\mathbf{a}_2 + n_3\mathbf{a}_3\,. \tag{4.47}$$

If we replace this expression for the wavefunction inside the Kohn-Sham equations 4.32, we get

$$\left[-\frac{\nabla^2}{2} + V_{tot}(\mathbf{r})\right] e^{i\mathbf{k}\cdot\mathbf{r}} u_{i\mathbf{k}}(\mathbf{r}) = \varepsilon_{i\mathbf{k}}\, e^{i\mathbf{k}\cdot\mathbf{r}} u_{i\mathbf{k}}(\mathbf{r})\,, \tag{4.48}$$

where we called $V_{tot} = V_n + V_H + V_{xc}$. The first term on the LHS becomes

$$\begin{aligned}
&-\frac{\nabla}{2}\cdot\left[(\nabla e^{i\mathbf{k}\cdot\mathbf{r}})u_{i\mathbf{k}}(\mathbf{r}) + e^{i\mathbf{k}\cdot\mathbf{r}}\nabla u_{i\mathbf{k}}(\mathbf{r})\right] \\
=&-\frac{\nabla}{2}\cdot\left[i\mathbf{k}\, e^{i\mathbf{k}\cdot\mathbf{r}} u_{i\mathbf{k}}(\mathbf{r}) + e^{i\mathbf{k}\cdot\mathbf{r}}\nabla u_{i\mathbf{k}}(\mathbf{r})\right] \\
=&\, e^{i\mathbf{k}\cdot\mathbf{r}}\frac{|\mathbf{k}|^2}{2} u_{i\mathbf{k}}(\mathbf{r}) - i\, e^{i\mathbf{k}\cdot\mathbf{r}}\mathbf{k}\cdot\nabla u_{i\mathbf{k}}(\mathbf{r}) - e^{i\mathbf{k}\cdot\mathbf{r}}\frac{1}{2}\nabla^2 u_{i\mathbf{k}}(\mathbf{r}) \\
=&-e^{i\mathbf{k}\cdot\mathbf{r}}\frac{1}{2}\left[\nabla^2 + 2i\mathbf{k}\cdot\mathbf{r} - |\mathbf{k}|^2\right] u_{i\mathbf{k}}(\mathbf{r}) \\
=&-e^{i\mathbf{k}\cdot\mathbf{r}}\frac{1}{2}(\nabla + i\mathbf{k})^2 u_{i\mathbf{k}}(\mathbf{r})\,,
\end{aligned} \tag{4.49}$$

so that we can get rid of the exponential factor on both sides and write an equation for just $u_{i\mathbf{k}}$

$$\left[-\frac{1}{2}(\nabla + i\mathbf{k})^2 + V_{tot}(\mathbf{r})\right] u_{i\mathbf{k}}(\mathbf{r}) = \varepsilon_{i\mathbf{k}}\, u_{i\mathbf{k}}(\mathbf{r})\,, \tag{4.50}$$

which we call the *crystal version* of the Kohn-Sham equations. We restrict the vector $\mathbf{k}$ to only live in the first Brillouin Zone (BZ). The density of electrons is then determined by integrating over the BZ and summing over all the occupied states

$$n(\mathbf{r}) = \sum_i \int_{\mathrm{BZ}} \frac{d^3\mathbf{k}}{\Omega_{\mathrm{BZ}}} f_{i\mathbf{k}} |u_{i\mathbf{k}}(\mathbf{r})|^2\,, \tag{4.51}$$

where $f_{i\mathbf{k}} = 1$ if the state is occupied by an electron and $f_{i\mathbf{k}} = 0$ otherwise, and the cell function is normalized such that (UC is the unit cell in real space)

$$\int_{UC} d^3\mathbf{r} |u_{i\mathbf{k}}(\mathbf{r})|^2 = 1\,. \tag{4.52}$$

Density Functional Perturbation Theory

In this section, we introduce the fundamental concepts of DFPT, a technique developed in the 1990s for calculating linear responses within first-principles methods [59, 60]. DFPT is now implemented in numerous DFT codes. Given our interest in lattice-related properties, we will specifically focus on the application of DFPT for computing phonon properties.

Born-Oppenheimer approximation

Throughout the last section we always assumed the nuclei to be fixed in their equilibrium position (what we called clamped nuclei approximation). As we said, that was the first step of what is known as *adiabatic* or *Born-Oppenheimer approximation*, in which we assume the nuclei to move way slower than the electrons, such that we can separate the total wavefunction of the system into an electron-only and a nuclei-only part

$$\Psi(\mathbf{r}_1, ..., \mathbf{r}_N; \mathbf{R}_1, ..., \mathbf{R}_M) = \Psi_{\mathbf{R}}(\mathbf{r}_1, ..., \mathbf{r}_N)\Phi(\mathbf{R}_1, ..., \mathbf{R}_M)\,. \tag{4.53}$$

The subscript in $\Psi_{\mathbf{R}}$ is now there to remind ourselves that the wavefunction depends parametrically on the positions of the nuclei and it is the solution of the many-electron Hamiltonian 4.5 (which we also rewrite now with explicitly indicating every quantity that depends parametrically on $\mathbf{R} = \{\mathbf{R}_1, ..., \mathbf{R}_M\}$)

$$\left[-\sum_i \frac{\nabla_i^2}{2} + \sum_i V_n(\mathbf{r}_i, \mathbf{R}) + \frac{1}{2}\sum_{i\neq j} \frac{1}{|\mathbf{r}_i - \mathbf{r}_j|} \right] \Psi_{\mathbf{R}} = E(\mathbf{R})\Psi_{\mathbf{R}}\,. \tag{4.54}$$

Remember that in eq. 4.3 we included in $E(\mathbf{R})$ also the nuclei-nuclei Coulomb repulsion. Now if $\Psi_{\mathbf{R}}$ is correctly normalized we can integrate it out of the full many-body Schrödinger equation, so that we get an effective one just for the nuclei

$$\left[-\sum_I \frac{\nabla_I^2}{2M_I} + E(\mathbf{R}) \right] \Phi(\mathbf{R}) = \mathcal{E}\Phi(\mathbf{R})\,. \tag{4.55}$$

The quantity $E(\mathbf{R})$ is known as the Born-Oppenheimer energy surface and it is the ground state energy of a system of interacting electrons moving in the field of fixed nuclei. One way to move forward would be of considering the nuclei as classical particles (since they move so slow compared to the electrons), such that they satisfy Newton's law and we can find their equilibrium positions by imposing

$$\mathbf{F}_I = -\frac{\partial E(\mathbf{R})}{\partial \mathbf{R}_I} = 0\,, \tag{4.56}$$

where $\mathbf{F}_I$ is the force acting on the Ith nucleus and in the *harmonic approximation* the vibrational frequencies ω are found by solving the secular equation

$$\det \left| \frac{1}{\sqrt{M_I M_J}} \frac{\partial^2 E(\mathbf{R})}{\partial \mathbf{R}_I \partial \mathbf{R}_J} - \omega^2 \right| = 0\,, \tag{4.57}$$

where the matrix being diagonalized here is known as the *dynamical matrix*.

We can take derivatives of $E(\mathbf{R})$ by using Hellmann-Feynman theorem:

$$\frac{\partial E_\lambda}{\partial \lambda} = \langle \psi_\lambda | \frac{\partial \hat{H}_\lambda}{\partial \lambda} | \psi_\lambda \rangle\,, \tag{4.58}$$

the first derivative of the eigenvalue E_λ of a parameter-dependent Hamiltonian $\hat{H}_\lambda$ is given by the expectation value of the first derivative of the Hamiltonian on the eigenstate ψ_λ corresponding to E_λ. In our case, this means that the force acting on the Ith nucleus can be calculated by taking a derivative of the many-electron Hamiltonian 4.54 (but also

remembering eq. 4.3)

$$\begin{aligned}
\mathbf{F}_I &= -\frac{\partial E(\mathbf{R})}{\partial \mathbf{R}_I} \\
&= -\langle \Psi_{\mathbf{R}} | \frac{\partial \hat{H}_{\mathbf{R}}}{\partial \mathbf{R}_I} | \Psi_{\mathbf{R}} \rangle - \frac{1}{2} \frac{\partial}{\partial \mathbf{R}_I} \sum_{J \neq I} \frac{Z_I Z_J}{|\mathbf{R}_J - \mathbf{R}_I|} \\
&= -\sum_i \int d\mathbf{r} d\mathbf{r}_2 ... d\mathbf{r}_N \Psi^*_{\mathbf{R}} \Psi_{\mathbf{R}} \frac{\partial V_n(\mathbf{r}_i, \mathbf{R})}{\partial \mathbf{R}_I} - Z_I \sum_{J \neq I} Z_J \frac{\mathbf{R}_J - \mathbf{R}_I}{|\mathbf{R}_J - \mathbf{R}_I|^3} \\
&= Z_I \int d\mathbf{r}\, n_{\mathbf{R}}(\mathbf{r}) \frac{\mathbf{r} - \mathbf{R}_I}{|\mathbf{r} - \mathbf{R}_I|^3} - Z_I \sum_{J \neq I} Z_J \frac{\mathbf{R}_J - \mathbf{R}_I}{|\mathbf{R}_J - \mathbf{R}_I|^3} \\
&= \int d\mathbf{r}\, n_{\mathbf{R}}(\mathbf{r}) \mathbf{f}^{(e)}_I(\mathbf{r}) - \mathbf{F}^{(n)}_I \,,
\end{aligned} \tag{4.59}$$

where we see that the force acting on a nucleus is the sum of two (classical) contributions: the electrostatic repulsion of the other nuclei around it $\mathbf{F}^{(n)}_I$ and the attraction of the electron charge density of all the electrons $\mathbf{f}^{(e)}_I(\mathbf{r})$. At last, the Hessian of the Born-Oppenheimer energy surface can be written as

$$\begin{aligned}
\frac{\partial^2 E(\mathbf{R})}{\partial \mathbf{R}_I \partial \mathbf{R}_J} &= -\frac{\partial \mathbf{F}_I}{\partial \mathbf{R}_J} \\
&= -\int d\mathbf{r}\, \frac{\partial n_{\mathbf{R}}(\mathbf{r})}{\partial \mathbf{R}_J} \mathbf{f}^{(e)}_I(\mathbf{r}) - \int d\mathbf{r}\, n_{\mathbf{R}}(\mathbf{r}) \frac{\partial \mathbf{f}^{(e)}_I(\mathbf{r})}{\partial \mathbf{R}_J} + \frac{\partial \mathbf{F}^{(n)}_I}{\partial \mathbf{R}_J} \,.
\end{aligned} \tag{4.60}$$

This last equation is pretty important, it states that the calculation of the Hessian requires to know the ground state electron charge density $n_{\mathbf{R}}$ AND its *linear response* to a distortion of the geometry of the nuclei $\partial n_{\mathbf{R}} / \partial \mathbf{R}_I$. In the last Chapter we learned a way (DFT) to give good approximations for the ground state electron density, but we still do not have a method to calculate linear responses.

Sternheimer equations

DFPT is one of the approaches developed to approximate the linear response of the density. The key concept is that, although we are mainly concerned with the linear response of the density, we can consider the linear responses of other quantities that depend on the nuclear positions $\mathbf{R}_I$. For example we can calculate the linear response of the total potential ΔV, as well as the KS wavefunctions $|\Delta\phi_i\rangle$ and eigenvalues $\Delta\varepsilon_i$. By treating ΔV as a small perturbation to the Schrödinger equation and approximating $|\Delta\phi_i\rangle$ and $\Delta\varepsilon_i$ at first order in perturbation theory, we obtain a new set of self-consistent equations known as the Sternheimer equations

$$\Big(H_{\mathbf{k}+\mathbf{q}} + \alpha \sum_{v'} |u_{v'\mathbf{k}+\mathbf{q}}\rangle\langle u_{v'\mathbf{k}+\mathbf{q}}| - \varepsilon_{v\mathbf{k}}\Big) |\Delta u_{v\mathbf{k}+\mathbf{q}}\rangle = -\Big(1 - \sum_{v'} |u_{v'\mathbf{k}+\mathbf{q}}\rangle\langle u_{v'\mathbf{k}+\mathbf{q}}|\Big) \Delta V_{\mathbf{q}} |u_{v\mathbf{k}}\rangle \,, \tag{4.61}$$

$$\Delta n_{\mathbf{q}}(\mathbf{r}) = 4 \sum_{v\mathbf{k}} u^*_{v\mathbf{k}}(\mathbf{r}) \Delta u_{v\mathbf{k}+\mathbf{q}}(\mathbf{r}) \,, \tag{4.62}$$

$$\Delta V_{\mathbf{q}}(\mathbf{r}) = \Delta V_{n,\mathbf{q}}(\mathbf{r}) + \int d\mathbf{r}' \frac{\Delta n_{\mathbf{q}}(\mathbf{r}')}{|\mathbf{r} - \mathbf{r}'|} e^{i\mathbf{q}\cdot(\mathbf{r}-\mathbf{r}')} + \left.\frac{dV_{xc}(n)}{dn}\right|_{n=n(\mathbf{r})} \Delta n_{\mathbf{q}}(\mathbf{r}) \,. \tag{4.63}$$

In Appendix A, a detailed explanation is provided for each quantity involved in these equations, along with the derivation process. Numerical solutions for these equations can be obtained using methods similar to those described earlier. In the upcoming Chapter, we will utilize Abinit's implementation of DFPT to compute the phonons of specific kagome-layered systems discussed in Chapter 2.

Chapter 5

DFT calculations

Kagome metal CsV_3Sb_5

Among the kagome metals, we focus on the CsV_3Sb_5 compound, which we simulate using DFT as implemented in Abinit 9.6.2 [61, 62] within the PBE GGA approximation and in a basis of Projector Augmented Waves (PAW) [63]. We use a Γ centered 16x16x8 k-point grid and a energy cutoff of 475 eV. For the electronic occupation (the $f_{i\mathbf{k}}$ in equation 4.51), we use a Gaussian smearing scheme[1] with smearing temperature of 10 meV.

First of all, we calculate the ground state properties for the experimental structure, with lattice parameters $a = 5.4949\,\text{Å}$ and $c = 9.3085\,\text{Å}$, and reduced out-of-plane coordinate of the Sb2 atoms $z = 0.74217$. Next, we interpolate the KS eigenvalues along a **k**-point path connecting high-symmetry points in the BZ. The resulting band structure is showed in Figure 5.1a, for a 2 eV window around the Fermi level, while the inset shows the BZ and the **k**-path. At the **M** point, there are four different saddle points close to the Fermi level. For each of them, we indicate the irrep that the corresponding Bloch wavefunction transforms under, which is obtained by applying point group transformations, calculating the character and comparing it to the character table of the little group at **M**, D_{2h} (this procedure is implemented in the IrRep Phyton code [65]). These calculated irreps agree with a previous study [9]. The saddle point closest to the Fermi level has M_1^+ character, and we show a cut of the magnitude squared of its wavefunction in Figure 5.1b, which is of the p-type, using the terminology introduced in Chapter 2.

In terms of atomic orbitals, the d_{z^2} and $d_{x^2-y^2}$ orbitals are the ones that transform under the M_1^+ irrep. In Figure 5.1c we show the orbital projections on top of the band structure, where we can see that the saddle point closest to the Fermi level, is in fact dominated by the vanadium d_{z^2} orbital, but also gets contributions by $d_{x^2-y^2}$ and d_{xy}. The reason why d_{xy} is present, is that in the global coordinate system $d_{x^2-y^2}$ and d_{xy} get mixed together, while we would only have $d_{x^2-y^2}$ in the local coordinates. This also explains the shape of the wavefunction in Figure 5.1b. More in general, we see that the physics of the system around the Fermi level is dominated by the antimony p_z and the vanadium d orbitals. In particular, the electron pocket around Γ, shown as the cylindrical surface in the Fermi surface in Figure 5.1d, is generated by the antimony p_z orbitals, while the hexagonal sheet that almost touches the M points is generated by the vanadium d orbitals.

The next step is to fully relax the unit cell and the internal atomic coordinates, i.e., minimizing the forces defined in equation 4.59 through a Broyden method implemented in Abinit, until every force is smaller in modulus than 1 meV/Å. Since the system is constrained to keep the same number of atoms and remain in the same space group, this procedure will find a structure that represents either a local minima or a saddle point

[1] In Abinit, this corresponds to setting the variable *occopt* to the value 7.

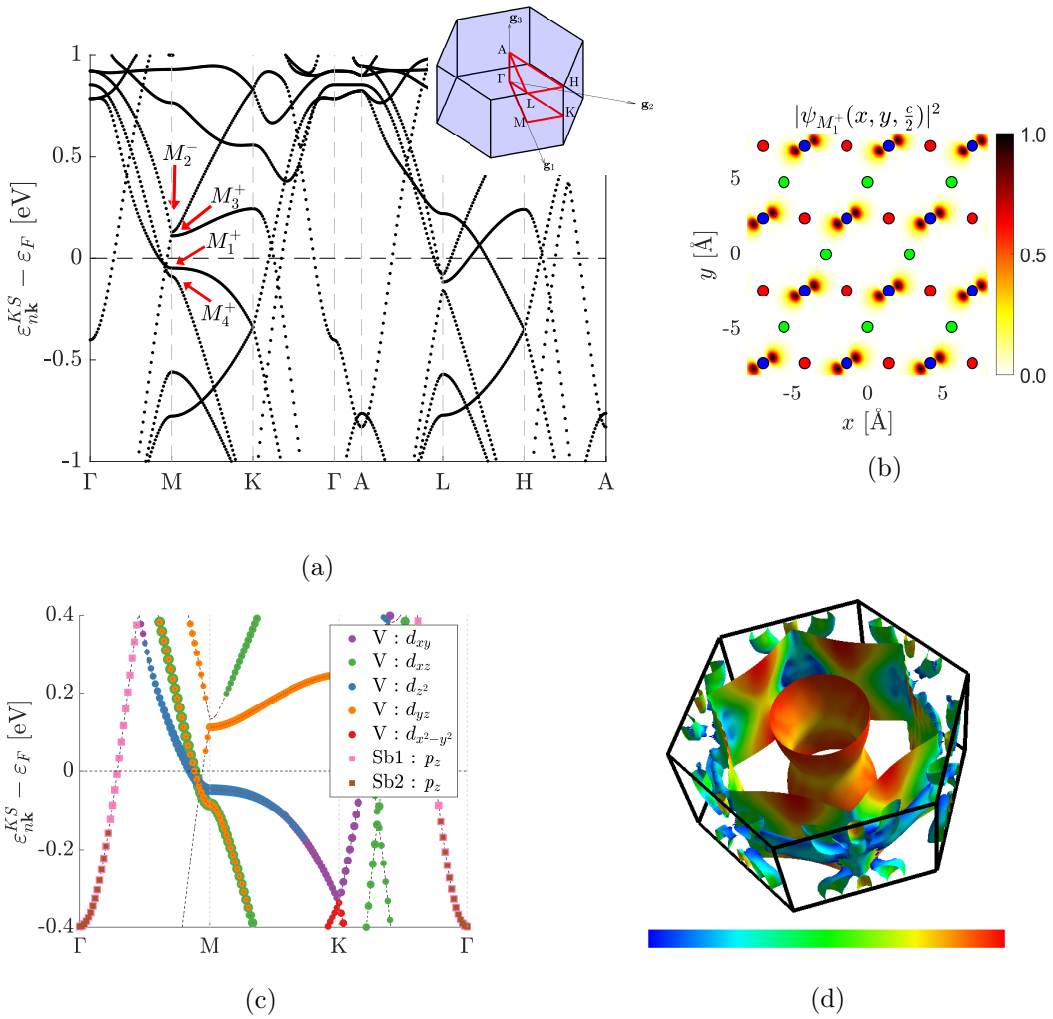

(a) (b) (c) (d)

Figure 5.1: (a) Calculated band structure for CsV_3Sb_5, along the high-symmetry k-path drawn as a red line in the BZ, shown in the inset. For the four saddle point that are closest to the Fermi level, we indicate the irrep of the corresponding eigenfunction. (b) Section of the magnitude squared of the M_1^+ eigenfunction, with the three kagome atoms shown in different colors. The wavefunction is mostly localized around one of the three, in this case the blue one. (c) Orbital projection of the wavefunctions. The energy windows around the Fermi level is dominated by vanadium d orbitals and antimony p_z orbitals. (d) Fermi surface obtained using *FermiSurfer* [64], with the color representing the magnitude of the Fermi velocity in arbitrary units.

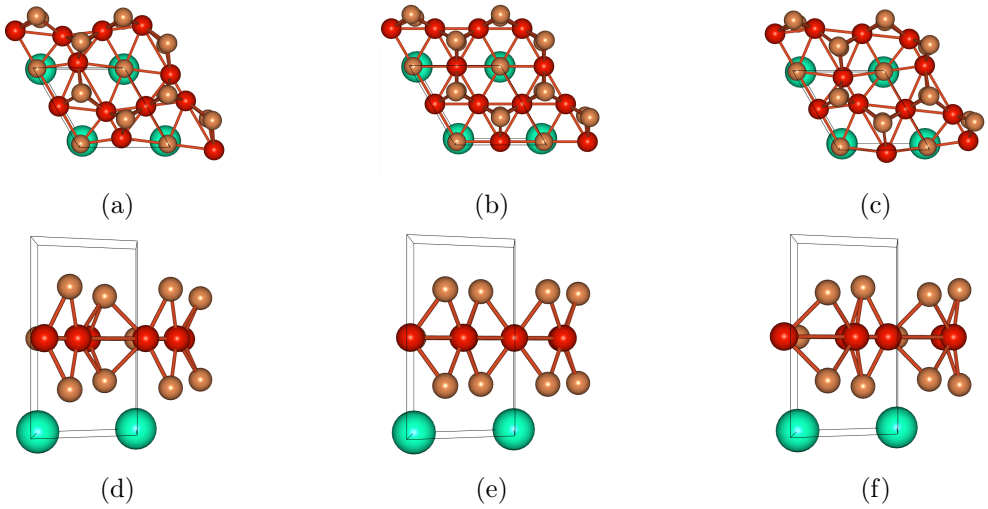

Figure 5.2: Lattice distortions caused by the unstable phonon mode M_1^+, shown from above the kagome plane (a-b-c) and from the side (d-e-f), with negative magnitude(a-d), zero magnitude (b-e) and positive magnitude (c-f).

in the Born-Oppenheimer energy surface. We find the relaxed lattice parameters to be $a = 5.5755$ Å and $c = 9.1107$ Å, and the reduced out-of-plane coordinate of the Sb2 atoms to be $z = 0.7451$.

Now that we have the relaxed structure, we can calculate the phonon properties. In particular, using DFPT as implemented in Abinit, we calculate the phonons at the **M** point $\mathbf{q} = (\frac{1}{2}, 0, 0)$. We find that the lowest phonon mode is unstable, and has imaginary energy $\omega_{1\mathbf{M}} = 3.73i$ meV. Moreover, this phonon mode (the eigenvector of the Dynamical matrix corresponding to the $\omega^2_{1\mathbf{M}}$ eigenvalue) transforms like the M_1^+ irrep. In terms of atomic displacements of the vanadium atoms, this mode indeed looks exactly like the M_1^+ mode that we discussed in Chapter 2 (Figure 3.3), but also includes some out-of-plane motion of the antimony Sb2 atoms, shown in Figure 5.2. The role of the apical antimony ions has been put under scrutiny in a recent work [66], where it has been shown that they could heavily contribute to the stabilization of the CDW phase.

In reference [41], it is mentioned that the amount of instability of the M_1^+ phonon mode is heavily dependent on the electronic smearing temperature, which is an evidence of the role played by the electronic degrees of freedom in the CDW instability. Here, we proceed with a similar caluclation: we introduce a background charge, equivalent to a fraction of an electron, uniformly distribuited through the unit cell, such that the new density of charge is $n_x(\mathbf{r}) = n(\mathbf{r}) + e \cdot x$. For small values of x, this should simulate the effect of electron doping. We calculate the band structures and the lowest phonon mode at **M**, for different values of x and show the results in Figure 5.3. As the M_1^+ saddle point crosses the Fermi level, the instability disappears (notice that for $x = 0.05$ the saddle point is already inside the 10 meV smearing window). This result is in agreement with recent experimental evidence [67], where the electron doping was achieved by substituting vanadium atoms with Titanium ones, and the critical doping value for the suppression of the CDW was determined to be between $x = 0.04$ and $x = 0.09$.

This result suggests that the quasi-2D hexagonal sheet coming from the M_1^+ saddle point, could be playing some critical role in the CDW formation. To further investigate the validity of this point, we turn our focus to the Fermi surface and calculate the Lindhard function

$$\mathcal{L}(\mathbf{q}) = \frac{1}{N} \sum_{ij,\mathbf{k}} \frac{f(\varepsilon_{j\mathbf{k}+\mathbf{q}}) - f(\varepsilon_{i\mathbf{k}})}{\varepsilon_{i\mathbf{k}} - \varepsilon_{j\mathbf{k}+\mathbf{q}}}\,, \tag{5.1}$$

where we take $\varepsilon_{i\mathbf{k}}$ to be the KS eigenvalues for six bands around the Fermi level (numbers

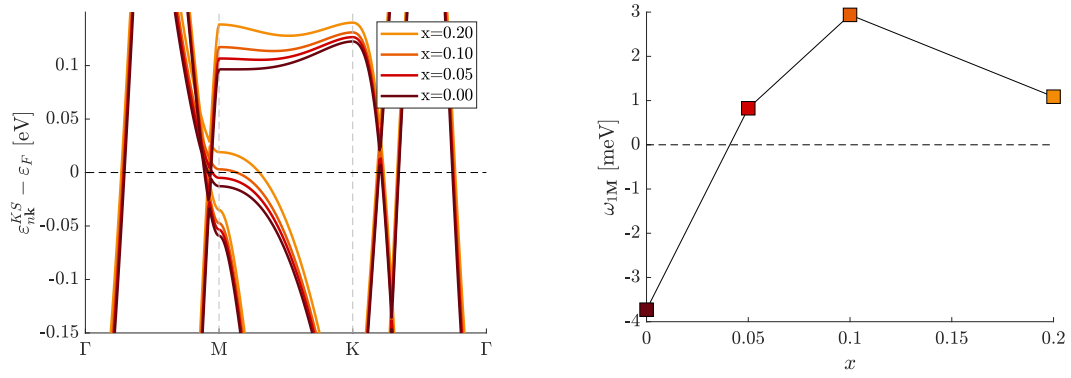

(a) (b)

Figure 5.3: (a) Comparison of the bands closest to the Fermi level around the M point, as a function of simulated doping x. (b) Frequency of the lowest phonon mode $\omega_{1\mathbf{M}}$ at the M point as a function of simulated doping x. The imaginary frequency is reported as negative for better visualization.

60-65 in our calculation). The Lindhard function is also referred to as the *nesting* function, since it contains the information of how much the Fermi surface is nested by the particular vector $\mathbf{q}$. In Figure 5.4 we show the calculated values of $\mathcal{L}(\mathbf{q})$ for a mesh of 16x16 $\mathbf{q}$-points over the BZ at $q_z = 0$, for the different values of simulated doping x. The $x = 0$ case agrees with previous results [68, 69]. For all four panels of Figure 5.4, there is no relative peak at the $\mathbf{M}$ points: not even in the $x = 0$ case, which is the unstable one. This means that (at least at the DFT level), there is no electronic instability driven by bare Fermi surface nesting that can explain the CDW transition.

Since DFT is able to predict the lattice instability, in a future work we might analyze the full bare electronic susceptibility[2]

$$\chi_0(\mathbf{q}) = \frac{1}{N} \sum_{ij,\mathbf{k}} \frac{f(\varepsilon_{j\mathbf{k}+\mathbf{q}}) - f(\varepsilon_{i\mathbf{k}})}{\varepsilon_{i\mathbf{k}} - \varepsilon_{j\mathbf{k}+\mathbf{q}} + i0^+} |\langle \psi_{i\mathbf{k}} | \psi_{j\mathbf{k}+\mathbf{q}} \rangle|^2 \,, \tag{5.2}$$

which also includes the matrix elements, i.e., the overlaps between different wavefunctions $\langle \psi_{i\mathbf{k}} | \psi_{j\mathbf{k}+\mathbf{q}} \rangle$. The reason why this would be interesting is that, given the peculiar nature of the kagome lattice and the phenomenon of sub-lattice interference, the orbital characters of the wavefunctions could be playing an important role, which cannot be accounted by only using the eigenvalues. In this work, we were only able to exclude a simple link between the CDW in CsV_3Sb_5 and Fermi surface nesting.

[2]The Lindhard function we defined above, is also referred in the literature as the real part of the bare electronic susceptibility with constant matrix element approximation.

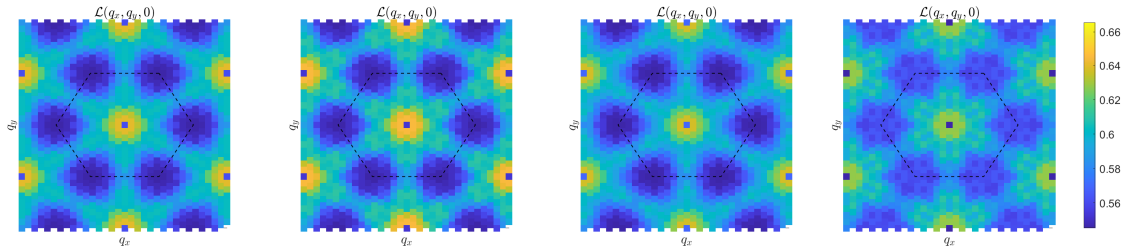

$x = 0.00$ $x = 0.05$ $x = 0.10$ $x = 0.20$

Figure 5.4: Comparison of the Lindhard/nesting function in eq. 5.1 for different values of simulated doping. Notice that there is no relative peak at the **M** points, no matter the value of x. The function has been normalized by the number of bands and **k**-points, so that it can only take values between 0 and 1.

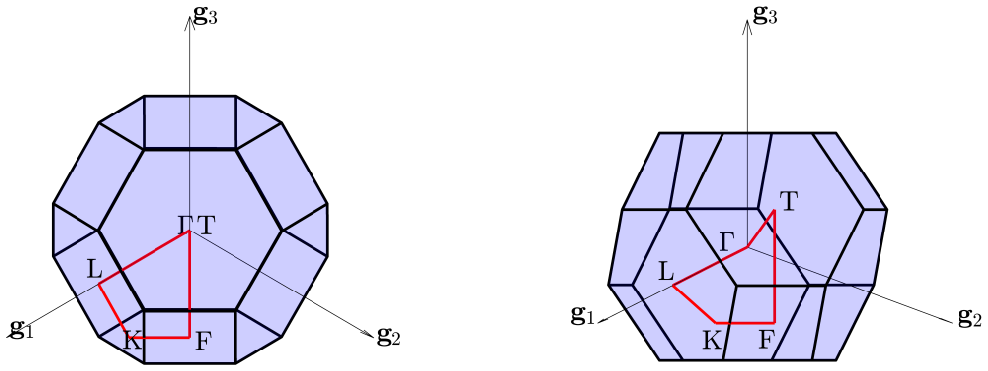

(a) (b)

Figure 5.5: Two different views of the three dimensional $R\bar{3}m$ BZ, with the **k**-path used for band structures highlighted as a red line.

Shandites $M_3A_2Ch_2$

We now turn our attention to the shandite kagome-layered compounds. In Chapter 3, we saw that the **F** point in the $R\bar{3}m$ BZ is analogous to the **M** point in $P6/mmm$. Furthermore, $R\bar{3}m$ can allow for a symmetry based phenomenological theory of a structural transition that doubles the unit cell and looks qualitatively the same as the one for $P6/mmm$. Despite these considerations, at the moment it looks like no shandite structured material has been found to undergo a CDW modulated by the **F** vector. To gain more insight, we turn to DFT calculations: our objective is to find a material whose electronic structure looks fairly similar to the AV_3Sb_5 one.

Let us start with the compound $Rh_3Sn_2S_2$, isoelectronic to $Co_3Sn_2S_2$, simulated using the PBE GGA functional, a Γ centered 16x16x16 **k**-point grid and a basis of PAW with energy cutoff of 500 eV. For the electronic occupation (the $f_{i\mathbf{k}}$ in equation 4.51), we use a Gaussian smearing scheme[3] with smearing temperature of 10 meV. We first fully relax the structure, until every force is smaller in modulus than 1 meV/Å, obtaining values fairly close to the ones reported in Reference [46]. Using the rhombohedral primitive cell, after relaxation we find the length of the primitive translation to be $a = 5.4914$ Å and the angles between the three vectors to be $\alpha = 61.68°$, while the parameter necessary for the Wyckoff position c of the sulphur atom is $z = 0.7113$. With these parameters, we calculate the ground state properties and then interpolate the KS eigenvalues over the **k**-path presented in Figure 5.5.

[3] In Abinit, this corresponds to setting the variable *occopt* to the value 7.

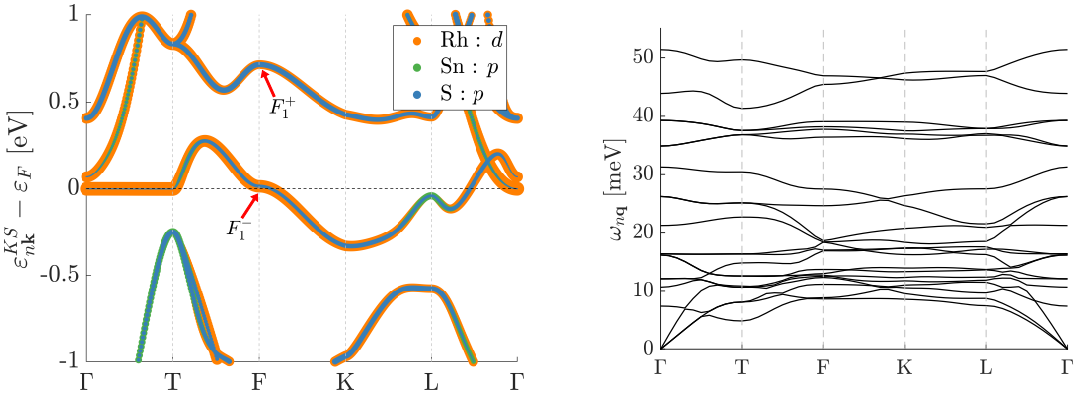

(a) (b)

Figure 5.6: (a) Electronic band structure of $Rh_3Sn_2S_2$ calculated with DFT. The three colors represent the orbital projections of the wavefunctions corresponding to each eigenvalue. Moreover, for the two saddle points at **F**, we report the little group irrep that labels the symmetry of the wavefunctions. (b) Phonon spectrum of $Rh_3Sn_2S_2$ calculated with DFPT. No phonon mode is unstable, such that we confirm this structure to be stable in the shandite structure.

(a) (b)

Figure 5.7: Magnitude of the wavefunctions of $Rh_3Sn_2S_2$ at the **F** point, for the saddle points with symmetries labeled by little group irreps (a) F_1^-, (b) F_1^+ shown in Figure 5.6a. The cuts are taken on the kagome plane, and the three kagome atoms are depicted with red, green and blue.

The resulting band structure is displayed in Figure 5.6a, with the colors indicating the orbital projection of the wavefunctions corresponding to each eigenvalue. At the Fermi level, the 4*d* orbitals of rhodium give the dominant contribution, with a completely flat band between Γ and **T** and a saddle point at **F**. In the figure we also report the irrep label that describes the symmetry of the wavefunction at the **F** point. As we can see, the saddle point that is very close to the Fermi level has F_1^- character and its associated wavefunction is of the m-type. The other saddle point, located around 0.7 eV above the Fermi level, has F_1^+ character and it is of the p-type, with the wavefunction mostly localized around just one of the kagome sites. It is interesting to note that in this case, the saddle point F_1^+ gets a significant contribution from the p orbitals of the apical sulphur ion, shown in blue in Figure 5.6a. We show the wavefunctions associated to the two saddle points in Figure 5.7.

Using DFPT, we calculate the full phonon spectrum using a 4x4x4 **q**-point grid centered at Γ. The resulting band structure, interpolated over the same path as before, is shown in Figure 5.6b. In the calculated spectrum, no phonon mode has imaginary frequencies, so that we confirm $Rh_3Sn_2S_2$ to be stable in the shandite structure.

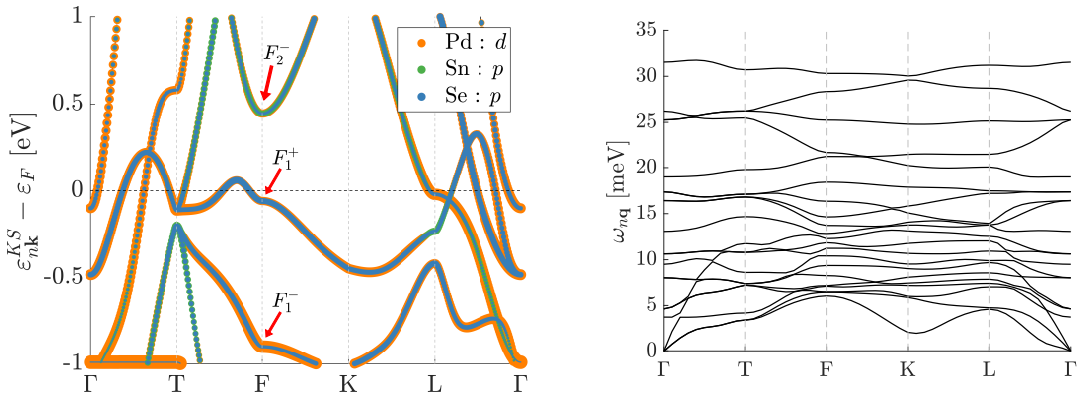

(a) (b)

Figure 5.8: (a) Electronic band structure of $Pd_3Sn_2Se_2$ calculated with DFT. The three colors represent the orbital projections of the wavefunctions corresponding to each eigenvalue. Moreover, for the two saddle points at **F**, we report the little group irrep that labels the symmetry of the wavefunctions. (b) Phonon spectrum of $Pd_3Sn_2Se_2$ calculated with DFPT. No phonon mode is unstable, such that we predict this structure to be stable in the shandite structure.

We simulated different shandite materials, aiming to identify structural instabilities and electronic band structures that closely resemble that of AV_3Sb_5 in terms of having a saddle point exhibiting F_1^+ character (p-type wavefunction) in close proximity to the Fermi level. However, none of the compounds we examined displayed any signs of instability under our simulation conditions. In Appendix B we show the resulting band structures and lattice parameters for the compounds that we simulated.

Let us take a look at $Pd_3Sn_2Se_2$, which we simulate using the same settings as $Rh_3Sn_2S_2$. Relaxing the structure leads us to find the lattice parameters $a = 5.8188$ Å and $\alpha = 59.82°$, with the parameter for the c position of the selenium ion $z = 0.70564$. In Figure 5.8a we show the band structure obtained by interpolating the KS eigenvalues along the **k**-path and the orbital projection of the wavefunctions. In this material, the saddle point with F_1^+ is around 60 meV below the Fermi level. In Figure 5.9 we also show the magnitude in the kagome plane of the wavefunctions at the **M** point. Notice another striking difference with the AV_3Sb_5 in the role of apical ions: the F_1^+ p-type saddle point is not completely dominated by the d orbitals of the kagome atoms, but instead also gets an almost equal contribution from the selenium p orbitals.

In Chapter 2, we briefly mentioned the observation that in shandite materials the kagome layers appear to be much closer to each other compared to kagome metals. For instance, the inter-layer distance in CsV_3Sb5 was found to be approximately 9.11 Å, whereas in the relaxed structure of $Pd_3Sn_2Se_2$, it is about half of that, approximately 4.75 Å. However, despite this reduced inter-layer distance, the distance between the apical ions and the kagome planes is not significantly affected. In CsV_3Sb5, the distance between the apical antimony and the vanadium kagome atoms is approximately 2.77 Å. In $Pd_3Sn_2Se_2$, the distances between the apical selenium and the palladium kagome atoms are around 2.29 Å, while the distance between the apical tin and palladium is 2.75 Å.

In future investigations, one could explore these observations in more detail and determine if there is any correlation between these structural characteristics and the apparent absence of CDW in shandites. A recent unpublished work [70] has indicated that the distances between the apical ions and the kagome plane in AV_3Sb5 remain relatively constant under simulated strain along the c-axis. It would be interesting to investigate whether a similar phenomenon occurs in shandites.

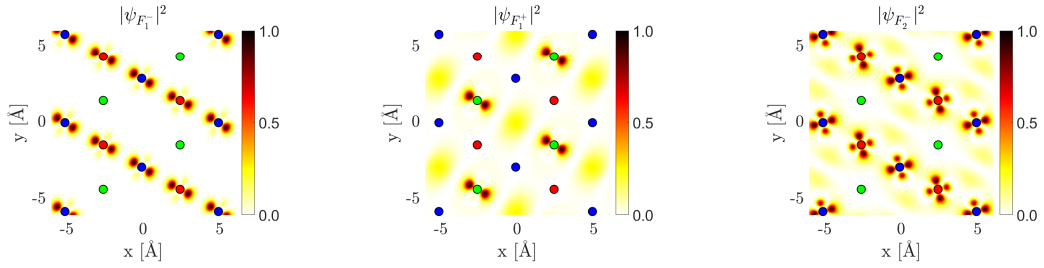

(a) (b) (c)

Figure 5.9: Magnitude of the wavefunctions of $Pd_3Sn_2Se_2$ at the **F** point, for the saddle points with symmetries labeled by little group irreps (a) F_1^-, (b) F_1^+, (c) F_2^- shown in Figure 5.8a . The cuts are taken on the kagome plane, and the three kagome atoms are depicted with red, green and blue.

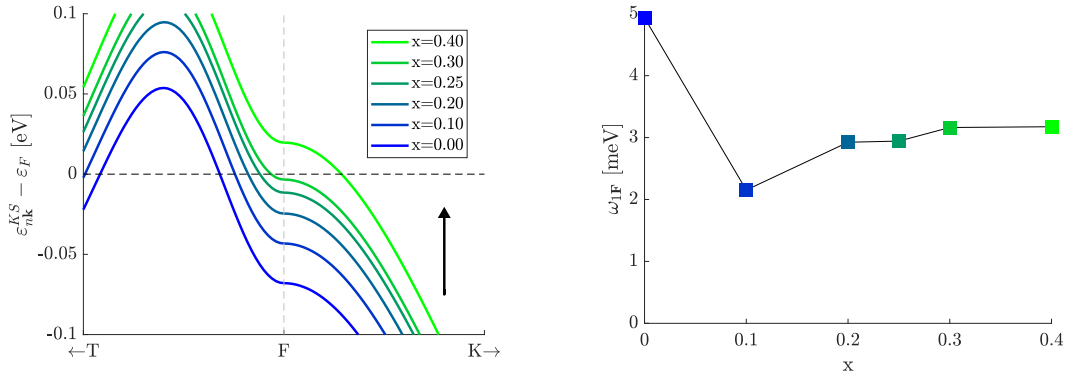

(a) (b)

Figure 5.10: (a) Comparison of the bands closest to the Fermi level around the **F** point, as a function of simulated doping x. (b) Frequency of the lowest phonon mode $\omega_{1\mathbf{F}}$ at the **F** point as a function of simulated doping x.

Using DFPT we also calculate the full phonon spectrum on a 4x4x4 **q**-point grid centered at Γ. The resulting phonon bands are shown in Figure 5.8b. Again, we find no imaginary frequency and so no structural instability.

In order to investigate the hypothesis proposed in the preceding chapter, which suggested that the proximity of the p-type saddle point to the Fermi level might contribute to the CDW instability, we conducted simulations involving doping and hydrostatic pressure on $Pd_3Sn_2Se_2$. This approach follows a similar line of inquiry, albeit with an opposing objective, to the previous section. Our aim is to determine whether manipulating the saddle point's position relative to the Fermi level using these methods can induce structural instability. Small amounts of doping are simulated in the same way that was introduced in the last section. Hydrostatic pressure is simulated by enforcing a value of pressure $-P$ in the diagonal elements of the stress tensor[4]. For each value of applied P, we repeat the structural relaxation and calculate ground state properties, band structure and phonons at **F**.

Figure 5.10 and Figure 5.11 depict the outcomes of our simulations. In both scenarios, bringing the saddle point closer to the Fermi level did not lead to the emergence of induced structural instability, as indicated by the absence of imaginary phonon frequencies at **q**=**F**. To provide a comprehensive understanding, we now delve into the relationship between the

[4]This is done in Abinit through the use of the *strtarget* variable.

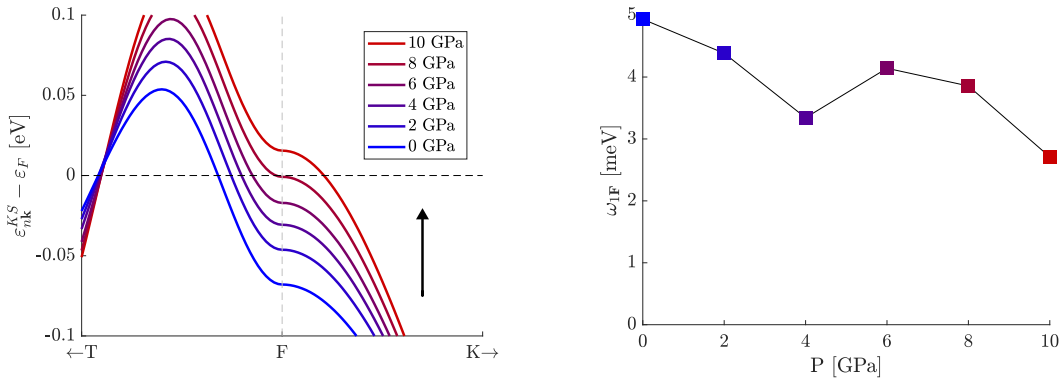

(a) (b)

Figure 5.11: (a) Comparison of the bands closest to the Fermi level around the **F** point, as a function of simulated hydrostatic pressure. (b) Frequency of the lowest phonon mode $\omega_{1\mathbf{F}}$ at the **F** point as a function of simulated hydrostatic pressure.

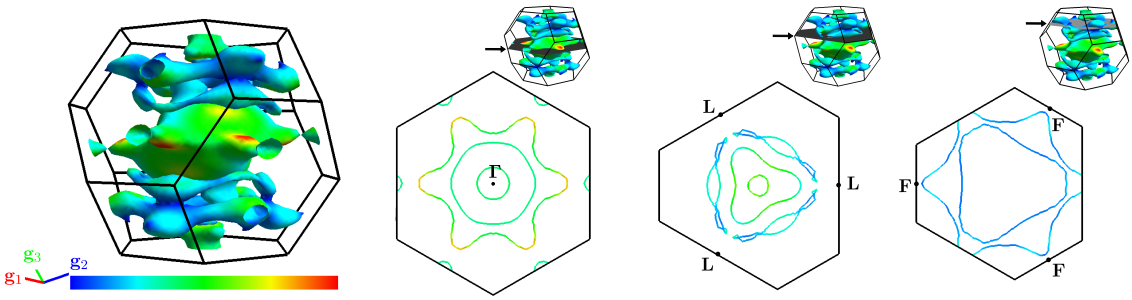

Figure 5.12: Fermi surface for $Pd_3Sn_2Se_2$ with 8 GPa of applied hydrostatic pressure, obtained using *FermiSurfer* [64]. The colors represent the magnitude of the Fermi velocity in arbitrary units. The three panels on the right show 2D sections on the planes that include the **Γ** point, the **L** points and the **F** points, respectively.

saddle point and the Fermi surface, thus completing the overall framework presented in the previous chapter.

The Fermi surface of $Pd_3Sn_2Se_2$ exhibits considerably more dispersion along the k_z direction compared to AV_3Sb_5. Figure 5.12 illustrates the Fermi surface of $Pd_3Sn_2Se_2$ under 8 GPa of applied hydrostatic pressure, wherein the saddle point is expected to coincide precisely with the Fermi level, as depicted in Figure 5.11a. Upon examining various two-dimensional cross-sections, it is not easy to identify hexagonal parts of the Fermi surface that could potentially exhibit nesting characteristics similar to those observed in AV_3Sb_5.

To validate this hypothesis, we performed calculations of the Lindhard function for two specific cases in our simulations: one with a simulated hydrostatic pressure of 8 GPa and another with simulated doping level $x = 0.3$. These are the two cases that bring the saddle point closest to the Fermi level in our calculations. In Figure 5.13, we compare the Lindhard function of these two cases with that of the system under zero doping and zero applied pressure. Notably, none of the three cases exhibit relative peaks at the **F** point (represented by red circles) or the **L** point (represented by blue circles). However, there appears to be a general trend of enhanced response along the **Γ**-**T** line, possibly attributed to the **Γ** and **T** pockets (depicted in the full band structure in Fig. 5.8a, but not in 5.10a-5.11a) moving closer to the Fermi level.

While symmetry considerations did not impose limitations on extending the phe-

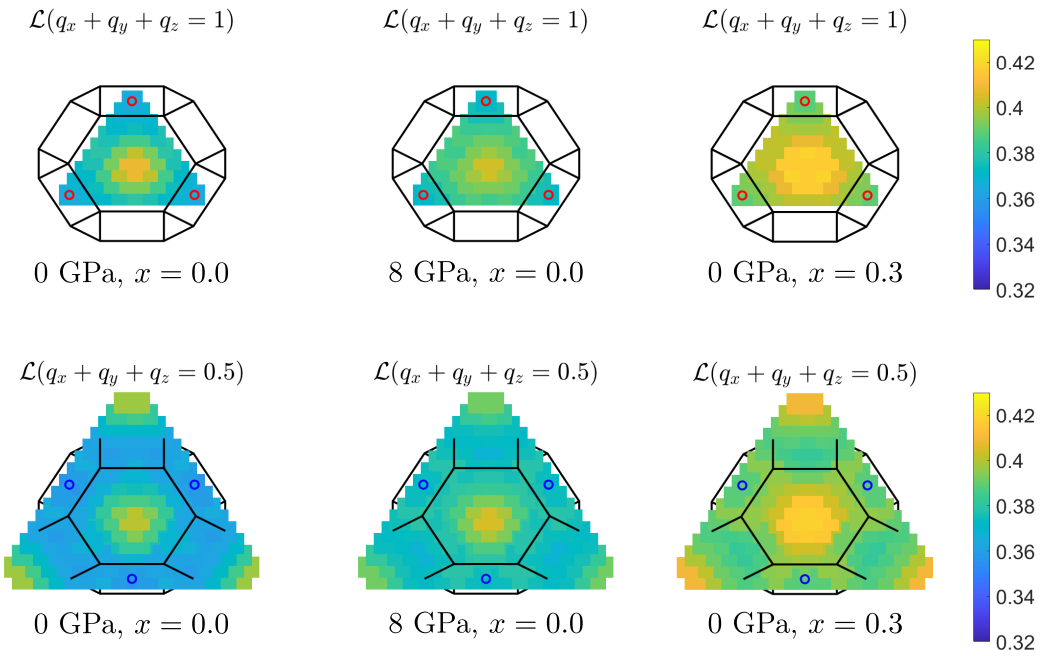

Figure 5.13: Comparison of the Lindhard/nesting function in eq. 5.1 for different values of simulated doping and pressure. We compare the case of no doping and no pressure with the two cases of applied pressure and doping that bring the F_1^+ saddle point closest to the Fermi level. In a similar fashion as Figure 5.12, we show two sections of this function. Top row: section of the function in the plane that contains the **F** points. Bottom row: section of the function in the plane that contains the **L** points. Both are superimposed over the BZ for reference. Notice that in all cases there is no relative peak at the **F** or **L** points. The function has been normalized by the number of bands and **k**-points, so that it can only take values between 0 and 1.

nomenological Landau theory for the structural transition to the $R\bar{3}m$ space group, it is plausible that symmetry plays a role in reducing the nesting behavior of the Fermi surface in shandite systems compared to AV_3Sb5 with the $P6/mmm$ space group. This reduced nesting behavior could be attributed to the $D3d$ point group symmetry of the system, specifically, which might prevent six-fold quasi two-dimensional sheets in the Fermi surface. However, further investigations are required to definitively confirm this hypothesis.

Chapter 6

Conclusion and outlook

Throughout this thesis, our investigation centered on two distinct crystal structures that present kagome layers: AV_3Sb_5 with the $P6/mmm$ space group and shandites $M_3A_2Ch_2$ with the $R\bar{3}m$ space group.We extended the phenomenological Landau theory of CDW-like structural transitions to the shandite crystal structure. By identifying the relevant vector in the Brillouin Zone as the **F** vector, we revealed that kagome layers in the $R\bar{3}m$ system can exhibit ground states characterized by Star-of-David and Tri-Hexagonal lattice distortions, in a same fashion as what is speculated for AV_3Sb_5.

To comprehend the underlying electronic and lattice properties, we gave a brief introduction to the Density Functional Theory and employed it to simulate various compounds of interest.In the case of CsV_3Sb_5, our simulations confirmed the presence of an unstable phonon mode at **M**, consistent with prior calculations. However, we could not establish a clear connection between this mode and any peak in the Lindhard/nesting function, thereby leaving open the question of whether Fermi surface nesting effects contribute significantly to the driving mechanism of the CDW in this system.

Among the shandite compounds examined, we focused our attention on $Pd_3Sn_2Se_2$. We observed the presence of a saddle point at **F**, analogous to the saddle points found at **M** in AV_3Sb_5. However, our simulations under various conditions of pressure and doping did not reveal any structural instability at the **F** point for this compound. Furthermore, we observed that the Fermi surface of $Pd_3Sn_2Se_2$ exhibited reduced two-dimensionality compared to AV_3Sb_5, making it less amenable to nesting phenomena. The main suspects that we can point to as reasons for the apparent absence of the CDW in shandites are: the distance between kagome layers being way smaller than in the kagome metals; the different role played by apical ions, both in the structural configuration and in the electronic structure.

Moving forward, several avenues for further investigation have emerged, including exploring the role of apical ions in both systems, calculating the full bare electronic susceptibility in AV_3Sb_5, continuing the study of different shandite compounds due to their diverse material properties and searching for a shandite exhibiting a CDW, which would lead to a deeper understanding of the nature of the CDW and the interplay between phonons and electronic effects.

In conclusion, this thesis has provided insights into the structural properties of AV_3Sb_5 and shandite compounds, laying the groundwork for future research and investigations into the fascinating aspects and potential applications of shandite materials.

Bibliography

[1] Itiro Syôzi. "Statistics of Kagomé Lattice". In: *Progress of Theoretical Physics* 6.3 (June 1951), pp. 306–308. ISSN: 0033-068X. DOI: 10.1143/ptp/6.3.306. eprint: https://academic.oup.com/ptp/article-pdf/6/3/306/5239621/6-3-306.pdf. URL: https://doi.org/10.1143/ptp/6.3.306.

[2] Leon Balents. "Spin liquids in frustrated magnets". In: *Nature* 464 (Mar. 2010), pp. 199–208. ISSN: 1476-4687. DOI: 10.1038/nature08917.

[3] Wan-Sheng Wang et al. "Competing electronic orders on kagome lattices at van Hove filling". In: *Phys. Rev. B* 87 (11 2013), p. 115135. DOI: 10.1103/PhysRevB.87.115135. URL: https://link.aps.org/doi/10.1103/PhysRevB.87.115135.

[4] Maximilian L. Kiesel, Christian Platt, and Ronny Thomale. "Unconventional Fermi Surface Instabilities in the Kagome Hubbard Model". In: *Phys. Rev. Lett.* 110 (12 2013), p. 126405. DOI: 10.1103/PhysRevLett.110.126405. URL: https://link.aps.org/doi/10.1103/PhysRevLett.110.126405.

[5] Francesco Ferrari, Federico Becca, and Roser Valentí. "Charge density waves in kagome-lattice extended Hubbard models at the van Hove filling". In: *Phys. Rev. B* 106 (8 2022), p. L081107. DOI: 10.1103/PhysRevB.106.L081107. URL: https://link.aps.org/doi/10.1103/PhysRevB.106.L081107.

[6] F. H. Yu et al. "Unusual competition of superconductivity and charge-density-wave state in a compressed topological kagome metal". In: *Nat. Commun.* 12.3645 (June 2021), pp. 1–6. ISSN: 2041-1723. DOI: 10.1038/s41467-021-23928-w.

[7] Shuo-Ying Yang et al. "Giant, unconventional anomalous Hall effect in the metallic frustrated magnet candidate, KV_3Sb_5". In: *Science Advances* 6.31 (2020), eabb6003. DOI: 10.1126/sciadv.abb6003. URL: https://www.science.org/doi/abs/10.1126/sciadv.abb6003.

[8] M. Kanagaraj, Jiai Ning, and Liang He. "Topological Co3Sn2S2 magnetic Weyl semimetal: From fundamental understanding to diverse fields of study". In: *Reviews in Physics* 8 (2022), p. 100072. ISSN: 2405-4283. DOI: https://doi.org/10.1016/j.revip.2022.100072. URL: https://www.sciencedirect.com/science/article/pii/S2405428322000041.

[9] Morten H. Christensen et al. "Loop currents in AV_3Sb_5 kagome metals: Multipolar and toroidal magnetic orders". In: *Phys. Rev. B* 106 (14 2022), p. 144504. DOI: 10.1103/PhysRevB.106.144504. URL: https://link.aps.org/doi/10.1103/PhysRevB.106.144504.

[10] Rudolf Ernst Peierls. "Quantum theory of solids". In: (1955). URL: https://cds.cern.ch/record/1988113.

[11] M. D. Johannes and I. I. Mazin. "Fermi surface nesting and the origin of charge density waves in metals". In: *Phys. Rev. B* 77 (16 2008), p. 165135. DOI: 10.1103/PhysRevB.77.165135. URL: https://link.aps.org/doi/10.1103/PhysRevB.77.165135.

[12] Y. Okamura et al. "Giant magneto-optical responses in magnetic Weyl semimetal Co3Sn2S2". In: *Nat. Commun.* 11.4619 (Sept. 2020), pp. 1–8. ISSN: 2041-1723. DOI: 10.1038/s41467-020-18470-0.

[13] Irina Anusca et al. "Half Antiperovskites: IV. Crystallographic and Electronic Structure Investigations on A2Rh3S2 (A = In, Sn, Tl, Pb, Bi)". In: *Z. Anorg. Allg. Chem.* 635.15 (Dec. 2009), pp. 2410–2428. ISSN: 0044-2313. DOI: 10.1002/zaac.200900113.

[14] F. H. Yu et al. "Pressure-induced superconductivity in a shandite compound Pd3Pb2Se2 with the Kagome lattice". In: *New J. Phys.* 22.12 (Dec. 2020), p. 123013. ISSN: 1367-2630. DOI: 10.1088/1367-2630/abcef6.

[15] Surajit Basak, Aksel Kobiałka, and Andrzej Ptok. *$T_3Pb_2Ch_2$ (T=Pd,Pt and Ch=S,Se) with transition metal kagome net: Dynamical properties, phonon nodal line, phonon surface states, and chiral phonons*. 2023. arXiv: 2303.13328 [cond-mat.mtrl-sci].

[16] Brenden R. Ortiz et al. "New kagome prototype materials: discovery of KV_3Sb_5, RbV_3Sb_5, and CsV_3Sb_5". In: *Phys. Rev. Mater.* 3 (9 2019), p. 094407. DOI: 10.1103/PhysRevMaterials.3.094407. URL: https://link.aps.org/doi/10.1103/PhysRevMaterials.3.094407.

[17] Brenden R. Ortiz et al. "Superconductivity in the $\mathbb{Z}_2$ kagome metal KV_3Sb_5". In: *Phys. Rev. Mater.* 5 (3 2021), p. 034801. DOI: 10.1103/PhysRevMaterials.5.034801. URL: https://link.aps.org/doi/10.1103/PhysRevMaterials.5.034801.

[18] Qiangwei Yin et al. "Superconductivity and Normal-State Properties of Kagome Metal RbV3Sb5 Single Crystals". In: *Chin. Phys. Lett.* 38.3 (Mar. 2021), p. 037403. ISSN: 0256-307X. DOI: 10.1088/0256-307X/38/3/037403.

[19] Brenden R. Ortiz et al. "CsV_3Sb_5: A $\mathbb{Z}_2$ Topological Kagome Metal with a Superconducting Ground State". In: *Phys. Rev. Lett.* 125 (24 2020), p. 247002. DOI: 10.1103/PhysRevLett.125.247002. URL: https://link.aps.org/doi/10.1103/PhysRevLett.125.247002.

[20] Mois I. Aroyo et al. "Brillouin-zone database on the Bilbao Crystallographic Server". In: *Acta Crystallographica Section A* 70.2 (2014), pp. 126–137. DOI: 10.1107/S205327331303091X. URL: https://doi.org/10.1107/S205327331303091X.

[21] Yu-Xiao Jiang et al. "Unconventional chiral charge order in kagome superconductor KV3Sb5". In: *Nat. Mater.* 20 (Oct. 2021), pp. 1353–1357. ISSN: 1476-4660. DOI: 10.1038/s41563-021-01034-y.

[22] Q. Stahl et al. "Temperature-driven reorganization of electronic order in CsV_3Sb_5". In: *Phys. Rev. B* 105 (19 2022), p. 195136. DOI: 10.1103/PhysRevB.105.195136. URL: https://link.aps.org/doi/10.1103/PhysRevB.105.195136.

[23] Jean-Paul Pouget. "The Peierls instability and charge density wave in one-dimensional electronic conductors". In: *Comptes Rendus Physique* 17.3 (2016). Physique de la matière condensée au XXIe siècle: l'héritage de Jacques Friedel, pp. 332–356. ISSN: 1631-0705. DOI: https://doi.org/10.1016/j.crhy.2015.11.008. URL: https://www.sciencedirect.com/science/article/pii/S163107051500225X.

[24] Haoxiang Li et al. "Observation of Unconventional Charge Density Wave without Acoustic Phonon Anomaly in Kagome Superconductors AV_3Sb_5 (A = Rb, Cs)". In: *Phys. Rev. X* 11.3 (Sept. 2021), p. 031050. ISSN: 2160-3308. DOI: 10.1103/PhysRevX.11.031050.

[25] Brenden R. Ortiz et al. "Fermi Surface Mapping and the Nature of Charge-Density-Wave Order in the Kagome Superconductor CsV_3Sb_5". In: *Phys. Rev. X* 11.4 (Nov. 2021), p. 041030. ISSN: 2160-3308. DOI: 10.1103/PhysRevX.11.041030.

[26] Hailan Luo et al. "Electronic nature of charge density wave and electron-phonon coupling in kagome superconductor KV3Sb5". In: *Nat. Commun.* 13.273 (Jan. 2022), pp. 1–8. ISSN: 2041-1723. DOI: 10.1038/s41467-021-27946-6.

[27] Noah Ratcliff et al. "Coherent phonon spectroscopy and interlayer modulation of charge density wave order in the kagome metal CsV_3Sb_5". In: *Phys. Rev. Mater.* 5.11 (Nov. 2021), p. L111801. ISSN: 2475-9953. DOI: 10.1103/PhysRevMaterials.5.L111801.

[28] Li Yu et al. "Evidence of a hidden flux phase in the topological kagome metal CsV_3Sb_5". In: (2021). arXiv: 2107.10714 [cond-mat.supr-con].

[29] Qiong Wu et al. "Simultaneous formation of two-fold rotation symmetry with charge order in the kagome superconductor CsV_3Sb_5 by optical polarization rotation measurement". In: *Phys. Rev. B* 106 (20 2022), p. 205109. DOI: 10.1103/PhysRevB.106.205109. URL: https://link.aps.org/doi/10.1103/PhysRevB.106.205109.

[30] Hong Li et al. "Rotation symmetry breaking in the normal state of a kagome superconductor KV3Sb5". In: *Nat. Phys.* 18 (Mar. 2022), pp. 265–270. ISSN: 1745-2481. DOI: 10.1038/s41567-021-01479-7.

[31] Takamori Park, Mengxing Ye, and Leon Balents. "Electronic instabilities of kagome metals: Saddle points and Landau theory". In: *Phys. Rev. B* 104 (3 2021), p. 035142. DOI: 10.1103/PhysRevB.104.035142. URL: https://link.aps.org/doi/10.1103/PhysRevB.104.035142.

[32] Lixuan Zheng et al. *Emergent charge order and unconventional superconductivity in pressurized kagome superconductor CsV3Sb5*. 2022. arXiv: 2209.07340 [cond-mat.supr-con].

[33] Jian-Feng Zhang, Kai Liu, and Zhong-Yi Lu. "First-principles study of the double-dome superconductivity in the kagome material CsV_3Sb_5 under pressure". In: *Phys. Rev. B* 104 (19 2021), p. 195130. DOI: 10.1103/PhysRevB.104.195130. URL: https://link.aps.org/doi/10.1103/PhysRevB.104.195130.

[34] C. C. Zhu et al. "Double-dome superconductivity under pressure in the V-based kagome metals AV_3Sb_5 (A = Rb and K)". In: *Phys. Rev. B* 105 (9 2022), p. 094507. DOI: 10.1103/PhysRevB.105.094507. URL: https://link.aps.org/doi/10.1103/PhysRevB.105.094507.

[35] Chongze Wang et al. "Charge density wave and superconductivity in the kagome metal CsV_3Sb_5 around a pressure-induced quantum critical point". In: *Phys. Rev. Mater.* 6 (9 2022), p. 094801. DOI: 10.1103/PhysRevMaterials.6.094801. URL: https://link.aps.org/doi/10.1103/PhysRevMaterials.6.094801.

[36] Jian-Guo Si et al. "Charge density wave and pressure-dependent superconductivity in the kagome metal CsV_3Sb_5: A first-principles study". In: *Phys. Rev. B* 105 (2 2022), p. 024517. DOI: 10.1103/PhysRevB.105.024517. URL: https://link.aps.org/doi/10.1103/PhysRevB.105.024517.

[37] F. Marsiglio. "Eliashberg theory: A short review". In: *Annals of Physics* 417 (2020). Eliashberg theory at 60: Strong-coupling superconductivity and beyond, p. 168102. ISSN: 0003-4916. DOI: https://doi.org/10.1016/j.aop.2020.168102. URL: https://www.sciencedirect.com/science/article/pii/S000349162030035X.

[38] E. R. Margine and F. Giustino. "Anisotropic Migdal-Eliashberg theory using Wannier functions". In: *Phys. Rev. B* 87 (2 2013), p. 024505. DOI: 10.1103/PhysRevB.87.024505. URL: https://link.aps.org/doi/10.1103/PhysRevB.87.024505.

[39] R.C. Dynes. "McMillan's equation and the Tc of superconductors". In: *Solid State Communications* 10.7 (1972), pp. 615–618. ISSN: 0038-1098. DOI: https://doi.org/10.1016/0038-1098(72)90603-5. URL: https://www.sciencedirect.com/science/article/pii/0038109872906035.

[40] Hengxin Tan et al. “Charge Density Waves and Electronic Properties of Superconducting Kagome Metals”. In: *Phys. Rev. Lett.* 127 (4 2021), p. 046401. DOI: 10.1103/PhysRevLett.127.046401. URL: https://link.aps.org/doi/10.1103/PhysRevLett.127.046401.

[41] Morten H. Christensen et al. “Theory of the charge density wave in AV_3Sb_5 kagome metals”. In: *Phys. Rev. B* 104 (21 2021), p. 214513. DOI: 10.1103/PhysRevB.104.214513. URL: https://link.aps.org/doi/10.1103/PhysRevB.104.214513.

[42] P. Ramdohr. *Das Vorkommen von Heazlewoodit Ni3S2 und ueber ein neues ihn begleitendes Mineral: Shandit Ni3Pb2S2*. Sitzungsberichte der Deutschen Akademie der Wissenschaften zu Berlin, Mathematisch-Naturwissenschaftliche Klasse. Akademie-Verlag, 1950. URL: https://books.google.dk/books?id=jfzivgEACAAJ.

[43] Richard Weihrich, Irina Anusca, and Manfred Zabel. “Halbantiperowskite: Zur Struktur der Shandite M3/2AS (M = Co, Ni; A = In, Sn) und ihren Typ-Antitypbeziehungen”. In: *Zeitschrift für anorganische und allgemeine Chemie* 631.8 (2005), pp. 1463–1470. DOI: https://doi.org/10.1002/zaac.200400561. URL: https://onlinelibrary.wiley.com/doi/abs/10.1002/zaac.200400561.

[44] Richard Weihrich and Irina Anusca. “Halbantiperowskite II: zur Kristallstruktur des Pd3Bi2S2”. In: *Zeitschrift für anorganische und allgemeine Chemie* 632.2 (2006), pp. 335–342. DOI: https://doi.org/10.1002/zaac.200500336. URL: https://onlinelibrary.wiley.com/doi/abs/10.1002/zaac.200500336.

[45] Richard Weihrich and Irina Anusca. “Half Antiperovskites. III. Crystallographic and Electronic Structure Effects in Sn2xInxCo3S2”. In: *Zeitschrift für anorganische und allgemeine Chemie* 632.8-9 (2006), pp. 1531–1537. DOI: https://doi.org/10.1002/zaac.200500524. URL: https://onlinelibrary.wiley.com/doi/abs/10.1002/zaac.200500524.

[46] Irina Anusca et al. “Half Antiperovskites: IV. Crystallographic and Electronic Structure Investigations on A2Rh3S2 (A = In, Sn, Tl, Pb, Bi) ”. In: *Zeitschrift für anorganische und allgemeine Chemie* 635.15 (2009), pp. 2410–2428. DOI: https://doi.org/10.1002/zaac.200900113. URL: https://onlinelibrary.wiley.com/doi/abs/10.1002/zaac.200900113.

[47] Richard Weihrich et al. “Structure, ordering, and bonding of half antiperovskites: PbNi3/2S and BiPd3/2S”. In: *Progress in Solid State Chemistry* 35.2 (2007). International Conference on Perovskites at EMPA, 2005., pp. 309–327. ISSN: 0079-6786. DOI: https://doi.org/10.1016/j.progsolidstchem.2007.01.011. URL: https://www.sciencedirect.com/science/article/pii/S0079678607000106.

[48] D. F. Liu et al. “Magnetic Weyl semimetal phase in a Kagomé crystal”. In: *Science* 365.6459 (2019), pp. 1282–1285. DOI: 10.1126/science.aav2873. URL: https://www.science.org/doi/abs/10.1126/science.aav2873.

[49] Enke Liu et al. “Giant anomalous Hall effect in a ferromagnetic kagome-lattice semimetal”. In: *Nat. Phys.* 14 (Nov. 2018), pp. 1125–1131. ISSN: 1745-2481. DOI: 10.1038/s41567-018-0234-5.

[50] Qi Wang et al. “Large intrinsic anomalous Hall effect in half-metallic ferromagnet Co3Sn2S2 with magnetic Weyl fermions”. In: *Nat. Commun.* 9.3681 (Sept. 2018), pp. 1–8. ISSN: 2041-1723. DOI: 10.1038/s41467-018-06088-2.

[51] M. Kanagaraj, Jiai Ning, and Liang He. “Topological Co3Sn2S2 magnetic Weyl semimetal: From fundamental understanding to diverse fields of study”. In: *Reviews in Physics* 8 (2022), p. 100072. ISSN: 2405-4283. DOI: https://doi.org/10.1016/j.revip.2022.100072. URL: https://www.sciencedirect.com/science/article/pii/S2405428322000041.

[52] Yang Zhang, Yan Sun, and Binghai Yan. "Berry curvature dipole in Weyl semimetal materials: An ab initio study". In: *Phys. Rev. B* 97 (4 2018), p. 041101. DOI: 10.1103/PhysRevB.97.041101. URL: https://link.aps.org/doi/10.1103/PhysRevB.97.041101.

[53] Maximilian L. Kiesel and Ronny Thomale. "Sublattice interference in the kagome Hubbard model". In: *Phys. Rev. B* 86 (12 2012), p. 121105. DOI: 10.1103/PhysRevB.86.121105. URL: https://link.aps.org/doi/10.1103/PhysRevB.86.121105.

[54] H. T. Stokes, D. M. Hatch, and B. J. Campbell. *ISOTROPY Software Suite*. URL: https://stokes.byu.edu/iso/isotropy.php.

[55] Wahyu Setyawan and Stefano Curtarolo. "High-throughput electronic band structure calculations: Challenges and tools". In: *Computational Materials Science* 49.2 (2010), pp. 299–312. ISSN: 0927-0256. DOI: https://doi.org/10.1016/j.commatsci.2010.05.010. URL: https://www.sciencedirect.com/science/article/pii/S0927025610002697.

[56] Daniel Arovas. *Lecture Notes on Group Theory in Physics*. [Online; accessed 22. May 2023]. May 2023. URL: https://courses.physics.ucsd.edu/2016/Spring/physics220/LECTURES/GROUP_THEORY.pdf.

[57] Xavier Gonze and Fabio Finocchi. "Pseudopotentials Plane Waves–Projector Augmented Waves: A Primer". In: *Phys. Scr.* 2004.T109 (Jan. 2004), p. 40. ISSN: 1402-4896. DOI: 10.1238/Physica.Topical.109a00040.

[58] John P. Perdew, Kieron Burke, and Matthias Ernzerhof. "Generalized Gradient Approximation Made Simple". In: *Phys. Rev. Lett.* 77 (18 1996), pp. 3865–3868. DOI: 10.1103/PhysRevLett.77.3865. URL: https://link.aps.org/doi/10.1103/PhysRevLett.77.3865.

[59] Stefano Baroni et al. "Phonons and related crystal properties from density-functional perturbation theory". In: *Rev. Mod. Phys.* 73 (2 2001), pp. 515–562. DOI: 10.1103/RevModPhys.73.515. URL: https://link.aps.org/doi/10.1103/RevModPhys.73.515.

[60] Paolo Giannozzi et al. "Ab initio calculation of phonon dispersions in semiconductors". In: *Phys. Rev. B* 43 (9 1991), pp. 7231–7242. DOI: 10.1103/PhysRevB.43.7231. URL: https://link.aps.org/doi/10.1103/PhysRevB.43.7231.

[61] Xavier Gonze et al. "The Abinit project: Impact, environment and recent developments". In: *Comput. Phys. Commun.* 248 (2020), p. 107042. URL: https://doi.org/10.1016/j.cpc.2019.107042.

[62] Aldo H. Romero et al. "ABINIT: Overview, and focus on selected capabilities". In: *J. Chem. Phys.* 152 (2020), p. 124102.

[63] François Jollet, Marc Torrent, and Natalie Holzwarth. "Generation of Projector Augmented-Wave atomic data: A 71 element validated table in the XML format". In: *Computer Physics Communications* 185.4 (2014), pp. 1246–1254. ISSN: 0010-4655. DOI: https://doi.org/10.1016/j.cpc.2013.12.023. URL: https://www.sciencedirect.com/science/article/pii/S0010465513004359.

[64] Mitsuaki Kawamura. "FermiSurfer: Fermi-surface viewer providing multiple representation schemes". In: *Computer Physics Communications* 239 (2019), pp. 197–203. ISSN: 0010-4655. DOI: https://doi.org/10.1016/j.cpc.2019.01.017. URL: https://www.sciencedirect.com/science/article/pii/S0010465519300347.

[65] Mikel Iraola et al. "IrRep: Symmetry eigenvalues and irreducible representations of ab initio band structures". In: *Computer Physics Communications* 272 (2022), p. 108226. ISSN: 0010-4655. DOI: https://doi.org/10.1016/j.cpc.2021.108226. URL: https://www.sciencedirect.com/science/article/pii/S0010465521003386.

[66] Ethan T. Ritz, Rafael M. Fernandes, and Turan Birol. "Impact of Sb degrees of freedom on the charge density wave phase diagram of the kagome metal CsV_3Sb_5". In: (2022). arXiv: 2212.13319 [cond-mat.mtrl-sci].

[67] Haitao Yang et al. "Titanium doped kagome superconductor $CsV_3xTi_xSb_5$ and two distinct phases". In: *Science Bulletin* 67.21 (2022), pp. 2176–2185. ISSN: 2095-9273. DOI: https://doi.org/10.1016/j.scib.2022.10.015. URL: https://www.sciencedirect.com/science/article/pii/S2095927322004753.

[68] Shangfei Wu et al. "Charge density wave order in the kagome metal AV_3Sb_5 ($A = Cs, Rb, K$)". In: *Phys. Rev. B* 105 (15 2022), p. 155106. DOI: 10.1103/PhysRevB.105.155106. URL: https://link.aps.org/doi/10.1103/PhysRevB.105.155106.

[69] Farnaz Kaboudvand et al. "Fermi surface nesting and the Lindhard response function in the kagome superconductor CsV3Sb5". In: *Appl. Phys. Lett.* 120.11 (Mar. 2022). ISSN: 0003-6951. DOI: 10.1063/5.0081081.

[70] Ethan Ritz et al. *Superconductivity from Orbital-Selective Electron-Phonon Coupling in* AV_3Sb_5. 2023. arXiv: 2304.14822 [cond-mat.supr-con].

[71] Xavier Gonze. "First-principles responses of solids to atomic displacements and homogeneous electric fields: Implementation of a conjugate-gradient algorithm". In: *Phys. Rev. B* 55 (16 1997), pp. 10337–10354. DOI: 10.1103/PhysRevB.55.10337. URL: https://link.aps.org/doi/10.1103/PhysRevB.55.10337.

Appendix A

Linear response theory and DFPT

Linear response

At the end of the day, we will be doing numerical calculations on our computers, so we will look at finite differences and not really derivatives as in eqs. 4.59-4.60. For the purpose of this section, then, we introduce the finite difference operator $\Delta^{\mathbf{R}}$, which acts on any function that depends parametrically on $\mathbf{R}$ in the following way

$$\Delta^{\mathbf{R}} F_{\mathbf{R}} = \sum_I \frac{\partial F_{\mathbf{R}}}{\partial \mathbf{R}_I} \Delta \mathbf{R}_I \,. \tag{A.1}$$

If we slightly distort the geometry of the nuclei, both the nuclear potential V_n and the ground state density n will change (because of Hohenberg-Kohn's theorem), but this means that also the Hartree potential V_H and the exchange-correlation potential V_{xc} will change. In the context of perturbation theory, we can imagine this as a perturbation ΔV to the Kohn-Sham Hamiltonian

$$H = -\frac{\nabla^2}{2} + V_n(\mathbf{r}, \mathbf{R}) + \overbrace{\int d\mathbf{r}' \frac{n_{\mathbf{R}}(\mathbf{r}')}{|\mathbf{r} - \mathbf{r}'|}}^{V_H(\mathbf{r})} + \overbrace{\frac{\delta E_{xc}}{\delta n_{\mathbf{R}}(\mathbf{r})}}^{V_{xc}(\mathbf{r})} , \tag{A.2}$$

$$\Delta V(\mathbf{r}) = \Delta^{\mathbf{R}} V_n(\mathbf{r}, \mathbf{R}) + \int d\mathbf{r}' \frac{\Delta^{\mathbf{R}} n_{\mathbf{R}}(\mathbf{r}')}{|\mathbf{r} - \mathbf{r}'|} + \left. \frac{dV_{xc}(n)}{dn} \right|_{n=n(\mathbf{r})} \Delta^{\mathbf{R}} n_{\mathbf{R}}(\mathbf{r}) \,, \tag{A.3}$$

where we used the chain rule $\Delta^{\mathbf{R}} F = \frac{dF}{dn} \Delta^{\mathbf{R}} n_{\mathbf{R}}$. From now on $\Delta n = \Delta^{\mathbf{R}} n_{\mathbf{R}}$, so we will get rid of the subscript/superscript $\mathbf{R}$ unless there could be ambiguities. Using the Kohn-Sham wavefunctions ϕ_i, the finite difference in density can be written as

$$\begin{aligned}
\Delta n(\mathbf{r}) &= \sum_i \frac{\partial n_{\mathbf{R}}(\mathbf{r})}{\partial \mathbf{R}_I} \Delta \mathbf{R}_I \\
&= \sum_{I,i} \left[\frac{\partial \phi_i^*(\mathbf{r})}{\partial \mathbf{R}_I} \phi_i(\mathbf{r}) + \phi_i^*(\mathbf{r}) \frac{\partial \phi_i(\mathbf{r})}{\partial \mathbf{R}_I} \right] \Delta \mathbf{R}_I \\
&= \sum_i \Big[\phi_i(\mathbf{r}) \Delta \phi_i^*(\mathbf{r}) + \phi_i^*(\mathbf{r}) \Delta \phi_i(\mathbf{r}) \Big] \\
&= 2\mathrm{Re} \sum_i \phi_i^*(\mathbf{r}) \Delta \phi_i(\mathbf{r}) \,,
\end{aligned} \tag{A.4}$$

where, as for the density, we call $\Delta \phi_i(\mathbf{r}) = \Delta^{\mathbf{R}} \phi_i(\mathbf{r})$. In the last line we assumed that, since both V_{tot} and ΔV are real, the wavefunctions ϕ_i and ϕ_i^* are degenerate, so that $(\Delta \phi_i)^* = \Delta \phi_i^*$.

In perturbation theory we always think that a perturbation to the Hamiltonian causes a perturbation both in the eigenvalue and in the state

$$\Big(H + \Delta V\Big)\Big(|\phi_i\rangle + |\Delta\phi_i\rangle\Big) = \Big(\varepsilon_i + \Delta\varepsilon_i\Big)\Big(|\phi_i\rangle + |\Delta\phi_i\rangle\Big)\,. \tag{A.5}$$

At first order we can ignore the terms $\Delta V|\Delta\phi_i\rangle$ and $\Delta\varepsilon_i|\Delta\phi_i\rangle$, such that we can rearrange the other terms to obtain

$$\Big(H - \varepsilon_i\Big)|\Delta\phi_i\rangle = -\Big(\Delta V - \Delta\varepsilon_i\Big)|\phi_i\rangle\,. \tag{A.6}$$

Since we usually assume that the perturbation to the state is orthogonal to the state itself (i.e., $\langle\phi_i|\Delta\phi_i\rangle = 0$), by projecting eq. A.6 on $\langle\phi_i|$ we get

$$\Delta\varepsilon_i = \langle\phi_i|\Delta V|\phi_i\rangle\,, \tag{A.7}$$

while projecting on any other $\langle\phi_j|$ with $j \neq i$ we get

$$|\Delta\phi_i\rangle = \sum_{j\neq i} \frac{\langle\phi_j|\Delta V|\phi_i\rangle}{\varepsilon_i - \varepsilon_j}|\phi_j\rangle\,, \tag{A.8}$$

which are the standard textbook results of first-order perturbation theory. We subtly just introduced a new set of self-consistent equations: $\Delta V(\mathbf{r})$ is a linear functional of $\Delta n(\mathbf{r})$, which in turn depends linearly on the set of $\Delta\phi_i(\mathbf{r})$'s, and they depend on $\Delta V(\mathbf{r})$, and so on... Let us rewrite this set of self-consistent equations once more, all together

$$\Delta V(\mathbf{r}) = \Delta^{\mathbf{R}} V_n(\mathbf{r},\mathbf{R}) + \int d\mathbf{r}' \frac{\Delta n(\mathbf{r}')}{|\mathbf{r}-\mathbf{r}'|} + \left.\frac{dV_{xc}(n)}{dn}\right|_{n=n(\mathbf{r})} \Delta n(\mathbf{r})\,, \tag{A.9}$$

$$\Delta n(\mathbf{r}) = 2\mathrm{Re}\sum_i \sum_{j\neq i} \phi_i^*(\mathbf{r})\phi_j(\mathbf{r}) \frac{\langle\phi_j|\Delta V|\phi_i\rangle}{\varepsilon_i - \varepsilon_j}\,, \tag{A.10}$$

where in the second one we used eq. A.8 (projected in the real space basis), to rewrite the density linear response to the perturbation.

Now, in a non-magnetic system, each of the lowest $N/2$ states is occupied by two electrons with opposite spins, so that in the density we can just sum i from 1 to $N/2$

$$\Delta n(\mathbf{r}) = 4\mathrm{Re}\sum_{i=1}^{N/2} \sum_{j\neq i} \phi_i^*(\mathbf{r})\phi_j(\mathbf{r}) \frac{\langle\phi_j|\Delta V|\phi_i\rangle}{\varepsilon_i - \varepsilon_j}\,, \tag{A.11}$$

and from this we can see that the density response to the perturbation only comes from matrix elements that mix one occupied and one non-occupied state: the terms that only mix occupied states can be regrouped as (remember we assumed ΔV to be real)

$$\frac{\Delta V_{ij}}{\varepsilon_i - \varepsilon_j}\Big(\phi_i^*\phi_j - \phi_j^*\phi_i\Big)\,, \tag{A.12}$$

but this is a purely imaginary term, so it gets canceled when we take the real part of Δn.

Unfortunately, it turns out that evaluating Δn this way is not computationally efficient, since it requires extensive summation over the unoccupied states, so it is way faster to just solve the coupled linear system in eq. A.6 with iterative methods[1]. The only problem is that the operator $(H - \varepsilon_i)$ on the LHS of A.6 is non-invertible since it clearly has one null eigenvalue. Since we saw that the response of the system to a perturbation only depends on the matrix elements that mix occupied (valence) states with unoccupied

[1] It is my understanding that Abinit uses the so called *conjugate-gradient* method, see Reference [71].

(conduction) states, we can project the RHS on the unoccupied states manifold with a projection operator P_c, and add a multiple of a projector operator P_v onto the occupied states manifold in the LHS as to make it invertible:

$$\Big(H + \alpha P_v - \varepsilon_i\Big)|\Delta\phi_i\rangle = -P_c \Delta V |\phi_i\rangle \,, \tag{A.13}$$

and so this is the linear system that we have to solve[2].

Monochromatic perturbations

Let us introduce in eq. A.13 an index for the wavevector $\mathbf{k}$ in the Brillouin Zone and an index v indicating which valence band we are talking about. Projecting both sides of the last equation on the manifold of states at some other wavevector $\mathbf{k}+\mathbf{q}$, we obtain

$$P^{\mathbf{k}+\mathbf{q}}\Big(H + \alpha P_v - \varepsilon_{v\mathbf{k}}\Big)|\Delta\phi_{v\mathbf{k}}\rangle = -P^{\mathbf{k}+\mathbf{q}} P_c \Delta V |\phi_{v\mathbf{k}}\rangle \,. \tag{A.14}$$

Because of translational invariance, $P^{\mathbf{k}+\mathbf{q}}$ commutes with H and with the other projectors, so that we can write

$$\Big(H + \alpha P_v^{\mathbf{k}+\mathbf{q}} - \varepsilon_{v\mathbf{k}}\Big)|\Delta\phi_{v\mathbf{k}+\mathbf{q}}\rangle = -P_c^{\mathbf{k}+\mathbf{q}} \Delta V |\phi_{v\mathbf{k}}\rangle \,, \tag{A.15}$$

where $P_{v,c}^{\mathbf{k}+\mathbf{q}} = P^{\mathbf{k}+\mathbf{q}} P_{v,c}$ is the projector onto the occupied/empty states at momentum $\mathbf{k}+\mathbf{q}$ and $P^{\mathbf{k}+\mathbf{q}}|\Delta\phi_{v\mathbf{k}}\rangle = |\Delta\phi_{v\mathbf{k}+\mathbf{q}}\rangle$[3].

Now we can decompose the perturbation in Fourier harmonics

$$\Delta V(\mathbf{r}) = \sum_{\mathbf{q}} \Delta V_{\mathbf{q}}(\mathbf{r}) e^{i\mathbf{q}\cdot\mathbf{r}} \tag{A.16}$$

where $\Delta V^{\mathbf{q}}(\mathbf{r})$ are lattice-periodic functions. Following what we already did in Section 4, we can rewrite A.15 for just the periodic parts $u_{v\mathbf{k}}$ and $\Delta u_{v\mathbf{k}}$ of the wavefunctions

$$\Big(H_{\mathbf{k}+\mathbf{q}} + \alpha \sum_{v'} |u_{v'\mathbf{k}+\mathbf{q}}\rangle\langle u_{v'\mathbf{k}+\mathbf{q}}| - \varepsilon_{v\mathbf{k}}\Big)|\Delta u_{v\mathbf{k}+\mathbf{q}}\rangle = -\Big(1 - \sum_{v'} |u_{v'\mathbf{k}+\mathbf{q}}\rangle\langle u_{v'\mathbf{k}+\mathbf{q}}|\Big)\Delta V_{\mathbf{q}} |u_{v\mathbf{k}}\rangle \,, \tag{A.17}$$

where $H_{\mathbf{k}+\mathbf{q}} = e^{-i(\mathbf{k}+\mathbf{q})\cdot\mathbf{r}} H e^{i(\mathbf{k}+\mathbf{q})\cdot\mathbf{r}}$. The Fourier components of the density response and of the perturbation are

$$\Delta n_{\mathbf{q}}(\mathbf{r}) = 4 \sum_{v\mathbf{k}} u^*_{v\mathbf{k}}(\mathbf{r}) \Delta u_{v\mathbf{k}+\mathbf{q}}(\mathbf{r}) \,, \tag{A.18}$$

$$\Delta V_{\mathbf{q}}(\mathbf{r}) = \Delta V_{n,\mathbf{q}}(\mathbf{r}) + \int d\mathbf{r}' \frac{\Delta n_{\mathbf{q}}(\mathbf{r}')}{|\mathbf{r}-\mathbf{r}'|} e^{i\mathbf{q}\cdot(\mathbf{r}-\mathbf{r}')} + \left.\frac{dV_{xc}(n)}{dn}\right|_{n=n(\mathbf{r})} \Delta n_{\mathbf{q}}(\mathbf{r}) \,. \tag{A.19}$$

In conclusion, quoting from Ref. [59], eqs. A.17-A.18-A.19 , sometimes called Sternheimer equations, "form a set of self-consistent relations for the charge-density and wave-function linear response to a perturbation of a wave vector $\mathbf{q}$, which can be solved in terms of lattice periodic functions only, and which is decoupled from all other sets of similar equations holding for other Fourier components of the same perturbation. Thus perturbations of different periodicity can be treated independently of each other with a numerical workload that is, for each perturbation, of the same order as that needed for the unperturbed system."

[2] This above discussion only applies to system with a finite gap, i.e., insulators and not metals.
[3] Of course for any projector operator P it holds that $P^2 = P$.

Appendix B

Other simulated shandites

We report the band structures, relaxed lattice parameters and lowest phonon frequency $\omega_{1\mathbf{F}}$ at the **F** point. These quantities were calculated with DFT as implemented in Abinit 9.6.2, using the PBE GGA exhange-correlation functional, a 16x16x16 Γ centered **k**-point grid and a PAW basis with energy cutoff of 500eV. The electronic states were occupied using a Gaussian smearing scheme with smearing temperature of 10 meV. The structure was relaxed until all the forces were small than 1 meV/Å in modulus.

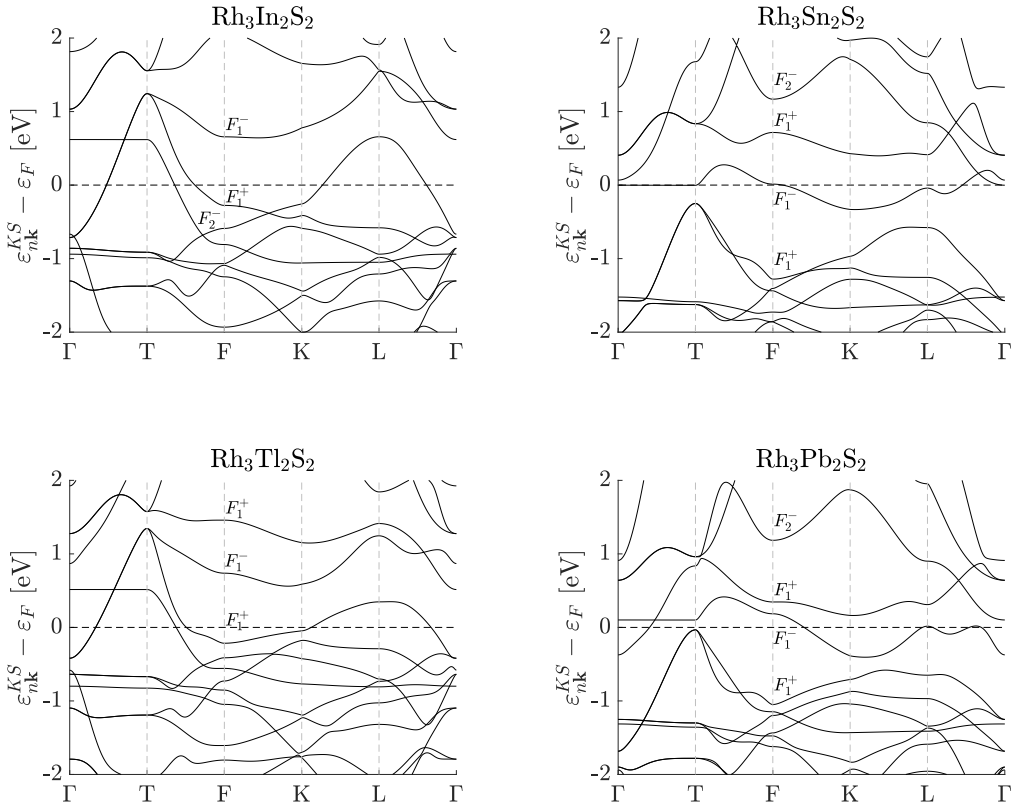

Figure B.1: Band structures of Rh kagome compounds and symmetry of the wavefunctions at the F point, labeled by the little group irrep.

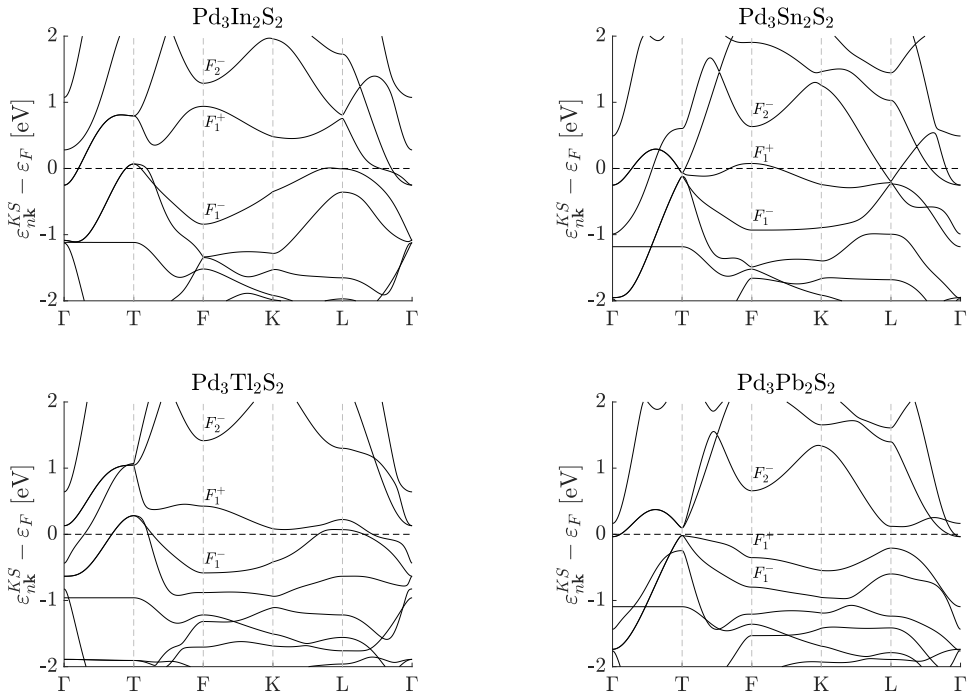

Figure B.2: Band structures of Pd kagome compounds and symmetry of the wavefunctions at the F point, labeled by the little group irrep.

Formula	a [Å]	α	z	$\omega_{1\mathbf{F}}$ [meV]
$Rh_3In_2S_2$	5.5491	60.46°	0.7145	6.81
$Rh_3Sn_2S_2$	5.4914	61.68°	0.7113	8.17
$Rh_3Tl_2S_2$	5.7711	59.67°	0.7221	3.68
$Rh_3Pb_2S_2$	5.6774	60.40°	0.7171	5.36
$Pd_3In_2S_2$	5.6203	61.31°	0.7129	5.11
$Pd_3Sn_2S_2$	5.5970	63.10°	0.7122	6.34
$Pd_3Tl_2S_2$	5.8463	60.27°	0.7213	4.27
$Pd_3Pb_2S_2$	5.7576	62.47°	0.7192	7.49

Table B.1: Lattice parameters calculated with DFT after relaxation, where α is the length of the primitive translation vectors, α is the angle between them and z is the parameter needed to describe the position of the sulphur atom. The table also reports on the right most column the value of the lowest phonon frequency at the **F** point, calculated with DFPT.